

WL-TR-94-1095

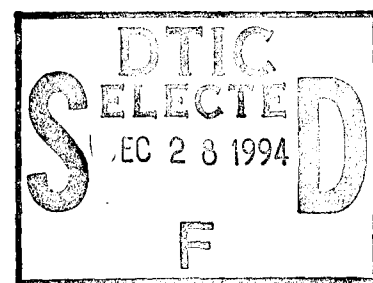
**INFRARED MULTISPECTRAL SENSOR
PROGRAM, PHASE 2: FIELD
MEASUREMENTS, ANALYSIS AND
MODELING**



**Volume 1: Fourier Transform Spectrometer
Sensor Characterization**

J.N. Cederquist, M.T. Eismann, C.R. Schwartz,
J.H. Seldin and A.D. Stocker (SCC)

Environmental Research Institute of Michigan
PO Box 134001
Ann Arbor, MI 48113-4001



MAY 1994

Final Report for 01/01/93 - 12/01/93

Approved for public release; distribution is unlimited.

Avionics Directorate
Wright Laboratory
Air Force Materiel Command
Wright-Patterson AFB, OH 45433-7409

19941223 001

DTIC QUALITY INSPECTED 1

NOTICE

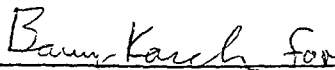
When Government drawings, specifications, or other data are used for any purpose other than in connection with a definitely Government-related procurement, the United States Government incurs no responsibility or any obligation whatsoever. The fact that the government may have formulated or in any way supplied the said drawings, specifications, or other data, is not to be regarded by implication, or otherwise in any manner construed, as licensing the holder, or any other person or corporation; or as conveying any rights or permission to manufacture, use, or sell any patented invention that may in any way be related thereto.

This report is releasable to the National Technical Information Service (NTIS). At NTIS, it will be available to the general public, including foreign nations.

This technical report has been reviewed and is approved for publication.



RAY O. JOHNSON, PhD
Capt USAF
Targeting Systems Section



HENRY S. LAPP, Chief
Targeting Systems Section
Electro-Optical Branch



PAUL F. McMANAMON, Chief
Electro-Optical Branch
Mission Avionics Division

If your address has changed, if you wish to be removed from our mailing list, or if the addressee is no longer employed by your organization please notify WL/AARI, WPAFB, OH 45433-7408 to help us maintain a current mailing list.

Copies of this report should not be returned unless return is required by security considerations, contractual obligations, or notice on a specific document.

REPORT DOCUMENTATION PAGE

Form Approved
OMB No. 0704-0188

Public reporting burden for the collection of information is estimated to average 1 hour per response, including the time for reviewing instructions, searching existing data sources, gathering and maintaining the data needed, and completing and reviewing the collection of information. Send comments regarding this burden estimate or any other aspect of this collection of information, including suggestions for reducing this burden, to Washington Headquarters Services, Directorate for Information Operations and Reports, 1215 Jefferson Davis Highway, Suite 1204, Arlington, VA 22202-4302, and to the Office of Management and Budget, Paperwork Reduction Project (0704-0188), Washington, DC 20503.

1. AGENCY USE ONLY (Leave Blank)

2. REPORT DATE

May 1994

3. REPORT TYPE AND DATES COVERED

Final 01/01/93 - 12/01/93

4. TITLE AND SUBTITLE

Infrared Multispectral Sensor Program, Phase 2: Field Measurements, Analysis and Modeling; Vol 1: Fourier Transform Spectrometer Sensor Characterization

5. FUNDING NUMBERS

C F 33615-90-C-1441

PE 63226

PR 2004

TA 05

WU 81

6. AUTHOR(S)

J.N. Cederquist, M.T. Eismann, C.R. Schwartz,
J.H. Seldin and A.D. Stocker

7. PERFORMING ORGANIZATION NAME(S) AND ADDRESS(ES)

Environmental Research Institute of Michigan
P.O. Box 134001
Ann Arbor, MI 48113-40018. PERFORMING ORGANIZATION
REPORT NUMBERERIM 232300-54-F (Vol 1);
Tasks: 93-4-1, 93-4-3,
93-4-4

9. SPONSORING/MONITORING AGENCY NAME(S) AND ADDRESS(ES)

Avionics Directorate
Wright Laboratory
Air Force Materiel Command
Wright Patterson AFB, OH 45433-740910. SPONSORING/MONITORING AGENCY
REPORT NUMBER

WL-TR-94-1095

11. SUPPLEMENTARY NOTES

Sponsored by ARPA

12a. DISTRIBUTION/AVAILABILITY STATEMENT

Approved for public release; distribution is unlimited.

12b. DISTRIBUTION CODE

13. ABSTRACT (Maximum 200 words)

A data collection sensor based on a Bomem Fourier transform spectrometer was used to measure infrared multispectral target/background signatures. This report describes the data collection sensor, including data processing software for quick look data analysis, gives the sensor characteristics test procedures and their results, and analyzes the effect of the sensor characteristics on the quality of the measured signatures. The sensor gives a very high level of performance including noise equivalent spectral radiances of $1 \text{ nW/cm}^2 \text{ sr cm}^{-1}$ in the MWIR (3 to 5 μm) region and $6 \text{ nW/cm}^2 \text{ sr cm}^{-1}$ in the LWIR (8 to 12 μm region), a relative calibration accuracy to less than 0.25% above 4 μm , and spectral band-to-band correlation preservation greater than 0.9999 in the LWIR, and greater than 0.9995 between MWIR and LWIR and within the 4 to 5 μm region of the MWIR.

14. SUBJECT TERMS

Infrared, Multispectral, Target Detection, IR Phenomenology,
IR modeling, Fourier Transform Spectrometer

15. NUMBER OF PAGES

164

16. PRICE CODE

17. SECURITY CLASSIFICATION
OF REPORT

Unclassified

18. SECURITY CLASSIFICATION
OF THIS PAGE

Unclassified

19. SECURITY CLASSIFICATION
OF ABSTRACT

Unclassified

20. LIMITATION OF ABSTRACT

UL

PREFACE

The work reported here was performed by the Environmental Research Institute of Michigan (ERIM) with assistance from Space Computer Corporation (SCC). The work was sponsored by Dr. Larry B. Stotts of ARPA/ASTO and managed through the Avionics Directorate of Wright Laboratory, Contract F33615-90-C-1441. At WL/AARI, the technical monitor was Major Robert Esquire. The ERIM program manager was Barry W. Lyons.

This final technical report covers work performed from 26 January 1993 to 31 December 1993. The task leader was John Cederquist. Major contributors to the effort were Michael Eismann, Craig Schwartz, John Seldin and Alan Stocker (SCC).

Distribution For	
<input checked="" type="checkbox"/> CHAS1 <input type="checkbox"/> TAG <input type="checkbox"/> Standard <input type="checkbox"/> ...	<input checked="" type="checkbox"/> <input type="checkbox"/> <input type="checkbox"/>
Priority Usage	
Author/Editor	
A-I	

CONTENTS

PREFACE	iii
FIGURES	ix
TABLES	xiii
1.0 OVERVIEW	1-1
1.1 INTRODUCTION	1-1
1.2 SUMMARY OF PHASE 2 ACCOMPLISHMENTS	1-1
1.3 GUIDE TO THE REPORT	1-2
1.4 REFERENCES	1-2
2.0 FTS INSTRUMENT HARDWARE SPECIFICATION	2-1
2.1 INFRARED SPECTROMETER	2-1
2.1.1 Design Requirements	2-1
2.1.1.1 Spectral Characteristics	2-1
2.1.1.2 Spatial Characteristics	2-1
2.1.1.3 Radiometric Sensitivity	2-3
2.1.1.4 Measurement Fidelity	2-3
2.1.1.5 Operation	2-3
2.1.2 Configuration	2-3
2.1.2.1 Bomem MB-100	2-3
2.1.2.2 Imaging Optics	2-5
2.1.2.3 Data Interface	2-5
2.1.3 Specifications	2-7
2.2 RADIOMETRIC CALIBRATION EQUIPMENT	2-7
2.2.1 Design Requirements	2-7
2.2.2 Configuration	2-8
2.2.3 Specifications	2-10
2.3 AZIMUTH/ELEVATION MOUNT	2-10
2.3.1 Design Requirements	2-10
2.3.2 Configuration	2-11
2.3.3 Specifications	2-11
2.4 CONTROL AND DATA ACQUISITION SYSTEM	2-13
2.4.1 Design Requirements	2-13
2.4.2 Configuration	2-14
2.4.3 Specifications	2-14
2.5 BORESIGHT VIDEO EQUIPMENT	2-16
2.5.1 Design Requirements	2-16
2.5.2 Configuration	2-16
2.5.3 Specifications	2-18

CONTENTS

2.6	REFERENCES	2-19
3.0	QUICK LOOK SOFTWARE	3-1
3.1	OVERVIEW	3-1
3.2	INSTALLATION OF THE DOS EXTENDER	3-1
3.3	REBUILDING QUICK-LOOK WITH BORLAND C PROJECT FILES	3-2
3.4	RUNNING QUICK-LOOK	3-2
3.4.1	Default File, QLOOK.DEF	3-2
3.4.2	Required Experiment Files	3-3
3.4.3	Quick-Look Functions	3-4
3.4.4	Plotting Capabilities, Hidden Functionality, Saving Plots	3-8
4.0	FTS SENSOR CHARACTERIZATION TESTS AND RESULTS	4-1
4.1	SENSOR NOISE	4-1
4.2	ABSOLUTE CALIBRATION ACCURACY	4-10
4.3	RELATIVE CALIBRATION ACCURACY	4-13
4.4	TEMPORAL RADIOMETRIC STABILITY	4-28
4.5	RESPONSE LINEARITY	4-30
4.6	POLARIZATION SENSITIVITY	4-44
4.7	SPATIAL REGISTRATION	4-47
4.8	CORRELATION PRESERVATION	4-48
4.9	POINTING REPEATABILITY	4-60
4.10	POINTING STABILITY	4-61
4.11	REFERENCES	4-63
5.0	SENSOR CHARACTERISTICS ANALYSIS	5-1
5.1	MEASUREMENT STATISTICS	5-1
5.2	NOISE	5-2
5.2.1	Effects on Measurements	5-2
5.2.2	Anticipated Noise Effects	5-2
5.3	ABSOLUTE CALIBRATION ACCURACY	5-7
5.3.1	Effects on Measurements	5-7
5.3.2	Anticipated Accuracy Levels	5-8
5.4	RELATIVE CALIBRATION ACCURACY	5-9
5.4.1	Effects on Measurements	5-9
5.4.2	Anticipated Accuracy Levels	5-10
5.5	SENSOR STABILITY	5-14
5.5.1	Effects on Measurements	5-14
5.5.2	Anticipated Accuracy Levels	5-15

CONTENTS

5.6	RESPONSE LINEARITY	5-18
5.6.1	Effects on Measurements	5-18
5.6.2	Anticipated Level	5-19
5.7	POLARIZATION SENSITIVITY	5-19
5.7.1	Effects on Measurements	5-19
5.7.2	Anticipated Accuracy Levels	5-21
5.8	SPATIAL FOOTPRINT	5-28
5.8.1	Effects on Measurements	5-28
5.8.2	Anticipated Level	5-28
5.9	SPATIAL REGISTRATION	5-28
5.10	POINTING ACCURACY	5-29
5.10.1	Effects on Measurements	5-29
5.10.2	Anticipated Level	5-29
5.11	POINTING REPEATABILITY	5-29
5.11.1	Effects on Measurements	5-29
5.11.2	Anticipated Level	5-29
5.12	POINTING STABILITY	5-30
5.12.1	Effects on Measurements	5-30
5.12.2	Anticipated Level	5-30
6.0	PRELIMINARY DATA ANALYSIS RESULTS	6-1
	Appendix A: Confidence Limits for Quick Look Parameter Estimates	A-1
A.1	Introduction and Summary	A-1
A.2	Mean Radiance	A-1
A.3	Mean Radiance Contrast	A-2
A.4	Radiance Variance	A-4
A.5	Spectral Correlation Coefficient	A-6
A.6	References	A-7
	Appendix B. Two Point Calibration Error Analysis	B-1
B.1	Two Point Radiometric Calibration	B-1
B.2	Calibration Error Sources	B-2
B.2.1	Absolute Temperature Inaccuracy (Temporally fixed error)	B-4
B.2.2	Emissivity Uncertainty (Temporally fixed error)	B-4
B.2.3	Temperature Instability (Temporally varying error)	B-5
B.2.4	Random Reflected Radiance Components	B-5
B.3	Calibration Error Case Analyses	B-5
B.3.1	Case 1: Measurements Within a Single Calibration Cycle	B-5
B.3.2	Case 2: Measurements Made Within Different Calibration Cycles	B-6

CONTENTS

B.4 Calibration Error Examples	B-7
B.4.1 Case 1: Measurements Within a Single Calibration Cycle	B-7
B.4.2 Case 2: Measurements Made Within Different Calibration Cycles	B-8
B.5 Conclusions	B-8

FIGURES

2-1.	Field Spectrometer Systems Diagram	2-2
2-2.	Schematic Drawing of MB-100 Interferometer on Wishbone Scan Arm . .	2-4
2-3.	Side View of FTS With Collimator and NFOV Telescope	2-6
2-4.	Perspective Drawing of Blackbody Calibration Source	2-9
2-5.	Azimuth/Elevation Mount Assembly Including Drive Stages and Payload (FTS)	2-12
2-6.	Control and Data Acquisition System Block Diagram	2-15
2-7.	Boresight Video Camera Interface Schematic	2-17
4-1.	Noise Dependence on Spectral Bandwidth (5-18-93)	4-4
4-2.	Noise Dependence on Temperature (5-18-93)	4-5
4-3.	Noise Correlation With 4.7 microns (5-18-93)	4-7
4-4.	Noise Correlation With 10 microns (5-18-93)	4-8
4-5.	Noise at 8 cm^{-1} (8-31-93)	4-9
4-6.	Blackbody Apparent Emissivity (8-31-93)	4-12
4-7.	Blackbody Radiometric Accuracy (8-31-93)	4-14
4-8.	Absolute Calibration Accuracy	4-15
4-9.	Blackbody Stability on 7-7-93 (#1)	4-17
4-10.	Blackbody Stability on 7-7-93 (#2)	4-18
4-11.	Blackbody Stability on 7-16-93	4-19
4-12.	Blackbody Stability on 7-17-93	4-20
4-13.	Blackbody Stability on 7-19-93	4-21

FIGURES

4-14. Blackbody Stability on 7-20-93	4-22
4-15. Blackbody Stability on 7-21-93	4-23
4-16. Blackbody Stability on 7-22-93	4-24
4-17. Average Blackbody Stability	4-26
4-18. Relative Calibration Accuracy	4-27
4-19. FTS Stability on 7-7-93 (#1)	4-31
4-20. FTS Stability on 7-7-93 (#2)	4-32
4-21. FTS Stability on 7-16-93	4-33
4-22. FTS Stability on 7-17-93	4-34
4-23. FTS Stability on 7-19-93	4-35
4-24. FTS Stability on 7-20-93	4-36
4-25. FTS Stability on 7-21-93	4-37
4-26. FTS Stability on 7-22-93	4-38
4-27. Average FTS Stability	4-39
4-28. Scatter Plot of Linearity Measurements Compared to Blackbody Predictions	4-41
4-29. Linearity Test via Correlation With 4.7 microns	4-42
4-30. Linearity Test via Correlation With 10 microns	4-43
4-31. Polarization Test on 8-31-93	4-46
4-32. Spatial Registration Test via Line Spread Function	4-49
4-33. Decorrelation on 7-7-93 (#1)	4-51

FIGURES

4-34.	Decorrelation on 7-7-93 (#2)	4-52
4-35.	Decorrelation on 7-16-93	4-53
4-36.	Decorrelation on 7-17-93	4-54
4-37.	Decorrelation on 7-19-93	4-55
4-38.	Decorrelation on 7-20-93	4-56
4-39.	Decorrelation on 7-21-93	4-57
4-40.	Decorrelation on 7-22-93	4-58
4-41.	Average Decorrelation	4-59
5-1.	Minimum Detectable Contrast (μ flicks) vs. Number of Coadded Scans . .	5-4
5-2.	Maximum Equivalent Clutter Suppression (dB) vs. Number of Coadded Scans	5-5
5-3.	Maximum Equivalent Clutter Suppression (300K Target, $N_s=15$) vs. Background Clutter Level (σ_T)	5-6
5-4.	Maximum Equivalent Clutter Suppression (300K Target, $N_s=25$) vs. Background Clutter Level (σ_T)	5-7
5-5.	Maximum Equivalent Clutter Suppression vs. Source Temperature Instability σ_{CAL} (300K Target, 45C and 20C Calibration Points, $\sigma_T = 1.0K$)	5-12
5-6.	Decorrelation Factor vs. Source Temperature Instability σ_{CAL} (300K Target, 45C and 20C Calibration Points, $\sigma_T=1.0K$)	5-12
5-7.	Correlation Bias vs. Source Temperature Instability σ_{CAL} (300K Target, 45C and 20C Calibration Points, $\sigma_T=1.0K$)	5-13
5-8.	Maximum Equivalent Clutter Suppression vs. Clutter Level σ_T (300K Target, 45C and 20C Calibration Points, $\sigma_{CAL}=0.03K$)	5-14

FIGURES

5-9.	Maximum Equivalent Clutter Suppression vs. $\rho_{bb}(\lambda_1, \lambda_2)$ for $\lambda_1=4.7\mu\text{m}$ and $\lambda_2=10.0\mu\text{m}$ (Assuming $\sigma_{\text{INS}}=0.02\text{K}$, $\sigma_{\text{T}}=1\text{K}$, and a 300K Background)	5-17
5-10.	Maximum Equivalent Clutter Suppression vs. σ_{INS} for Various Band Combinations ((3.8 μm ,4.7 μm), (4.7 μm ,10.0 μm), and (8.0 μm , 10.0 μm)) (Assuming $\sigma_{\text{T}}=1\text{K}$, $\rho_{bb}(\lambda_1, \lambda_2)=0.0$, and a 300K Background)	5-17
5-11.	Maximum Equivalent Clutter Suppression vs. Background Clutter Level (σ_{T}) for Various Band Combinations ((3.8 μm ,4.7 μm), (4.7 μm ,10.0 μm), and (8.0 μm ,10.0 μm)) (Assuming $\sigma_{\text{INS}}=0.02\text{K}$, $\rho_{bb}(\lambda_1, \lambda_2)=0.0$, and a 300K Background)	5-18
5-12.	Measured BSDF for CARC 383 Green Paint ($\theta_i=60$ degrees)	5-22
5-13.	Directional Hemispherical Reflectance of CARC 383 Green Camouflage Paint	5-23
5-14.	Target Degree of Polarization (Includes Both Emission and Reflection)	5-24
5-15.	Target and Background Radiance Error Due to Sensor Polarization Sensitivity	5-25
5-16.	Mean Contrast Error Due to Sensor Polarization Sensitivity	5-26
5-17.	Maximum Equivalent Clutter Suppression vs. Background Polarization Level α (%) (Polarization Variance $\sigma_{\alpha}=0.167\alpha$, $\sigma_{\text{T}}=1\text{K}$, $\epsilon_{\text{bkg}}=0.98$, $T_{\text{bkg}}=300\text{K}$, $T_{\text{sky}}=250\text{K}$)	5-27
5-18.	Maximum Equivalent Clutter Suppression vs. Background Clutter Level (σ_{T}) ($\alpha=0.3\%$, $\sigma_{\alpha}=0.05\%$, $\epsilon_{\text{bkg}}=0.98$, $T_{\text{bkg}}=300\text{K}$, $T_{\text{sky}}=250\text{K}$)	5-27
6-1.	Treeline Correlation With 10.1 Microns	6-2
6-2.	Mean Contrast: CARC Panel vs. Treeline	6-3
6-3.	CARC Panel and Treeline	6-5
6-4.	Signal-to-Clutter Ratio for CARC Panel vs. Treeline	6-6
6-5.	Low Emissivity Panel and Treeline	6-7

TABLES

4-1:	Sensor Characterization Test Summary	4-2
4-2:	Noise Performance Summary	4-10
4-3:	Correlation Test Results With and Without Temporal Calibration	4-50
4-4:	Pointing Repeatability Measurements Results	4-61
4-5:	Pointing Stability Measurements Results	4-62
5-1:	Sensor Noise for $N_s=15$ Coadded Scans	5-3
5-2:	Correlation vs. Equivalent Clutter Suppression	5-5
5-3:	Anticipated Absolute Calibration Accuracies (Based on the Blackbody Source Manufacturer's Specifications)	5-8
5-4:	Anticipated Relative Calibration Accuracies for Mean Contrast Measurements (Based on the Blackbody Source Manufacturer's Specifications)	5-10
5-5:	Anticipated Instability Mean Contrast Error Levels (Assuming a 300K Target)	5-16
A-1:	Student's t-Distribution	A-3
A-2:	Percentage Points of the Chi-Square Distribution	A-5
B-1:	Case 2 Calibration Errors	B-8

1.0 OVERVIEW

1.1 INTRODUCTION

The goal of the ARPA Multispectral Sensor Program (MSSP) is to develop infrared (IR) multispectral sensors for ARPA Warbreaker focused surveillance and targeting applications. The program is proceeding in phases. Phase 1, which occurred in FY 92, analyzed existing data, developed target and background models, and made promising predictions of target detection performance [1.1]. These results motivated Phase 2 which collected IR multispectral data with a tower-based Fourier transform spectrometer, determined target and background signatures, and compared the measurements to the models developed earlier. Phase 2 is discussed in more detail below. Phase 3 could acquire a tower-based or an airborne data collection instrument, collect IR multispectral images of targets and potential false alarm regions, and develop target detection algorithms. Phase 4 could build an airborne IR multispectral sensor and use it in Warbreaker system demonstrations.

1.2 SUMMARY OF PHASE 2 ACCOMPLISHMENTS

Phase 2 has been funded under the EO CC&D contract F33615-90-C-1441 and the IRIA contract DLA900-88-D-0312. The main accomplishments of the part funded by the EO CC&D contract have been: 1) integration of an IR Fourier transform spectrometer with a pan/tilt mount for automated calibration and data collection, 2) development of quick look data analysis software including confidence bounds on quantities estimated from data, 3) characterization of the spectrometer (noise, stability, calibration accuracy) to verify performance exceeds goals for target/background spectral contrast and correlation measurements, 4) fabrication of calibration panels and test targets (panels, box and cylinder) and use of current and next generation camouflage paints, mats and nets in data collection, 5) collection of contrast, correlation, and model validation data sets on test targets, camouflage nets and trucks in grass, treeline and partially obscured by forest backgrounds from towers at WPAFB and Redstone Arsenal, 6) measurement of target/background spectral contrast finding IR spectral signature differences supporting high IR multispectral processing gain for targets where the single

band signal-to-clutter ratio is low, 7) measurement of background band-to-band spectral correlation to higher levels than any previous sensor finding high correlation supporting high IR multispectral processing gain and 8) tracking IR multispectral signatures from night through thermal crossover into day to enable better understanding of phenomenology and to improve adaptive target detection algorithms.

1.3 GUIDE TO THE REPORT

The Phase 2 work funded under the EO CC&D contract is reported in three volumes. Volume 1 (this volume) describes the IR multispectral sensor and its characteristics. Volume 2 catalogs the data collected at Redstone Arsenal [1.2]. Volume 3 catalogs the data collected at WPAFB [1.3]. In Volume 1, Section 2 gives the Fourier transform spectrometer specification. Section 3 and Appendix A describe the quick look software used for data analysis. Section 4 details the sensor specification tests and their results. Section 5 and Appendix B analyze the effects of the anticipated sensor characteristics on the measured data. Section 6 gives the results of preliminary analysis of the data.

1.4 REFERENCES

- [1.1] J.N. Cederquist, et al., "Infrared Multispectral Sensor Program, Phase 1: Model-Based Performance Predictions," ERIM Report 232300-41-F to ARPA/WL on contract F33615-90-C-1441, October 1993.
- [1.2] J.N. Cederquist, et al., "Infrared Multispectral Sensor Program, Phase 2: Field Measurements, Analysis and Modeling; Volume 2: Redstone Arsenal Measurements Catalog," ERIM Report 232300-54-F(V2) to ARPA/WL on contract F33615-90-C-1441, October 1993.
- [1.3] C.R. Schwartz, "Infrared Multispectral Sensor Program, Phase 2: Field Measurements, Analysis and Modeling; Volume 3: Wright-Patterson Air Force Base Measurements Catalog," ERIM Report 232300-54-F(V3) to ARPA/WL on contract F33516-90-C-1441, May 1994.

2.0 FTS INSTRUMENT HARDWARE SPECIFICATION

This section summarizes the hardware specifications of the MSSP Fourier Transform Spectrometer (FTS) sensor system. This system consists of five primary components:

1. infrared spectrometer,
2. radiometric calibration equipment,
3. azimuth/elevation mount,
4. control and data acquisition equipment, and
5. boresight video equipment.

Figure 2-1 provides a block diagram of the entire system. The design requirements, configuration, and specifications of each of these components is addressed throughout the remainder of this section.

2.1 INFRARED SPECTROMETER

2.1.1 Design Requirements

The requirements of the infrared spectrometer are driven by the primary objective of collecting a suitable spectral database to assess the spectral correlation of backgrounds and the spectral contrast between various targets and the surrounding background.

2.1.1.1 Spectral Characteristics

Based on flat plate model results as well as characteristic spectra found in the SAL database, the spectral resolution of the spectrometer must be on the order of 100-200 nm or better. Ideally, a continuum of bands across the MWIR (3-5 microns) and LWIR (8-12 microns) should be investigated in a simultaneous manner such that changes in environment and instrument pointing do not introduce errors in the measured spectrum.

2.1.1.2 Spatial Characteristics

The spatial resolution of the spectrometer should be on the order of 0.3-1.0m on a target. For tower ranges of 50-100m, the spectrometer IFOV should be on the order of 5 mrad or better. Spatial registration between bands should be at least a tenth of an IFOV, and preferably better.

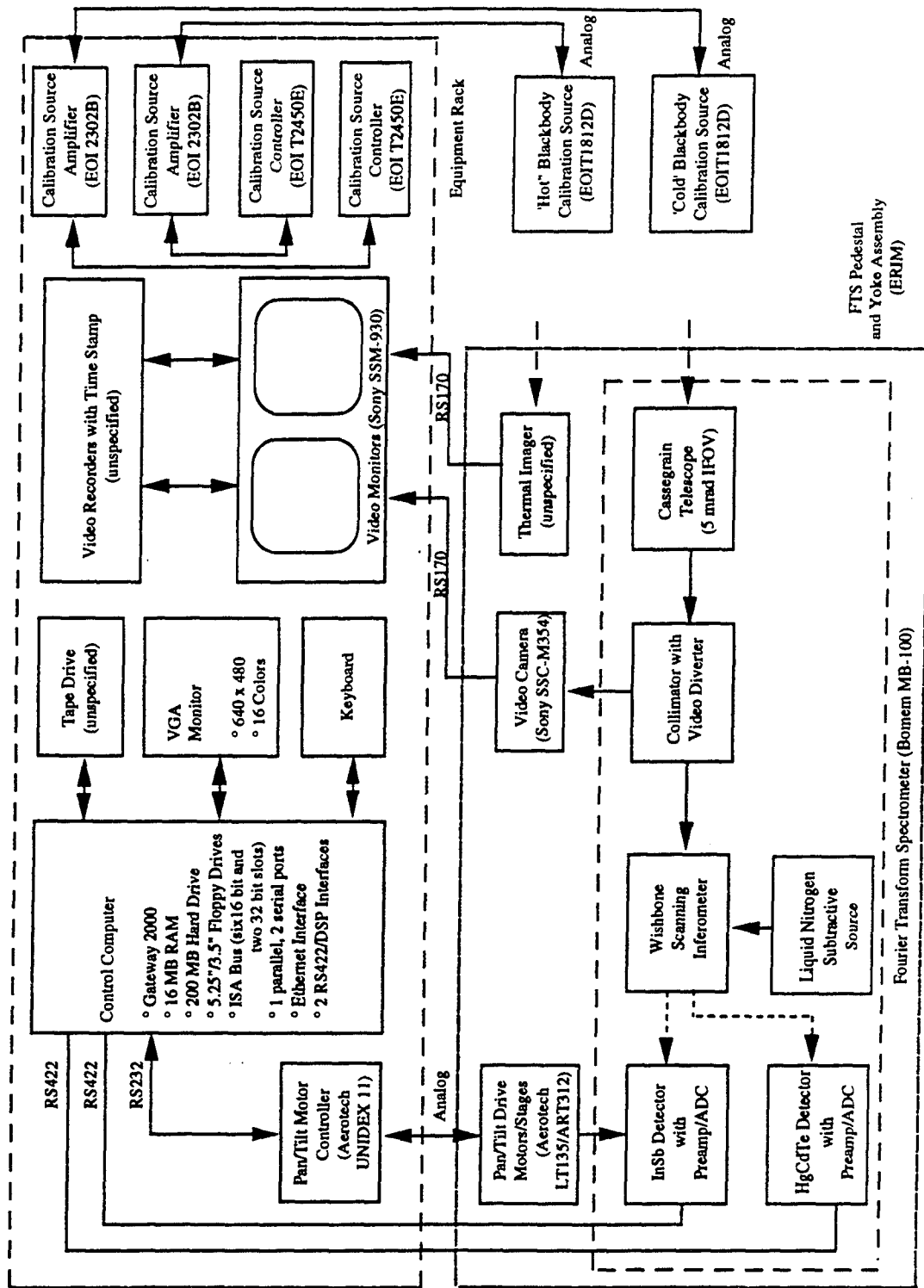


Figure 2-1. Field Spectrometer Systems Diagram

2.1.1.3 Radiometric Sensitivity

The radiometric sensitivity of the spectrometer should be sufficient to preserve background correlations on the order of 0.999 or better with typical day and night clutter levels, and to measure spectral mean differences due to emissivity differences of less than 0.01. Further analysis is provided in Section 5.

2.1.1.4 Measurement Fidelity

The calibration accuracy, stability, linearity, and polarization insensitivity of the spectrometer should be sufficient to preserve background correlations on the order of 0.999 with typical day and night clutter levels, and to measure spectral mean differences due to emissivity differences of less than 0.01. Further analysis is provided in Section 5.

2.1.1.5 Operation

The spectrometer must be completely operable in a field environment, such as from a tower or lift vehicle. Control of the spectrometer, including data acquisition, must be semiautomated (computer controlled) and be able to be performed remotely (e.g., 100 ft.).

2.1.2 Configuration

2.1.2.1 Bomem MB-100

The spectrometer configuration selected for the field measurements is a Bomem MB-100 Fourier Transform Spectrometer (FTS). An FTS design was selected because it inherently preserves correlation due to the use of a single detector per band (MWIR and LWIR) and the simultaneity of the spectral measurements. The MB-100 has been specifically designed by Bomem for radiometric measurements and field use.

The basic interferometer design of the MB-100 consists of a KBr beamsplitter with two cube corner retro-reflectors mounted on a wishbone scan arm (see Figure 2-2). As the arm pivots, an optical path difference is introduced between the arms of the interferometer, thereby scanning out an interferogram. The spectrum is produced by

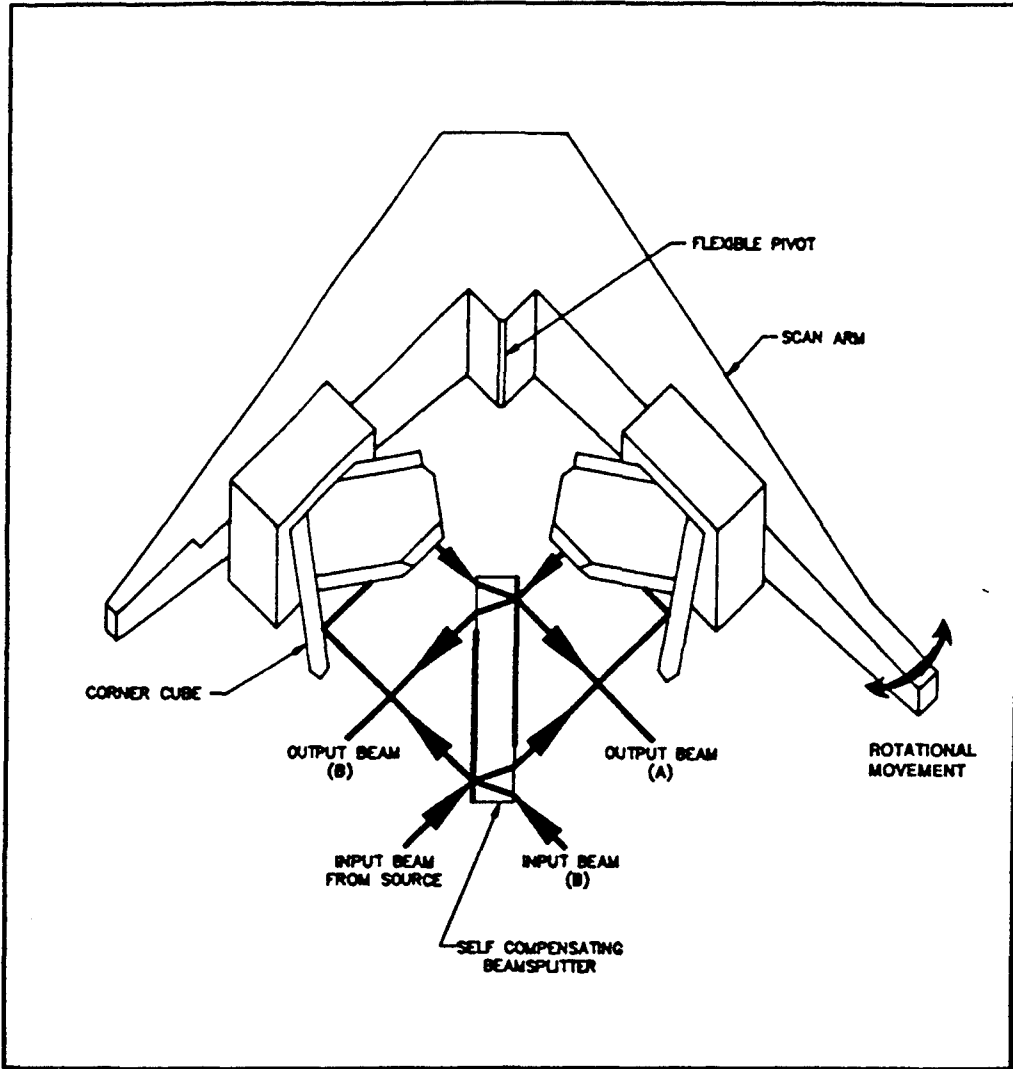


Figure 2-2. Schematic Drawing of MB-100 Interferometer on Wishbone Scan Arm.

sampling in conjunction with a reference HeNe laser beam and Fourier transforming this interferogram.

The optical design of the interferometer provides two complimentary inputs and outputs. In the exact configuration used, one of the inputs is directed to the target of interest, while the other is directed to a stable cold (liquid nitrogen) reference. The outputs are directed to two separate detectors an InSb detector for the MWIR (3-5 micron) spectral region, and an HgCdTe detector for the LWIR (8-12 micron) region. Both of these detectors are located at image planes of the pupil plane of the spectrometer through a common field aperture and secondary field apertures in each set of output optics. These apertures can be adjusted to tradeoff MWIR/LWIR spatial registration with radiometric sensitivity and stability.

2.1.2.2 Imaging Optics

The input optics of the FTS consist of a 10" Cassegrain telescope and a collimator assembly. All focusing optics are reflective. With the field limiting apertures open to their maximum diameter, the IFOV of the sensor is 5 mrad. A dichroic beamsplitter in the collimating assembly provides an optical output to a CCD camera, which provides boresight video through the common field limiting aperture. Figure 2-3 shows a side view of the FTS with the collimator and telescope attached.

2.1.2.3 Data Interface

The FTS operates in a free run mode and provides digital interferogram data through two separate interfaces (one for each detector). The interferogram is sampled in conjunction with an internal HeNe laser reference beam that propagates through the interferometer. An RS422 interface for each channel is utilized to allow remote data acquisition with the control computer. In addition, a DSP board (one for each channel) allows real time Fourier transformation of the acquired interferograms into complex spectra.

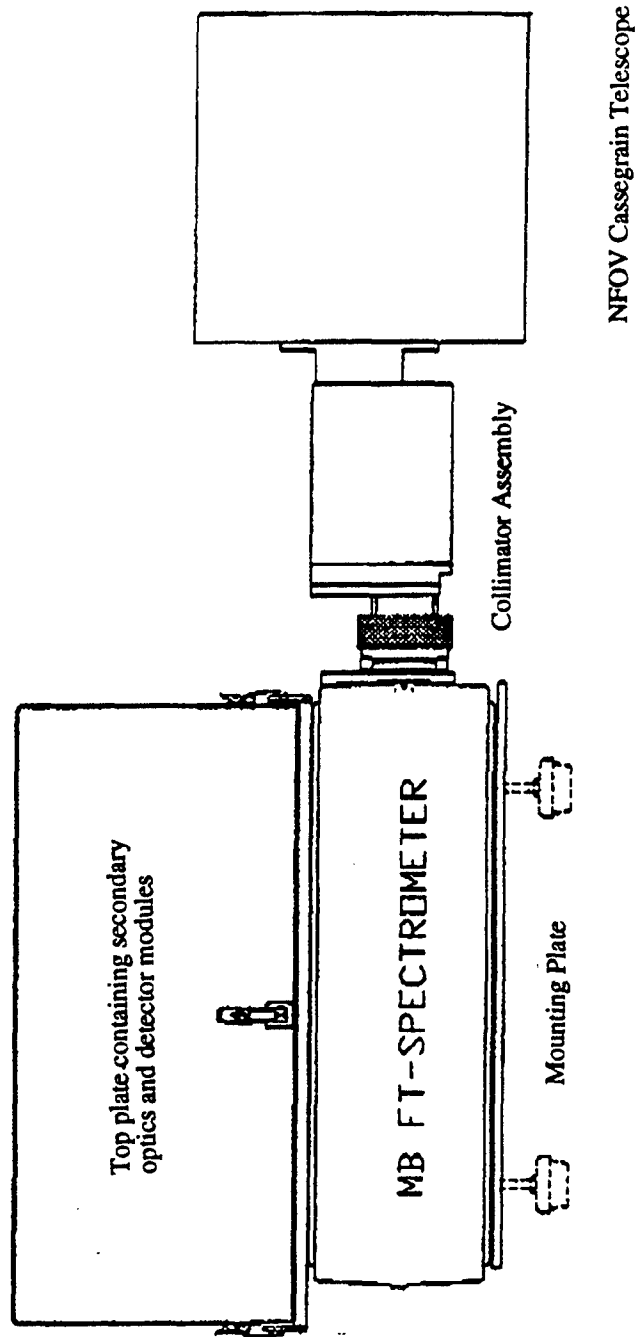


Figure 2-3. Side View of FTS With Collimator and NFOV Telescope.

2.1.3 Specifications

The following are specifications of the spectrometer configuration:

Spectral Range:	1,800 to 6,000 cm^{-1} (1.7 to 5.5 μm) with InSb detector 800 to 5,000 cm^{-1} (2.0 to 12.5 μ) with HgCdTe detector
Spectral Resolution:	1 to 128 cm^{-1} by factors of 2
Throughput:	0.0083 cmsr with 6.4 mm field stop (fully open)
Scan Rate:	1 cm/s (optical path difference) plus 0.15 sec turnaround time 0.8 sec for signals merged forward/reverse scan at 8 cm^{-1}
Input collimator:	14 cm focal length, 2.5 cm diameter
Cassegrain Telescope:	127 cm focal length, 25 cm diameter, less than 10% obscuration
IFOV:	5 mrad with 6.4 mm field stop (fully open)
NESR (estimated):	1.8×10^{-8} $\text{W}/\text{cm}^2\text{srcm}^{-1}$ for HgCdTe detector 1.8×10^{-9} $\text{W}/\text{cm}^2\text{srcm}^{-1}$ for InSb detector single merged forward/reverse scan, cosine apodization, 8 cm^{-1}
Sampling:	16 bit ADC up to 100 kHz rate
Interface	RS422 with 100 ft. cable length
Size (bounding box):	23" (W) x 16" (H) x 42" (L) 22.1" x 7.4" x 19.4" cast interferometer housing
Weight (estimated):	120 lbs.
Power:	115/230 VAC, 50/60 Hz, 140 VA maximum (75 VA typical)
Temperature Range:	-5 to 40C

As described above, the spectral resolution can be much finer than needed. Typically, we utilize 8 to 16 cm^{-1} resolution with 4x wavelength binning in the MWIR to provide roughly 75 to 150 nm wavelength bands across the entire spectral range.

2.2 RADIOMETRIC CALIBRATION EQUIPMENT

2.2.1 Design Requirements

The spectrometer is calibrated in the field through a two-point complex calibration procedure developed by Revercomb [2.1]. This is accomplished by alternately making

measurements of two extended area blackbody reference sources at different, known temperatures prior to each data collection sequence. In addition, such measurements can be repeated directly prior to and after each collection sequence to provide temporal calibration of linear FTS drift.

The calibration sources must provide greater than a 10" diameter calibrated surface with known spectral radiance across both the MWIR and LWIR spectral channels. The calibration error analysis described in Section 5 suggests that sources with 0.05 C absolute temperature accuracy, 0.03 C temperature stability, and a surface emissivity greater than 0.98 for wavelengths less than 4.2 microns and 0.99 above 4.2 microns will provide adequate system calibration. In addition, the sources must be suitably fieldable and be controllable via a remote computer.

2.2.2 Configuration

The calibration sources selected for the FTS measurements, Electro-Optical Industries Model T1812D, exhibit a 12" x 12" blackbody surface controlled by a large (10x10) array of matched thermoelectric modules with closed loop compensation in reference to a platinum resistance thermometer on the emitting surface. Temperature calibration is traceable to ITS-90 via NIST. The emitting surface is painted with Borden Krylon 1602 black paint, which is claimed to exhibit better than 0.99 emissivity in the LWIR band. A 12" deep sun baffle extends from the emitting surface to minimize stray reflected radiances. A second thermometer monitors baffle temperature. A perspective drawing of the calibration source is shown in Figure 2-4. In field use, each source is mounted on a stage light stand with a custom 0-45 degree tiltable mechanical interface.

The calibration sources are controlled by a Z-80 digital microprocessor based on temperature measurement through a precision ohmmeter. Temperature measurement, source control, and input/output functions are all contained in the Model T2450 E controllers. The Model 2302B power amplifiers provide additional amplification to drive the large arrays of thermoelectric modules.

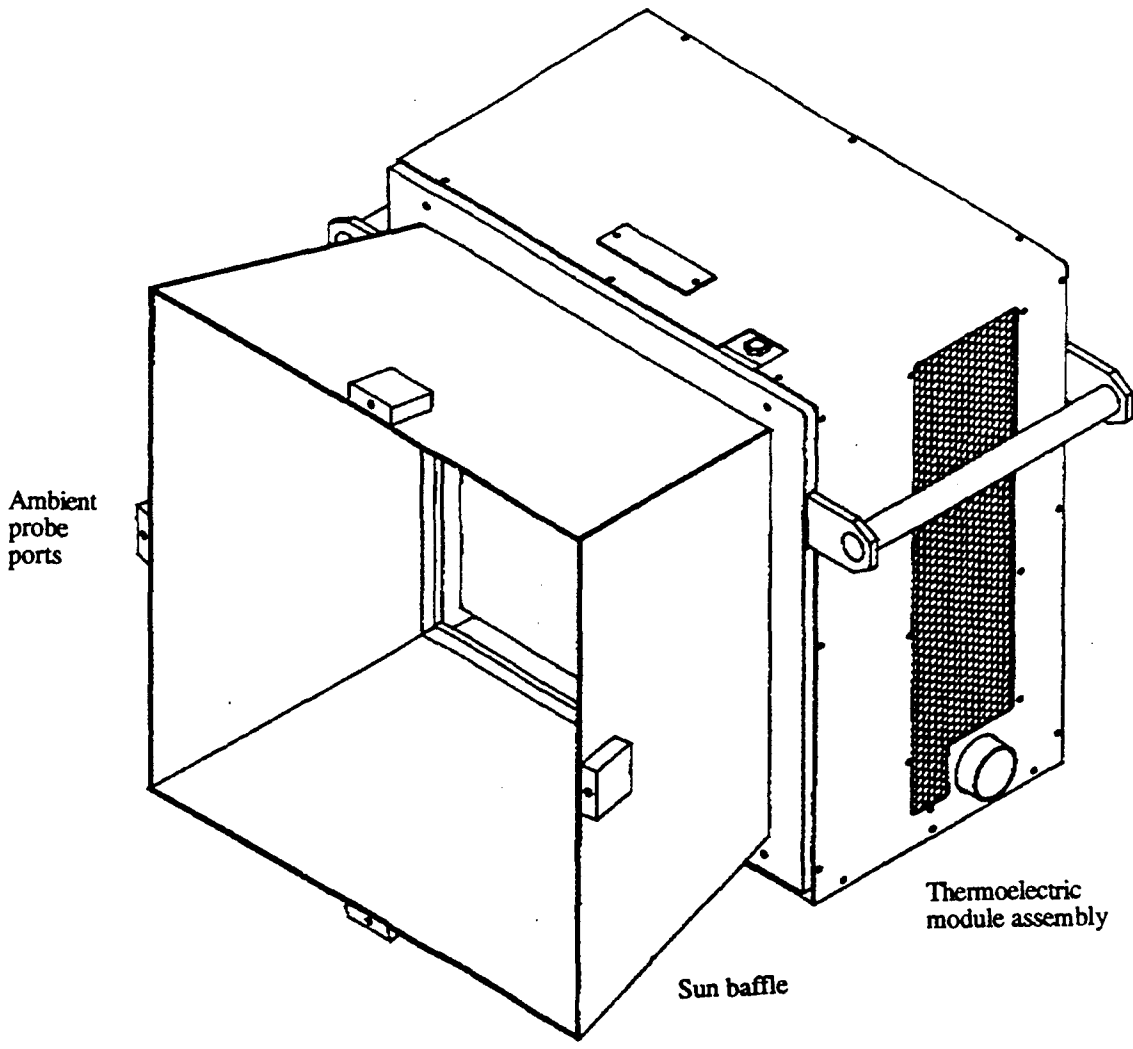


Figure 2-4. Perspective Drawing of Blackbody Calibration Source.

2.2.3 Specifications

The following are specifications for the calibration equipment:

Blackbody Sources:	EOI T1812 D
Calibrated Surface:	12" x 12"
Temperature Range:	0 to 50 C (at 25 C ambient)
Absolute Accuracy:	+/-0.03 C
Stability:	+/-0.003 C
Uniformity:	+/-0.01 C between +/-5 C from ambient
Emissivity:	>0.99 in LWIR band roughly 0.98 in MWIR band
Power:	drawn through power amp
Size:	14" x 14" x 9" (not including baffle)
Weight:	140 lbs.

Temperature Controller:	
Type:	EOI T2450 E
Temperature Measurement:	Precision ohmmeter
Microprocessor:	Z-80
Display Resolution:	0.01 C
Set Point Resolution:	0.01 C
Remote Interface:	RS232
Power Requirements:	110/115/200/230 VAC, 50-400Hz, 250 W
Size:	19"(W) x 18"(D) x 5.2"(H)
Weight:	approx. 40 lbs.

Power Amplifier:	
Type:	EOI 2302 B
Power Requirements:	200/230 VAC, 50-400 Hz, 1500 W
Size:	19"(W) x 18"(D) x 7"(H)
Weight:	approx. 100 lbs.

2.3 AZIMUTH/ELEVATION MOUNT

2.3.1 Design Requirements

In order to acquire the correlation and contrast data of interest, it is necessary that the spectrometer be mounted on a pedestal with provisions for rapidly steering the line-of-sight to a sequence of predetermined locations under computer control. The field of regard should accommodate depression angles of 5 to 60 degrees and azimuthal range of 180 degrees. Stability and repeatability should be better than a tenth of the sensor

Ifov. Obviously, the mount and steering motors must be suitably chosen to accommodate the weight and inertia of the FTS (roughly 120 lbs. and 100,000 in² lb).

2.3.2 Configuration

The configuration for the azimuth/elevation mount, depicted in Figure 2-5, is a yoke assembly consisting of two motorized rotary stages mounted on a large tripod. The rotary stages (Aerotech ART312) are 12 inches in diameter and provide extremely precise positioning via high quality angular contact bearings and a precision oil-filled worm drive. Each of the stages is driven by a pulse width modulated (pwm) dc servo motor (Aerotech LT135) equipped with a rotary encoder to provide closed loop position feedback and velocity stabilization. Motor control occurs via a Unidex 11 digital controller, which allows point-to-point pan/tilt through either front panel programming, a proportional speed joystick, or an RS232 interface. The yoke assembly was designed with adequate rigidity for 1 arc min stability.

2.3.3 Specifications

The following are specifications for the pan/tilt mount:

Rotary Stages:	
Type:	Aerotech ART312
Range:	+/-60 degrees (tilt); +/-180 degrees (pan)
Gear Ratio:	1081
Resolution:	0.05 arc min (4000 steps per revolution on motor shaft)
Accuracy:	0.5 arc min
Repeatability:	0.1 arc min unidirectional
Wobble:	5 arc sec
Load Capacity:	250 lb (axial), 200lb (radial)
Output Torque:	400 in lb (with LT135 motors)
Slew Rate:	0.2 to 3000 deg/s
Acceleration:	88 deg/s ² (tilt with 100,000 in lb inertial load) 18 deg/s ² (tilt with 500,000 in lb inertial load)
Size:	12 inches diameter x 5 inches high
Weight:	40 lb with LT135 motor

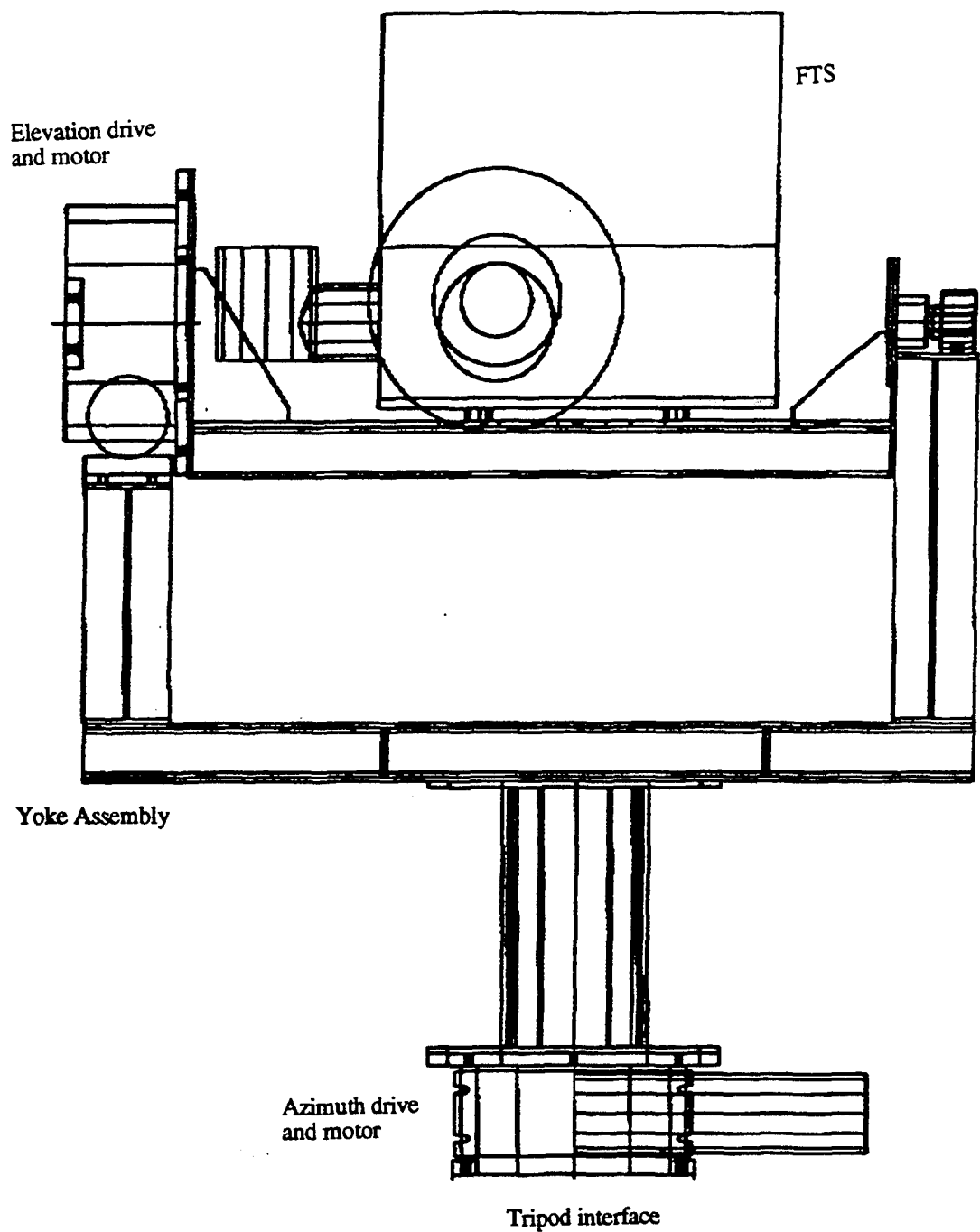


Figure 2-5. Azimuth/Elevation Mount Assembly Including Drive Stages and Payload (FTS).

Motors/Encoders:

Type: Aerotech LT135 pwm servo
Stall Torque: 135 oz in continuous
Peak Torque: 736 oz in
Maximum Speed: 5000 rpm
Resolution: 4000 steps per revolution (1000 encoder lines)
Interface: NEMA 34
Size: 3.25 inches diameter x 9 inches long
Weight: 8 lbs.

Controller:

Type: Aerotech Unidex 11
Axes: 2
Motion: Point-to-point with designated peak angular velocity
and linear or parabolic acceleration profile
Interfaces: RS232 and proportional speed joystick
Size: 10.5" (H) x 19.0" (W) x 19.25" (D)
Weight: 42 lbs.
Power: 115 VAC, 50/60 Hz, 1000 VA (max)
Temperature Range: 0 to 50 C

Yoke Assembly:

Type: ERIM fabricated
Material: Aluminum
Size: 34.7"(W) x 19.1"(D) x 31"(H)
Weight: approx. 80 lbs. (without rotary drives)

2.4 CONTROL AND DATA ACQUISITION SYSTEM

2.4.1 Design Requirements

The control and data acquisition system must be field portable and capable of interfacing with the FTS, motor controller, blackbody controllers, as well as all possible data analysis platforms. A PC-based system is required for FTS compatibility. Due to the large amounts of data collected (on the order of 2 MB per experiment), it is essential that the system provide a rapid data acquisition capability, sufficient RAM and hard disk storage capacity, and a tape backup capability.

2.4.2 Configuration

Figure 2-6 illustrates the primary components of the control and data acquisition system. The basic system is a Gateway 4DX-33V computer with a 80486DX processor and 16MB RAM, equipped with several ISA boards to provide the FTS (RS422), motor controller (RS232), and network (Ethernet) interfaces.

2.4.3 Specifications

The following summarizes the overall system:

Computing Platform:

Type:	Gateway 2000 4DX-33V PC
CPU Type:	Intel 80486DX/33
Expansion Slots:	Six 16-bit ISA, two 32-bit VESA
Cache:	8 kB primary, 64 kB secondary
RAM:	8 MB (expandable)
Hard Disk:	Western digital IDE (200 MB, 13 ms)
Floppy Disk:	One 5-1/4" drive, one 3-1/2" drive
Graphics Adapter:	ATI Graphics Ultra Pro (EGA/VGA)
I/O Ports:	One parallel, two serial (RS232)
Operating System:	MS-DOS 5.0 (Microsoft)
Software Development:	C++ (Borland)
Size:	16.25" x 16" x 4.25"
Power Supply:	110 VAC, 200 Watt

SCSI Controller:

Type:	Adaptec AHA-1542C
Interface:	ISA/SCSI
Software:	ASPI DOS manager (Adaptec)

Tape Drive:

Type:	Archive Model 2150S
Interface:	SCSI
Format:	QIC-150
Density:	150 MB
Software:	DOSTAR (Cactus International)

Ethernet Interface:

Type:	Racal Interlan NI6510
Interface:	ISA/IEEE 802.3 10 base 5
Software:	Telnet/FTP (NCSA)

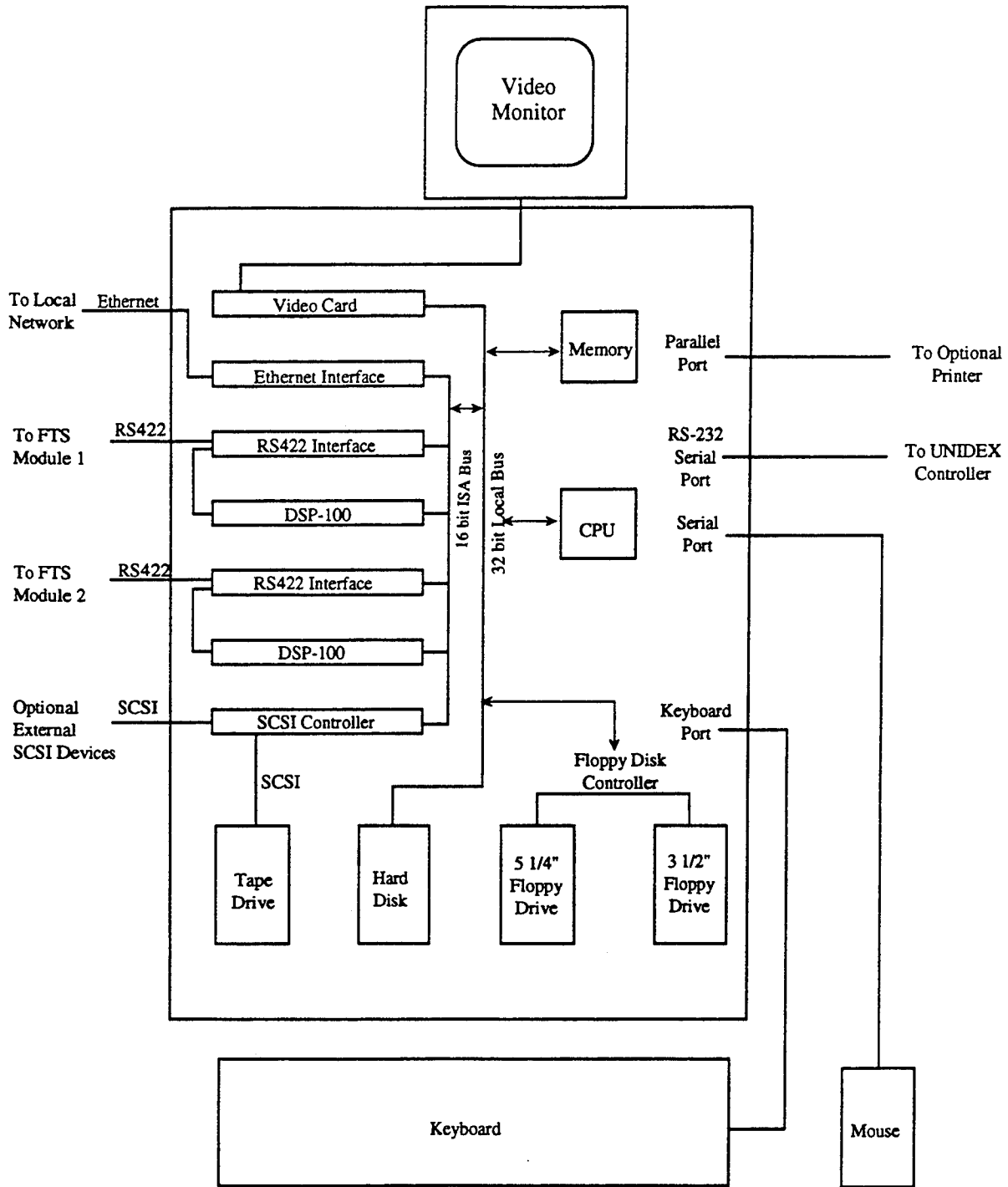


Figure 2-6. Control and Data Acquisition System Block Diagram.

Motor Controller Interface:

Type: Serial (RS232) port
Configuration: 9600 baud, 8 data bits, 1 stop bit, no parity
Software: C++ I/O library (Borland)
Cable Length: 30 meters

FTS Interface:

Type: Two Bomem SEQ136
Interface: ISA/RS422
Cable Length: 30 meters

Digital Signal Processor:

Type: Two Bomem DSP-100
Interface: ISA
Software: Radiometric Software (Bomem)
Lab Calc (Galactic Industries)

2.5 BORESIGHT VIDEO EQUIPMENT

2.5.1 Design Requirements

Boresight video is required to set up the spatial scan sequence for an FTS data collection experiment and, during daytime hours, monitor and record a visual rendering of the measured target and background patches. A dichroic video diverter is included in the FTS collimator that allows a video camera to monitor the scene through the FTS telescope and front aperture. The mechanical interface is C-mount and imaging optics are contained within the collimator assembly (see Figure 2-7), but no exposure control is provided. Therefore, the boresight video camera must provide an electronic shuttering capability. The imaging optics are designed for a 1/2" or 2/3" camera format. The video recording must provide a time-stamp capability for data synchronization.

2.5.2 Configuration

The configuration for the boresight video equipment consists of a black-and-white 1/2" format CCD camera, two 9-inch black-and-white monitors, and a VHS time-stamp recorder. Each is contained in the system diagram illustrated in Figure 2-7.

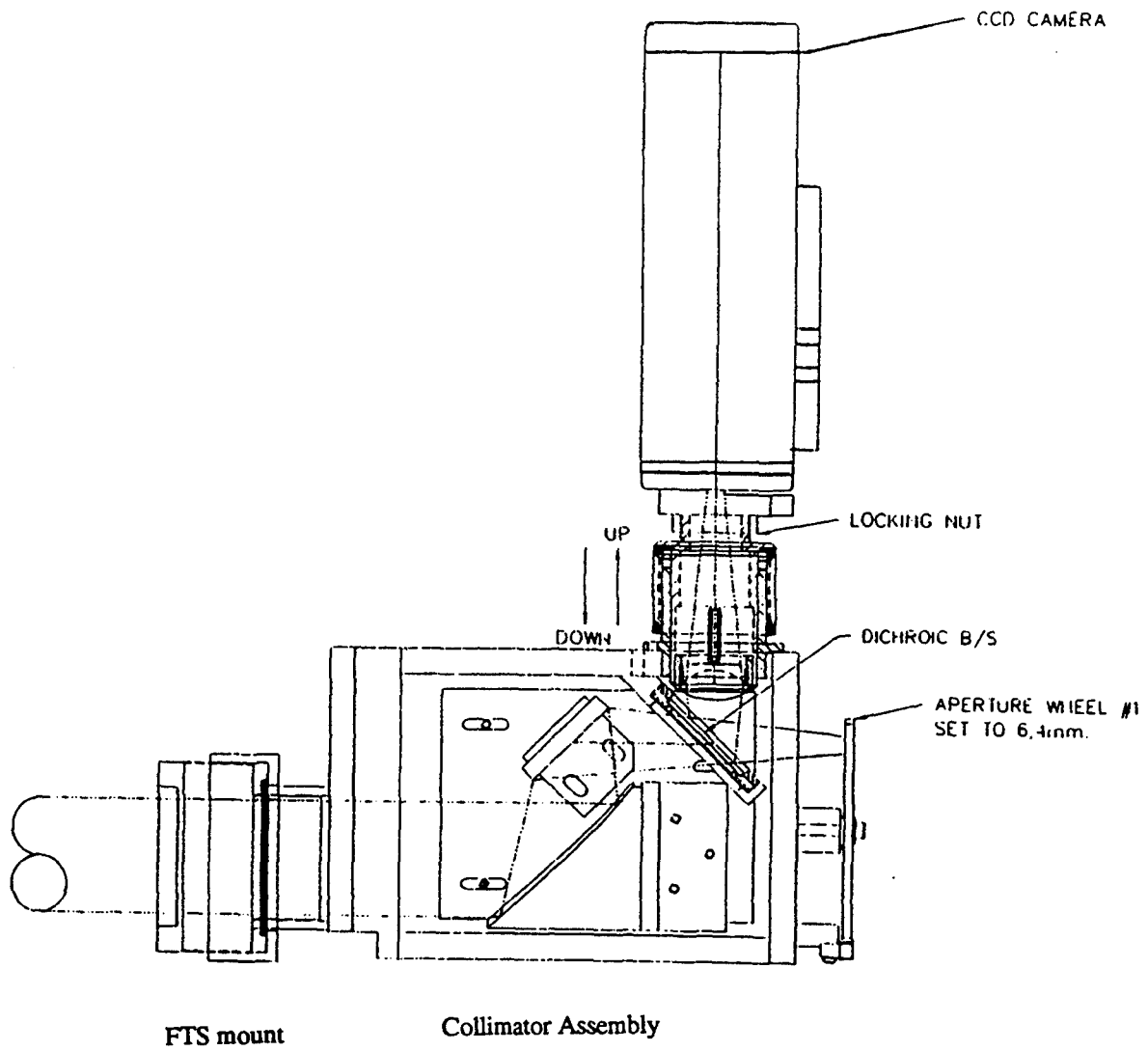


Figure 2-7. Boresight Video Camera Interface Schematic.

2.5.3 Specifications

The following contains a summary of the boresight video equipment specifications:

Video Camera:

Type:	Sony SSC-M354
Detector:	Interline transfer type CCD
Sensing Area:	6.3 x 4.7 mm (1/2" format)
Lens Mount:	C-Mount
Signal System:	NTSC; 21 interlace
Resolution:	510 x 492 (H/V)
Video Output:	1.0 V pp, 75 ohms
Sensitivity:	0.3 lux at f/1.2 (AGC on)
S/N Ratio:	48 dB (AGC off)
Electronic Shutter:	8 settings 1/60 sec to 1/10000 sec
Power Requirements:	24 VAC, 60 Hz, 4.0 W
Size:	64 x 57 x 155 mm
Weight:	660 g

Video Monitor:

Type:	Sony SSM-930
System:	EIA standard
Picture Tube:	9" diagonal black and white
Resolution:	More than 750 TV lines
Impedance:	75 ohm or high impedance
Power Requirements:	120 VAC, 60 Hz, 27 W
Size:	220 x 219 x 246 mm
Weight:	5.8 kg (13 lb)

Video Recorder:

Type:	Panasonic Model AG-1050
TV System:	EIA standard, NTSC color system
Recording System:	2 rotary heads
Tape Format:	VHS
Tape Speed:	SP or SLP
Input Level:	1.0 V p-p, 75 ohms
Horizontal Resolution:	240 lines
S/N Ratio:	45 dB (SP)
Power Requirements:	120 VAC, 60 Hz, 20W
Size:	270 (W) x 120 (H) x 339 (D) mm
Weight:	11.7 lbs

2.6 REFERENCES

- [2.1] H.E. Revercomb, et al., "Radiometric Calibration of IR Fourier Transform Spectrometers: Solution to a Problem with the High-Resolution Interferometer Sounder," *Applied Optics*, Vol. 27, No. 15, pp. 3210-3218, 1 August 1988.

3.0 QUICK LOOK SOFTWARE

3.1 OVERVIEW

The Quick-Look software package is a tool used to analyze signatures collected by the Bomem Fourier Transform spectrometer. The package was developed with Borland C++, V3.1 for use on an IBM-compatible PC and should support a number of graphics drivers. The menu-driven software allows you to view spectra and related statistical quantities. The user can also save displayed quantities to the disk in ASCII and binary formats.

Because of the potentially large amount of memory required for some of the functions, a version of the software is provided that accesses available extended memory by linking with the Phar Lap DOS Extender Libraries via their 286 DOS Extender Software Development Kit. If you do not have the Phar Lap 286 DOS Extender, then you cannot use the extender version of the Quick-Look package. If you would like to purchase the extender, contact Phar Lap (based in Cambridge, MA).

As of September 1993, Borland C++ does not support the 32-bit 386 and 486 processors running under DOS. If and when such a compiler is released, we intend to rebuild the Quick Look utility. If Phar Lap supports the new compiler, we will likely rebuild the extender version of the package as well.

3.2 INSTALLATION OF THE DOS EXTENDER

To use the DOS extender version of Quick-Look, the Phar Lap 286 SDK should be installed according to the installation instructions provided for Borland C, Version 3.0 (BC3). Note that for software development, some Borland C libraries are required; however, to simply use the extender version of Quick-Look, these libraries are not required.

After the Phar Lap extender is installed, there are a couple things left to do before running Quick-Look. First of all, the directory `\run286\bin` must be in your path. Modify the `autoexec.bat` file to achieve this. This was likely done during installation, but check to make sure. To link Quick-Look with the extender, copy the file `\run286\bc3\fp286.lib` to `\run286\bc3\fp286.obj`. This may not be required to actually

run the software, but it does not hurt to make this change now, especially if you want to recompile in the future. Next, replace the file graph286.lib in the \run286\bc3\lib directory with the graph286.lib provided with Quick-Look software. You may want to save the existing graph286.lib in a back-up file before replacing. Last of all, replace the file graphics.dll in the \run286\bin library with the graphics.dll file provided with the Quick-Look software. You may want to save the existing graphics.dll in a back-up file before overwriting. This file contains the dynamic link library used to run the Quick-Look graphics.

If you encounter serious problems running qlext.exe, please contact the Phar Lap technical support people. They are extremely helpful.

3.3 REBUILDING QUICK-LOOK WITH BORLAND C PROJECT FILES

If you have Borland C installed on your system, it is possible to recompile and relink the original source code. Two project files are provided for rebuilding Quick-Look within the Borland IDE: qllook.prj and qlext.prj. Both project files use the same source code, but link differently. If rebuilding the extender version qlext.exe, consult the Phar Lap 286 SDK installation instructions above. If rebuilding qllook.exe, first copy the file graphics.lib provided with the source code into the \borlandc\bgi directory. This file is linked to when building qllook.exe, and contains various graphics drivers.

3.4 RUNNING QUICK-LOOK

The executable versions of the Quick-Look package are qllook.exe (normal) and qlext.exe (DOS extender). The descriptions that follow below apply to both versions of the software.

3.4.1 Default File, QLOOK.DEF

Upon execution, Quick-Look looks for a file in your CURRENT directory called qllook.def. This file contains 4 default setting that can be overridden within the program, but which are more conveniently set automatically each time the program is launched. They are:

1. **BW:** Bandwidth in nanometers for binning the spectra. For each wavelength sample in a spectrum, neighboring wavelength samples are averaged to yield the specified bandwidth in nanometers, centered about the given wavelength. If the bandwidth is set to 0.0, no binning is performed, and the raw data is used. Note that if the bandwidth is too small, there could be no binning at longer wavelengths, since the inherent bandwidth of the data collected by the spectrometer would exceed the user-specified bandwidth.
2. **DECIMATE:** Integer decimation factor (Default == 1, no decimation)
3. **RANGE:** Range of wavelengths (in microns) over which to work. As an example, one may wish to only process long-wave data, and would specify: RANGE 8.0 12.0
4. **NESR_FILE:** Noise-equivalent spectral radiance sensor noise characterization file used to predict the maximum correlation that can be measured. Three files with ".nes" extensions have been provided along with the software. The required file depends on the spectrometer configuration during the particular experiment. This should be clear from the collection documentation.

You should set the parameters in this file to your preference. If qlook.def is not found, Quick-Look will remind you to set these parameters manually within the program. An example qlook.def file has been provided with the software.

3.4.2 Required Experiment Files

Almost every Quick-Look utility prompts you for an experiment name. This is the filename prefix to all experiment-related files, and is most likely the name of the directory containing the various files. These files will be called experiment.spc (contains the spectra), experiment.grt (ground truth file), experiment.set (Bomem sensor settings), etc. When you are prompted for an experiment name, leave off any 3-character extensions.

There are some basic files that you will need to run most of the utilities:

experiment.spc: Data file
Format: Bomem "LabCalc" format (not human-readable)

experiment.grt: Ground truth file (ASCII)

Format:

```
target1 first_subfile last_subfile
target2 first_subfile last_subfile
.
.
.
targetN first_subfile last_subfile
```

NESR file: NESR file (ASCII, independent of any experiment)

Format:

```
wavenumber1 NESR1
wavenumber2 NESR2
.
.
.
wavenumberN NESRN
```

The spectral correlation function also requires a .set file that specifies the number of co-added scans, and the spatial correlation and spatial-spectral coherence functions require a .ptm file for determining the angular resolution of a line scan. Normally, the user does not have to worry about these files, as they should all be in one place for a given experiment. If a required file is missing, the user will be notified by Quick-Look.

3.4.3 Quick-Look Functions

The Quick-Look software has the following utilities, accessed by scrolling through menus using the Up-arrow and Down-arrow keys. See the section below on plotting capabilities for options while viewing a plot. The competition of confidence bounds is described in Appendix A.

1.0 View Spectra

This allows you to view an individual spectrum or all the spectra from a given scene found in the ground truth file.

2.0 Mean-based Measurements

- A. Single mean - plot a mean with confidence bounds (see H. below).
- B. 2 means - plot two means (targ and bkgnd) with conf. bounds.

- C. Mean contrast - plot the difference between two means (target and background) with confidence bounds.
- D. Mean contrast SCR - divide absolute value C. above by std dev of the background, plotted with conf. bounds. Because the absolute value of the mean contrast is plotted, the plot changes colors when the sign of the contrast reverses. Plotted in units of dB, but the space bar can be used to toggle between dB and non-dB units.
- E. Mean contrast eff SCR - effective SCR, similar to D. above, but uses target variance. No confidence bounds are available. Plotted in units of dB, but the space bar can be used to toggle between dB and non-dB units.
- F. Required samples (target) - Required number of samples to be X% certain an estimated mean is within a specified number of microflicks of the true mean.
- G. Reqd samps (trg+bkgnd) - Same as F. but for both a target and a background.
- H. Set confidence level - Choice of 90, 95 and 99% confidence. *This is a global setting and applies to all plots with confidence levels. Default = 90%*

A note about A-C above: all mean and standard deviation calculations are performed with radiance units. However, for display purposes the user is given the additional choices of normalizing out temperature with the Planck function or converting to apparent temperature. *Remember that calculations are made in radiance units and the conversion to other units is made just prior to displaying.*

3.0 Standard Deviation

- A. Single std. dev - plot a standard deviation with confidence bounds (see C. below). The space bar can be used to toggle between std. dev. and variance.
- B. 2 std. dev. plots - display two std. dev plots (targ and bkgnd) with conf. bounds. Use the space bar to toggle between std. dev. and variance.
- C. Set confidence level - See 2.0, H. above.

A note about A and B above: all standard deviation calculations are performed with radiance units. However, for display purposes the user is given the additional choices of normalizing out temperature with the Planck function or converting to apparent

temperature. *Remember that calculations are made in radiance units and the conversion to other units is made just prior to displaying.*

4.0 Spectral Correlation

- A. 2-D correlation plot - plot the correlation between all band-pairs on a 2-D plot. Clutter suppression (dB) is plotted to squash the dynamic range. Correlation values can be viewed by toggling back and forth with the space bar.
- B. Single-band correlation - Correlate a single band with all other bands. Plotted with confidence levels and maximum attainable correlation (using NESR data).
- C. Multi-band correlation - Same as above, but for more than one band (up to 7) *without* confidence levels.
- D. Required samples - Required samples for desired, one-sided correlation confidence. The confidence, delta-rho, is specified in terms of the ratio of delta-rho to 1-rho. As an example, if the ratio specified is 0.5 and the measured correlation is 0.99, then delta-rho would equal 0.005, and the number of samples required to be X% confident that the measured correlation were within 0.005 of the true correlation are displayed.
- E. Read NESR file - If the NESR file was not specified in the qlook.def file and is required for one of the above functions, then it can be read here.
- F. Set confidence level - See 2.0, H. above.

5.0 Spatial Correlation

- A. Single band correlation - estimate the correlation length on a single-band basis. Currently, a region about the auto-correlation peak is plotted along with the exponential fit versus either milliradians or meters, and the $\exp(-1)$ point is reported.
- B. Plot correlation length - plot the correlation length as a function of wavenumber. If plotted in terms of angle, the space bar can be used to toggle between milliradians and degrees.

6.0 Spatial/Spectral Coherence

This function requires a series of line scans from the Bomem spectrometer. After specifying the scans, the user selects two bands, after which he can generate the complex-valued, 1-D auto- and cross-spectral densities for these two bands. There are spatial- and frequency-domain weighting and averaging options, the user can plot the magnitude or the phase, and there is a normalization option that allows the user to plot the cross-coherence coefficients. The densities are plotted on a dB scale, and the coherence coefficients are plotted in units of clutter suppression (dB). Use the space bar to toggle between dB and non-dB units.

7.0 Dual-band, 1-D performance metrics

- The metrics are computed for one band with respect to all other bands

- A. Color ratio
- B. Dual-band SCR (with confidence bounds, plotted on dB scale)
Use the space bar to toggle between dB and non-dB units.
- C. Dual-band SCR multispectral gain (plotted on dB scale)
Use the space bar to toggle between dB and non-dB units.
- D. Dual-band effective SCR (plotted on dB scale)
Use the space bar to toggle between dB and non-dB units.
- E. Dual-band effective SCR multispectral gain (plotted on dB scale)
Use the space bar to toggle between dB and non-dB units.

8.0 Dual-band, 2-D performance metrics

- The metrics are plotted for all band-pairs

- A. Color ratio
- B. Dual-band SCR (plotted on dB scale)
Use the space bar to toggle between dB and non-dB units.
- C. Dual-band SCR multispectral gain (plotted on dB scale)
Use the space bar to toggle between dB and non-dB units.
- D. Dual-band effective SCR (plotted on dB scale)
Use the space bar to toggle between dB and non-dB units.
- E. Dual-band effective SCR multispectral gain (plotted on dB scale)
Use the space bar to toggle between dB and non-dB units.

9.0 Dual-band Scatter plots

This utility will display a 2-D scatter plot of the radiance in two bands of up to 12 "scenes" (panel, grass, truck)

10.0 Dump Spectra

All the spectra for a given scene will be dumped into a series of ASCII files with a user-specified suffix and a spectra-index prefix. For example, the 3

spectra associated with the user-specified suffix MYSCENE would be dumped into MYSCENE.0, MYSCENE.1 and MYSCENE.2.

11.0 Binning/Decimation/Offset

- A. Binning - specify the desired bandwidth in nanometers. Can be set in qlook.def file.
- B. Decimation - specify the integer decimation factor (none==1). Can be set in qlook.def file.
- C. Range - specify the range of wavelengths (in microns) over which to work. Can be set in qlook.def file.
- D. Plot Bandwidth - useful diagnostic, but otherwise ignore

3.4.4 Plotting Capabilities, Hidden Functionality, Saving Plots

The plots have slide bars that can be moved to display the plotted values. Along the slide bars the wavelength in microns is displayed. (Almost all of the plots are in wavenumbers, so this is quite handy). For 1-D plots, an ascii output can be obtained by typing the letter "o" while viewing the plot. Typing "o" while viewing a 2-D plot will allow you to dump a binary output file. However, ascii files are dumped in the case of a 2-D scatter plot. Also, for 1-D plots, the y-axis range can be modified by typing the letter "r" while viewing the plot. This function can also be used to change both the x-axis and y-axis ranges while viewing a 2-D scatter plot.

A note about 2-D plots. You are encouraged to decimate initially when attempting 2-D plotting to save computation time. Also, because memory is at a premium without the DOS extender, you will be restricted without the extender in the size of the plots.

The following key-stroke functions are available with the plotting routines:

1-D plots:

Right arrow - move slide bar right

Left arrow - move slide bar left

Cntl-right-arrow - fast move

Cntl-left-arrow - fast move

Home - move to beginning of plot

End - move to end of plot

Space bar - toggles between plotted units and transformed units:

Correlation: toggles between dB clutter suppression and correlation

Correlation length: toggles between milliradians and degrees

Signal to Clutter Ratio (SCR): toggles between dB and non-dB units

Std. Deviation: toggles between std. dev. and variance

- Spectral densities: toggles between dB and non-dB units
- o - output plot to ASCII file. It is important to realize that the units of the data saved to the file depends on the toggle setting (if applicable) at the time output is requested. As an example, if plotting correlation in units of dB clutter suppression, to dump actual correlation values, the space bar should be used to toggle to correlation prior to selecting "o" for output. *THIS FUNCTION EXITS THE PLOT.*
 - r - change y-axis range
 - Return - exit

2-D plots:

- Right arrow - move slide bar right
- Left arrow - move slide bar left
- Up arrow - move slide bar up
- Down arrow - move slide bar down
- Cntl-right-arrow - fast move
- Cntl-left-arrow - fast move
- Cntl-up-arrow - fast move
- Cntl-down-arrow - fast move
- Home - move to left edge of plot
- End - move to right edge of plot
- PgUp - move to top of plot
- PgDn - move to bottom of plot
- Space bar - toggles between plotted units and transformed units:
 - Correlation: toggles between dB clutter suppression and correlation
 - Signal to Clutter Ratio (SCR): toggles between dB and ratio units
- o - output plot to binary file. It is important to realize that the units of the data saved to the file depends on the toggle setting (if applicable) at the time output is requested. As an example, if plotting correlation in units of dB clutter suppression, to dump actual correlation values, the space bar should be used to toggle to correlation prior to selecting "o" for output. *THIS FUNCTION EXITS THE PLOT.*
- r - 2-D scatter plots only: change x-axis and y-axis range
- Return - exit

DISCLAIMER: THE QUICK-LOOK PACKAGE IS RESEARCH-GRADE CODE AND, THUS, PLACES NUMERICAL FIDELITY ABOVE USER-FRIENDLINESS. WE WELCOME ANY COMMENTS REGARDING BUGS IN THE CODE, BUT DO NOT INTEND TO SUPPORT NON-TECHNICAL ENHANCEMENTS.

4.0 FTS SENSOR CHARACTERIZATION TESTS AND RESULTS

This section contains a summary of the objectives, procedures, and results of a series of tests performed to evaluate the performance of the FTS sensor, specifically with regard to making in-situ spectroradiometric contrast and correlation measurements of ground-based targets and backgrounds. The FTS sensor consists of four primary components a Bomem MB-100 Fourier Transform Spectrometer outfitted for field radiometric measurements, two Electro-Optical Industries (EOI) T1812D large area blackbody calibration sources, a computer controlled azimuth/elevation mount, and a PC-based control and data acquisition system. Details of the sensor configuration can be found in Section 1.

The tests were performed at a variety of locations, including the WL Avionics Lab tower, the WL Materials Directorate Optical Measurements facility, and the MICOM Russell Measurement Facility. The following performance properties were quantified sensor noise, absolute calibration accuracy, relative calibration accuracy, temporal radiometric stability, response linearity, polarization sensitivity, spatial registration, correlation preservation, pointing repeatability, and pointing stability. The remainder of this section successively addresses each of these properties, including discussion of the test objectives, test procedure, error sources, sensor modifications employed to minimize errors (where applicable), test results and conclusions.

Table 4-1 provides a brief overall summary of the sensor characterization test results.

4.1 SENSOR NOISE

Sensor noise produces a variance in the spectral measurements, which results in an uncertainty in measured contrast as well as a correlation measurement limit. Integration techniques can be employed to reduce sensor noise. Such integration can be performed spectrally by decreasing spectral resolution or temporally by increasing integration time. For a single spectral scan, these are naturally tied together since a longer integration time assumes a larger mirror displacement (constant scan rate) and therefore finer spectral resolution. Post-processing integration can also be employed,

Table 4-1: Sensor Characterization Test Summary

Effect	Limiting Factors	Modifications	Anticipated Performance	Measured Performance
Noise	Detector Performance	None	NESR=1.8 nW/cm ² sr cm ⁻¹ (MWIR) 18 nW/cm ² sr cm ⁻¹ (LWIR)	NESR=1 nW/cm ² sr cm ⁻¹ (MWIR) 6 nW/cm ² sr cm ⁻¹ (LWIR)
Absolute Calibration Accuracy	Blackbody non-unity emissivity	None	3-5% miscalibration	±1% miscalibration
Relative Calibration Accuracy	Blackbody instability Noise	None	0.3% miscalibration	miscalibration <0.15% (LWIR) <0.25% (MWIR) (greater for λ <4μm due to noise)
Temporal Radiometric Stability	Detector instability Stray radiance	Replaced reentrant dewar Collimator thermal blanket Increased front aperture Temporal calibration	unknown	Uncorrected instability≈0.1-0.15% Corrected instability ≈0.03-0.05% (over 20-30 min time frame)
Linearity	Detector nonlinearity	None	Limited to nonlinearity of blackbody function	Roughly blackbody limited (within measurement limits)
Polarization Sensitivity	Video diverter coating Beamsplitter coating	None	unknown	Varies from 3.5 to 9.1% over 4-12μm (with video diverter) Varies from -2.0 to 2.9% over 4-12μm (without video diverter)
Spatial Registration	Module to module misregistration	None	Better than IFOV/50	Better than IFOV/50 within LWIR and MWIR, IFOV/14 between LWIR/MWIR
Correlation Preservation	Sensor instability Noise	Temporal calibration	>0.9995 for 1 degree rms temperature blackbody (limited further <4μm by noise)	>0.9999 within LWIR >0.9995 MWIR to LWIR noise limited in MWIR (>0.9995 above 4μm)
Pointing Repeatability	Rotary stage runout and backlash	None	0.5 arc min bidirectional 0.1 arc min unidirectional	0.6 arc min bidirectional <0.15 arc min unidirectional
Pointing Stability	Pointing system rigidity Telescope vibration (wind) Platform (tower) stability	None	1 arc min steady state unknown transient	0.15 arc min steady state in calm environment 1 arc min steady state in windy environment 2 arc min transient instability for >5-10° displacements (settling time≈1 sec)

either by summing a series of spectral scans or by smoothing the resulting spectrum (spectral convolution). Assuming the noise is spectrally and temporally uncorrelated, a \sqrt{N} decrease in the relative noise level will result where N is the number of summed spectral scans and/or spectral channels.

The objectives of the sensor noise tests were to understand the sensor trades with regard to noise. In particular, this involves determining the most suitable spectral resolution setting and the resulting noise level as a function of wavelength for each of the FTS detectors (InSb from 3-5.5 μm , MCT from 3-12 μm).

The figure of merit used to characterize noise performance is the noise equivalent spectral radiance (*NESR*, in $\text{nW}/\text{cm}^2\text{sr cm}^{-1}$ units) for a single scan at the specified spectral resolution (cm^{-1}). A single scan is defined as a full mirror cycle, consisting of a merged forward and reverse scan.

The procedure utilized for measurement of the noise performance involved collecting a sequence of 100 spectral scans of a one inch cavity blackbody with the FTS, calibrating the entire sequence using a single set of calibration measurements, and computing the standard deviation of the measurements in time. To use the cavity blackbody as a reference, the measurements were made with the Cassegrain telescope removed. Therefore, the *NESR* measurements were corrected for the 90% telescope transmission. Measurements were made both prior to and after the exchange of the InSb detector (discussed later), which occurred on 6-30-93.

Figure 4-1 illustrates the measured *NESR* for a 25C blackbody as a function of wavelength for several resolution settings, indicating a slight decrease with coarser resolution. In light of this result as well as the modest spectral resolution requirements, 8 cm^{-1} was chosen as the best trade of performance and data acquisition time.

Figure 4-2 illustrates the measured *NESR* as a function of wavelength with 8 cm^{-1} resolution at three blackbody temperatures. In the MWIR, the *NESR* increases slightly with temperature as expected. In the LWIR, however, the opposite occurs, which is non-intuitive. This is most likely an anomaly of the fact that the noise data taken on 5-18-93 was uncalibrated due to a malfunction in the calibration sources.

NESR (nW/cm²/sr \cdot cm⁻¹)

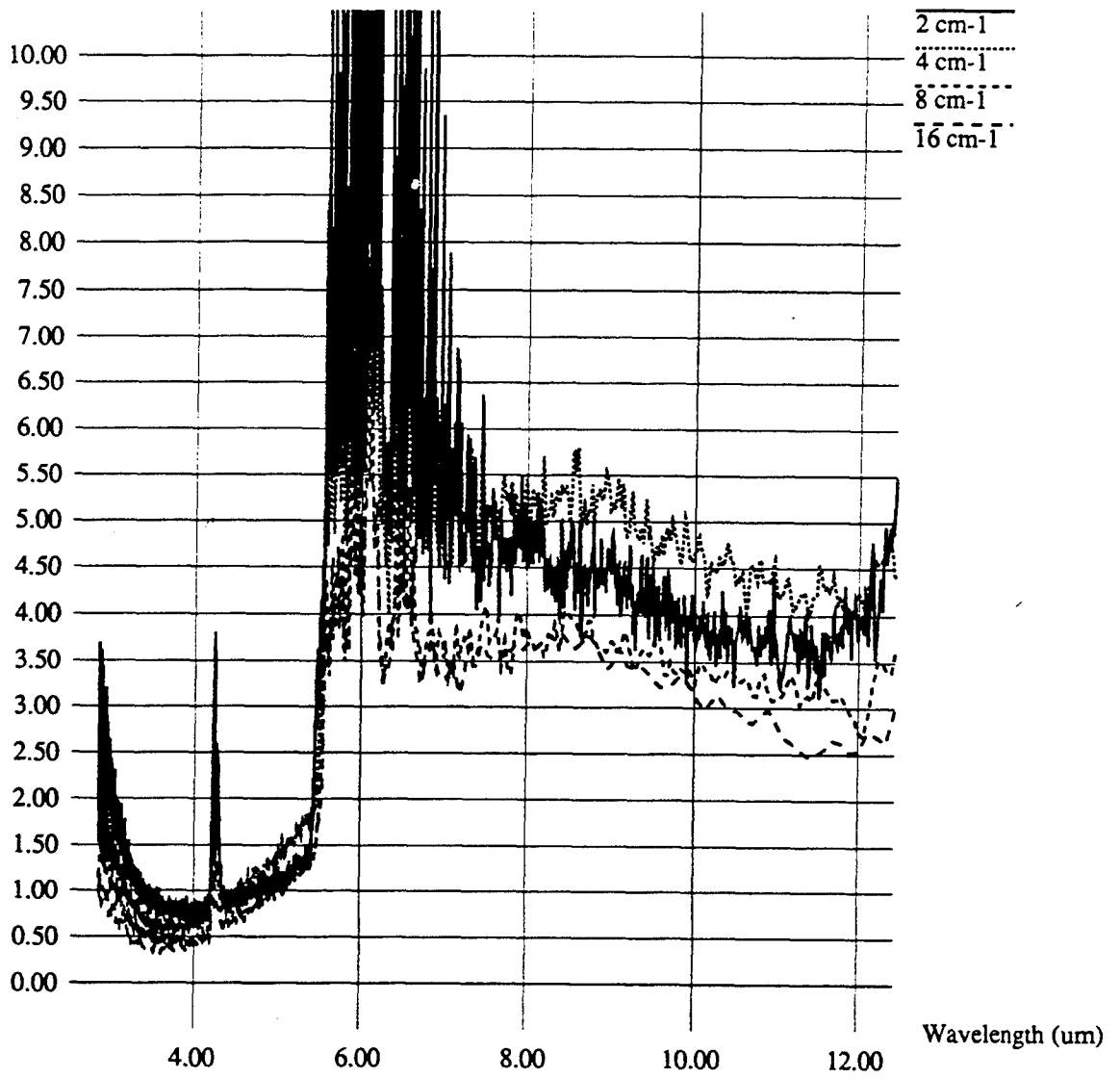


Figure 4-1. Noise Dependence on Spectral Bandwidth (5-18-93).

NESR (nW/cm²/sr \cdot cm⁻¹)

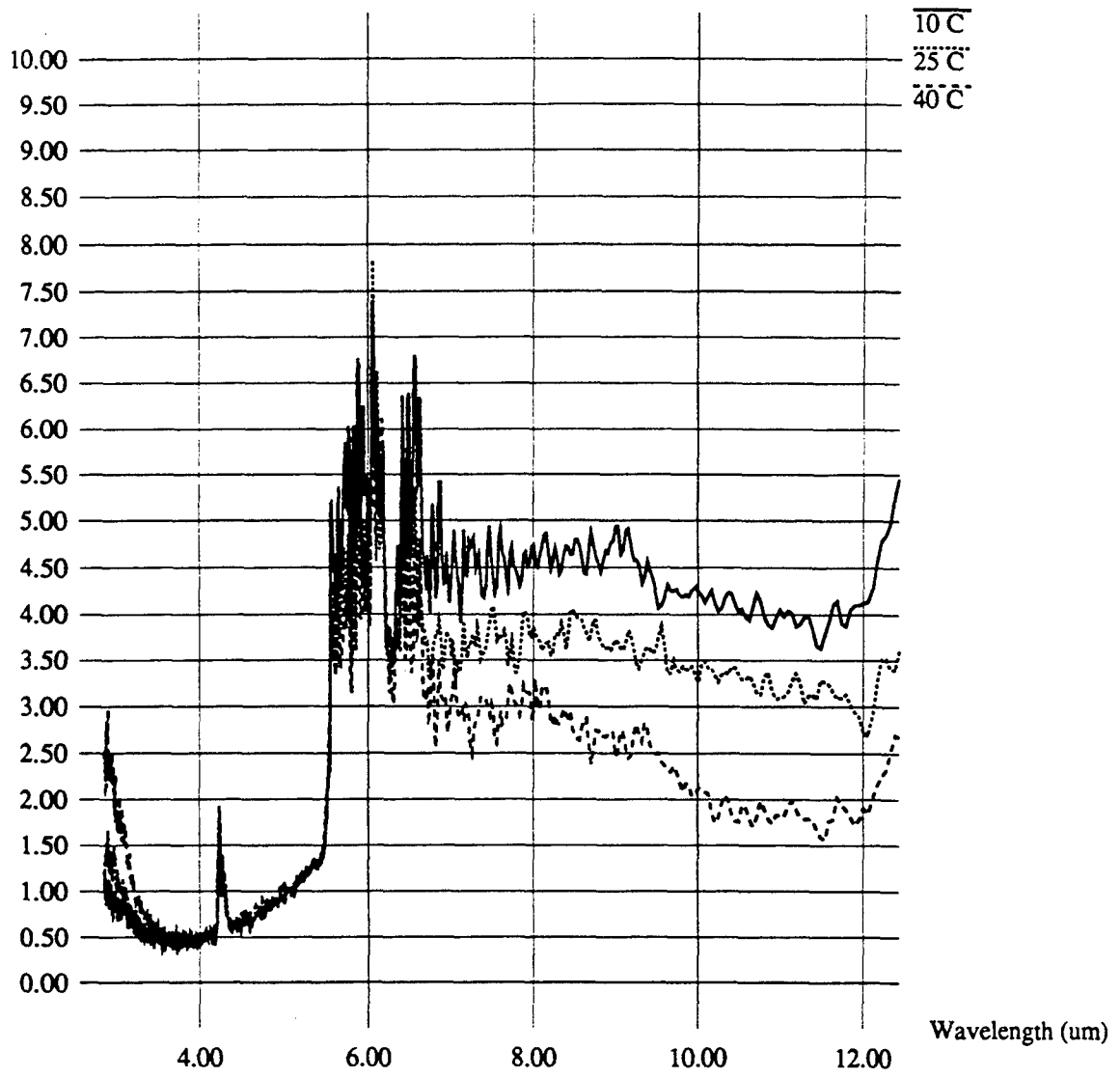


Figure 4-2. Noise Dependence on Temperature (5-18-93).

Figures 4-3 and 4-4 show the spectral correlation of the 8 cm^{-1} , 25C noise data with 4.7 and 10 microns. The interpretation of Figures 4-3 and 4-4 (noise correlation) is as follows. If we truly measured only the noise, we would expect to find the correlation to be zero (or nearly so) except for a small region around the wavelength against which the correlation is computed (reference wavelength). For wavelength binning to provide a \sqrt{N} increase in SNR, the width of this correlation peak must be on the order of 8 cm^{-1} (the spectral resolution interval). Since the FTS oversamples the spectrum by a factor of two, this corresponds to two samples. In actuality, we are not able to solely measure the noise, rather the noise plus some small signal due to FTS and/or blackbody drift. The latter exhibits some spectral correlation, which accounts for the fact that the correlation between widely separated wavelengths is not zero. There is, nevertheless, a recognizable correlation peak in each plot at the reference wavelength. Furthermore, the width of this peak is less than two samples in each case. Therefore, we infer that the noise is spectrally uncorrelated outside the spectral resolution interval.

These results indicate independence of the noise process between spectral channels separated by more than the spectral resolution (the FTS oversamples by a factor of two). This is important since it allows a reduction in the noise level with spectral smoothing. Note that the residual correlation outside the spectral resolution width is likely due to a small drift in the FTS response or blackbody temperature over the time frame of the measurements. Note also that the collected data also indicates temporal decorrelation of the noise from scan to scan, although no such plots are provided here.

The best estimates of the FTS noise level and Bomem specifications are shown in Figure 4-5. These measurements were made from calibrated data after the InSb detector was installed on 6-30-93. Also, the MCT noise performance was measured all the way down to 3 microns (although it becomes very poor below 4 microns). In all regions of the spectrum, the measured NESR was better than the initial estimates from Bomem, typically by more than a factor of two. The increase of the NESR with wavelength in the LWIR region is probably due to detector $1/f$ noise where the interferometric modulation frequencies are lower.

Correlation

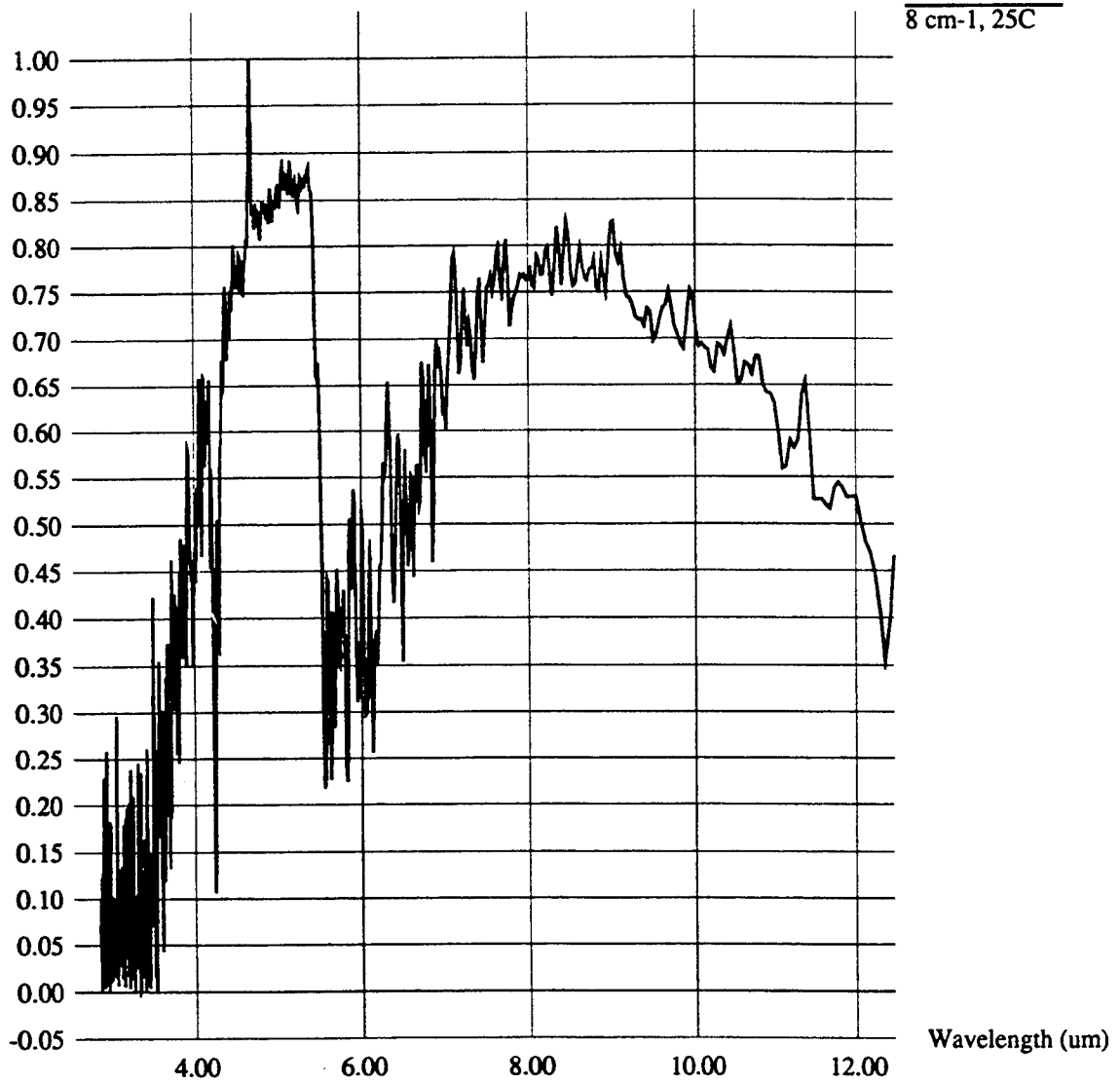


Figure 4-3. Noise Correlation With 4.7 microns (5-18-93)

Correlation

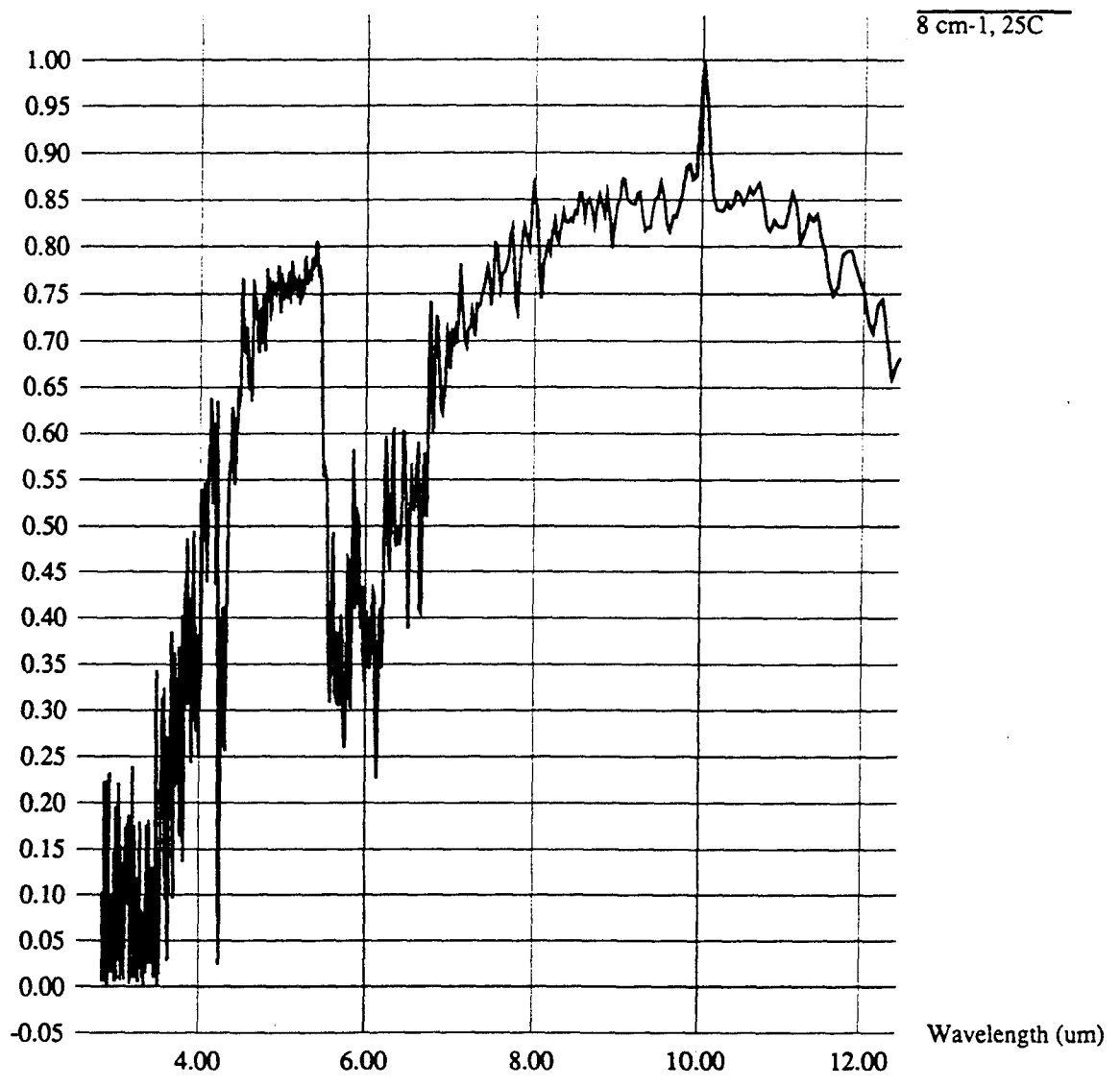


Figure 4-4. Noise Correlation With 10 microns (5-18-93)

NESR (nW/cm²srcm⁻¹)

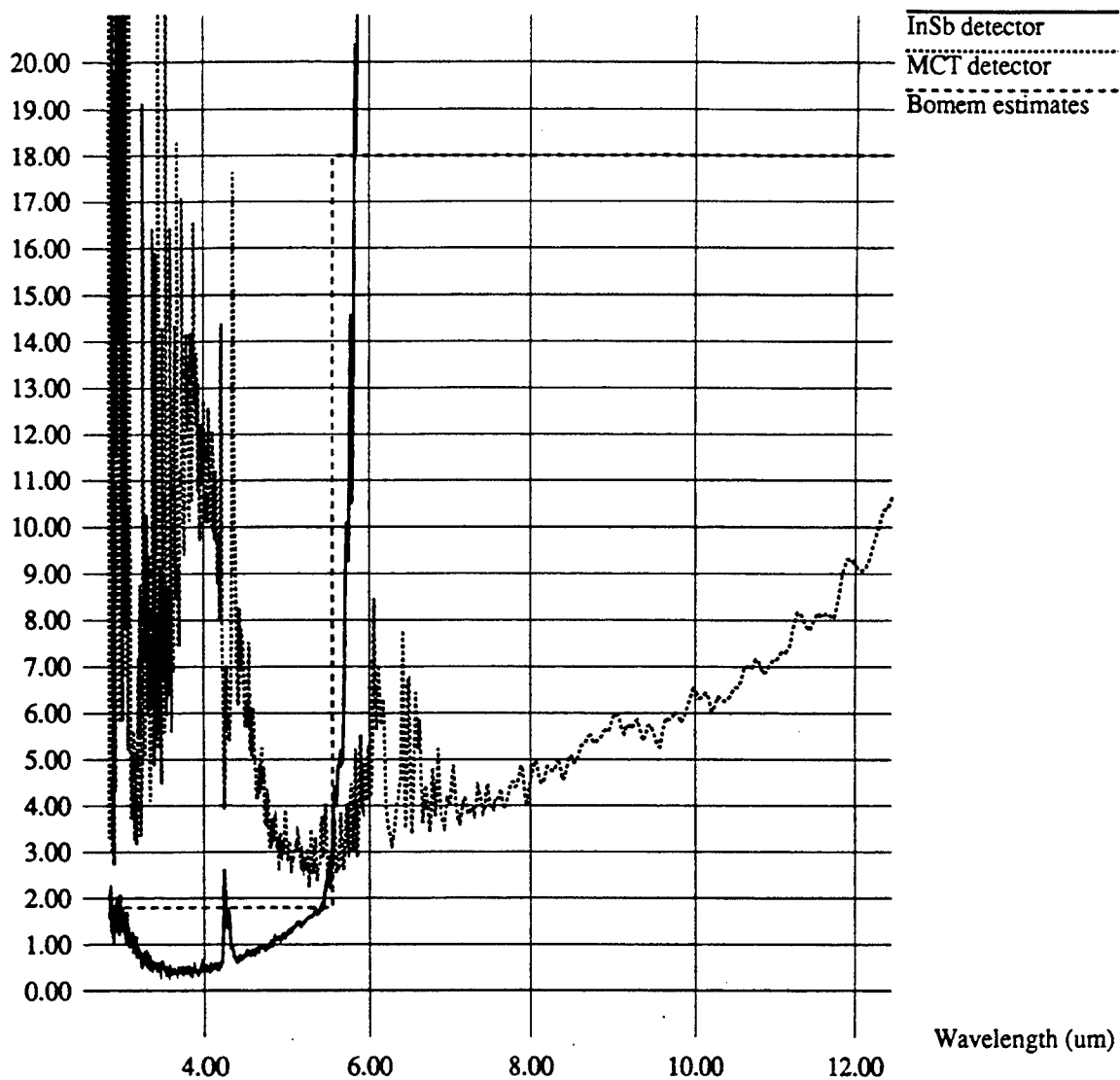


Figure 4-5. Noise at 8 cm⁻¹ (8-31-93).

The following conclusions can be drawn from the noise measurements:

1. The FTS noise performance is better than anticipated.
2. A spectral resolution of 8 cm^{-1} provides the best trade between noise performance and collection time.
3. The noise process is uncorrelated from scan to scan.
4. The noise is uncorrelated outside the spectral resolution interval.

Table 4-2 summarizes the measured NESR at several wavelengths. No sensor modifications were made to explicitly improve noise performance.

Table 4-2: Noise Performance Summary

Wavelength (μm)	NESR ($\text{nW}/\text{cm}^2\text{srcm}^{-1}$)	
	InSb detector	MCT detector
3.8	0.49	7.5
4.7	0.89	3.7
8.0	-	4.6
10.0	-	6.4
12.0	-	9.1

4.2 ABSOLUTE CALIBRATION ACCURACY

Although absolute calibration accuracy is not of critical importance in the ability of the sensor system to collect high quality contrast and correlation data, it may be important in future use of the collected data. Absolute radiometric calibration relies on the use of the two extended area blackbody calibration sources at known temperatures to estimate the complex sensor gain and offset response. Such a calibration is performed on an experiment-by-experiment basis, using the method of Revercomb [4.1].

The accuracy of calibration in an absolute sense is determined by the radiometric accuracy of blackbody calibration sources, which in turn can be characterized by their emissivity and temperature accuracy. The objectives of the characterization experiments summarized in this section were (1) to measure the radiometric accuracy of the

blackbody calibration sources and (2) to predict the resulting absolute calibration accuracy based on these measurements, using the two-point calibration method. Specifications for the EOI T1812D sources include a temperature accuracy of 0.03C and emissivity of 0.99 ± 0.01 .

In order to measure the radiometric accuracy of the blackbodies, a radiance standard is required. For purpose of this characterization, a MIKRON cavity blackbody was used as the standard. FTS measurements of both the EOI extended area blackbody and the cavity blackbody were made at 20C, 25C, and 45C setpoints with sufficient time between setpoints to allow adequate settling but minimal time difference between the EOI and cavity measurements at any setpoint. All the data was calibrated using the cavity measurements at the 20C and 45C settings. Note that only one EOI blackbody was actually measured under the assumption that the other source would perform similarly.

Figure 4-6 illustrates the apparent emissivity of the EOI blackbody, which is simply the ratio of the calibrated EOI blackbody and cavity measurements at each setpoint. The interpretation of this result is as follows. At the 25C setpoint, the apparent emissivity is very nearly unity. In this case, a nonunity emissivity of the EOI blackbody will not produce an appreciable error since the reflected radiation originates from sources at nearly the same temperature. The fact that this curve is so close to unity and flat tells us that the temperature accuracy is extremely good. At the 45C setpoint, the reflected radiation originates from cooler sources such that the apparent emissivity is less than unity. This gives us an upper bound on the source emissivity (< 0.99), which means that the manufacturer's specification is suspect. To measure the true emissivity, the reflected environment would have to be made very cold or the source temperature would have to be increased (which is not possible). At the 20C setpoint, the apparent emissivity is greater than unity since reflected radiation originates from warmer sources.

Apparent Emissivity

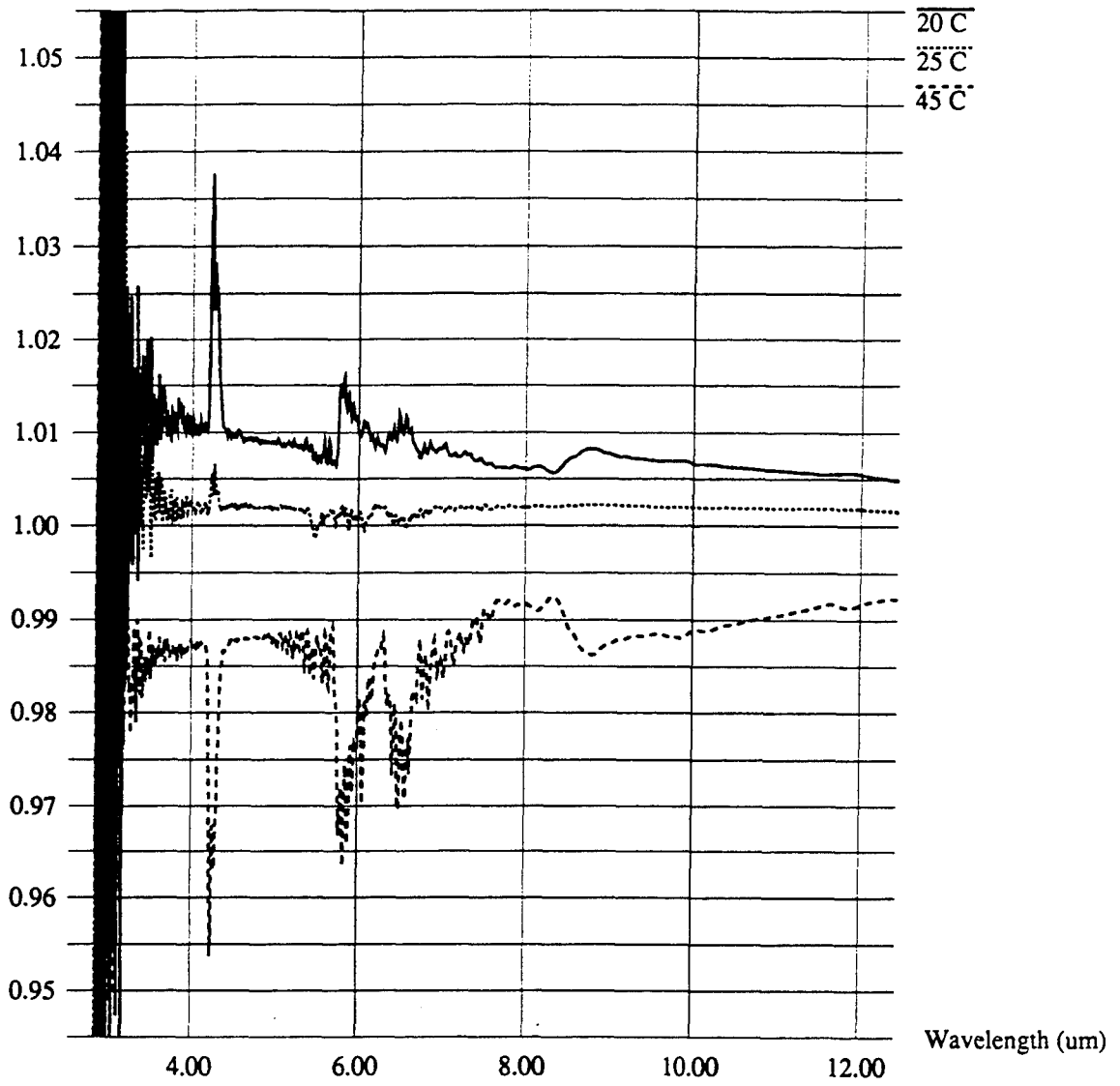


Figure 4-6. Blackbody Apparent Emissivity (8-31-93).

Another way to describe this result is in the form of an absolute radiometric accuracy, given by

$$\frac{dL}{L} = \frac{L_{\text{blackbody}} - L_{\text{reference}}}{L_{\text{blackbody}}} \quad (4-1)$$

This is shown in Figure 4-7 and displays the same behavior as described above. Assuming calibration is performed using the EOI 20C and 45C setpoints, the absolute calibration accuracy of the entire sensor system can be shown to be (see Section 5).

$$\frac{dL_T}{L_t} = \left[1 + \frac{dL_H - dL_C}{L_H - L_C} \right] + \left[\frac{L_H dL_C - L_C dL_H}{L_H - L_C} \right] \frac{1}{L_T} \quad (4-2)$$

where L_H , L_C , L_T are the hot source, cold source, and target radiances and dL_H , dL_C , dL_T are the errors associated with each. All are implicitly functions of wavelength. Figure 4-8 shows this result, which falls well below our expectation of 3-5% (see Section 5).

The conclusions with regard to the absolute calibration accuracy of the FTS sensor system are:

- 1) The absolute calibration accuracy is dictated by the radiometric accuracy of the calibration sources
- 2) The radiometric accuracy of the calibration sources appears to be limited by their emissivity, which is lower than the 0.99 manufacturer's specification.
- 3) The absolute radiometric accuracy of the sensor system is roughly within 1%, which is better than expected.

No system modifications were made to explicitly improve absolute calibration accuracy.

4.3 RELATIVE CALIBRATION ACCURACY

By relative calibration accuracy, we refer to the situation in which spectroradiometric measurements are made using a different set of hot and cold calibration source measurements and are compared in some manner. It is assumed that

Pct. Miscalibration

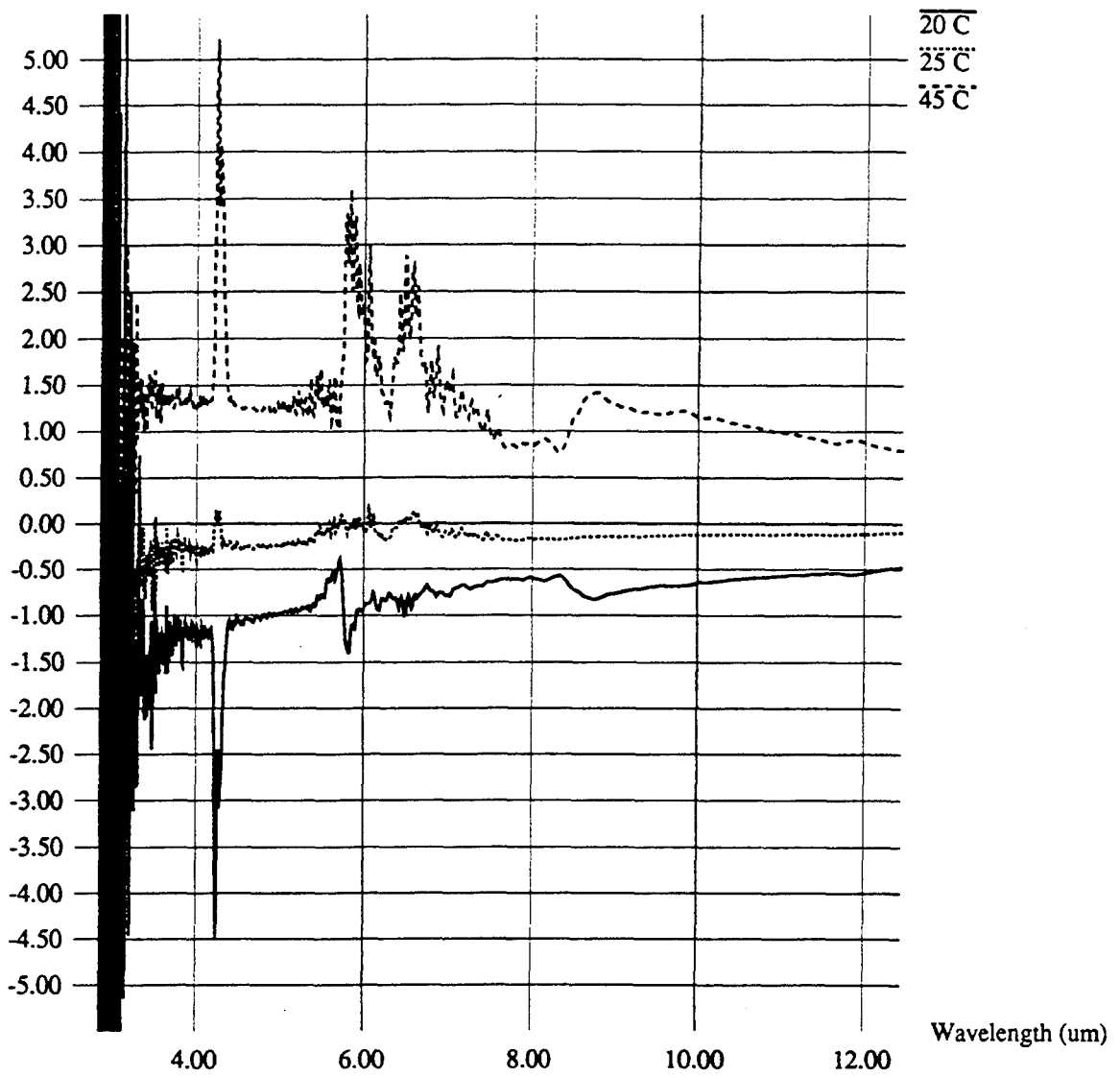


Figure 4-7. Blackbody Radiometric Accuracy (8-31-93).

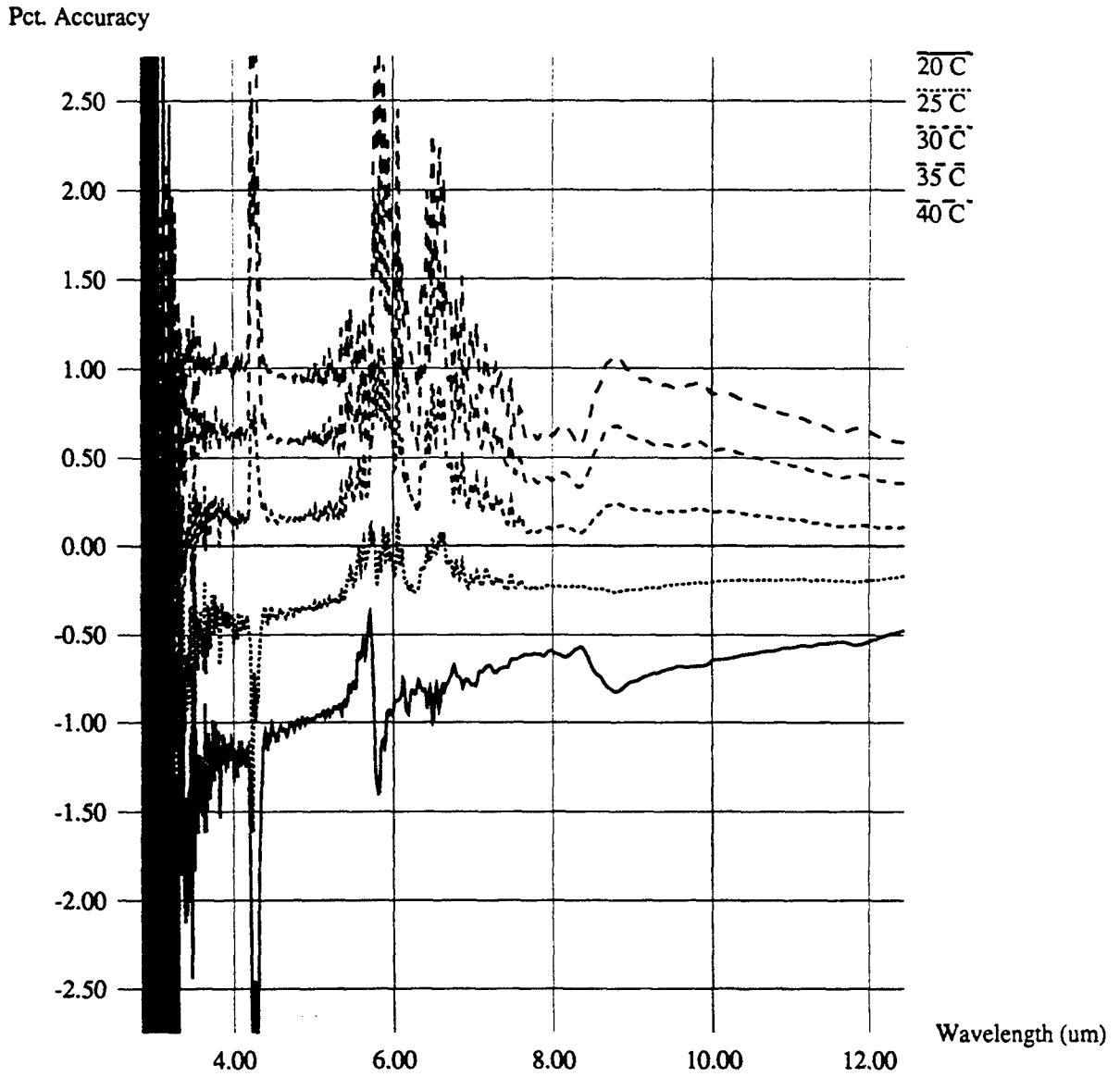


Figure 4-8. Absolute Calibration Accuracy.

the same sources and same calibration procedure are utilized, as well as that the ambient environment is similar. Relative calibration accuracy, for example, is an operative parameter in comparative studies of data collected in different experiments. Within an experiment, however, this parameter does not apply since a single set of calibration source measurements are used.

Relative calibration accuracy is determined by the stability of the blackbody calibration sources. To maximize their stability, the sources were operated in a steady state mode such that their setpoints were not altered during the course of each day of collection. The objectives of the characterization experiments described in this section were (1) to measure blackbody stability in a collection environment over the time frame of a typical experiment and (2) to predict the resulting relative calibration accuracy based on these measurements using the two-point calibration method. The stability specification of the EOI T1812D blackbody calibration is ± 0.003 degrees, although our anticipation was more on the order of 0.03 degrees due to the field environment.

The difficulty in measuring blackbody stability is in separating it from the instability of the measurement instrument used, which in our case was the FTS itself. To circumvent this problem, we utilized a differential mode in which a set of alternating measurements were made of two blackbodies at slightly different temperatures (specifically, 24C and 26C). Under the assumption that the instability of the blackbodies will be uncorrelated between each other, their instability was estimated from the instability of the differential between adjacent measurements. This was performed using a typical set of experiment parameters (30 measurements, 25 coadded scans per measurement, 20-30 min total measurement time) on several days throughout the WPAFB and MICOM data collections.

Figures 4-9 through 4-16 illustrate the results of the blackbody instability tests in the form of the estimated rms temperature fluctuation as a function of wavelength. Since radiometric instability can arise from fluctuations in either the physical blackbody temperature or the reflected radiance component, the rms temperature fluctuation would not necessarily be expected to be spectrally constant. Note that the large increase below 4 microns is due to the ultimate noise limit of the FTS itself. This limit is on the order

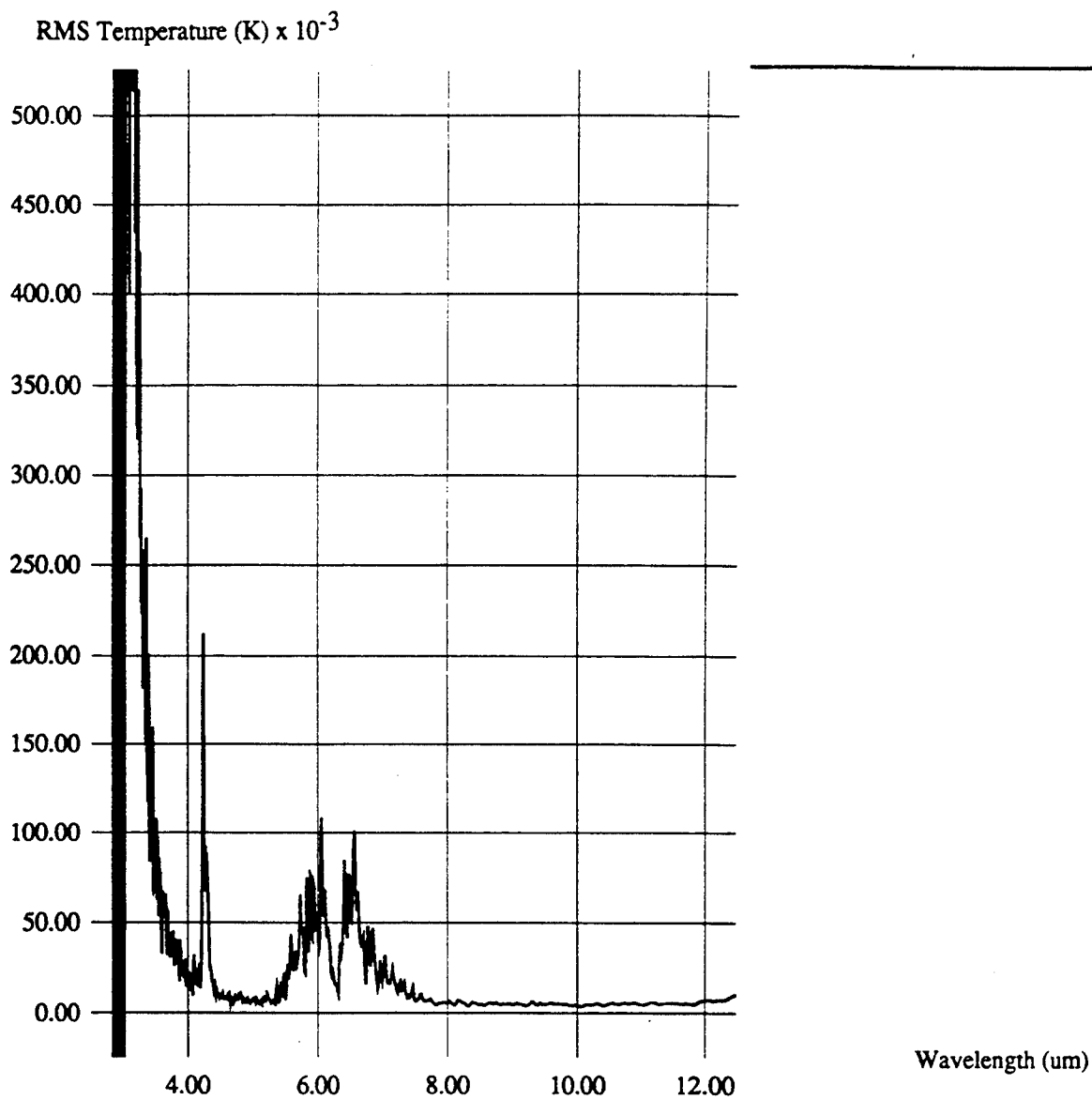


Figure 4-9. Blackbody Stability on 7-7-93 (#1).

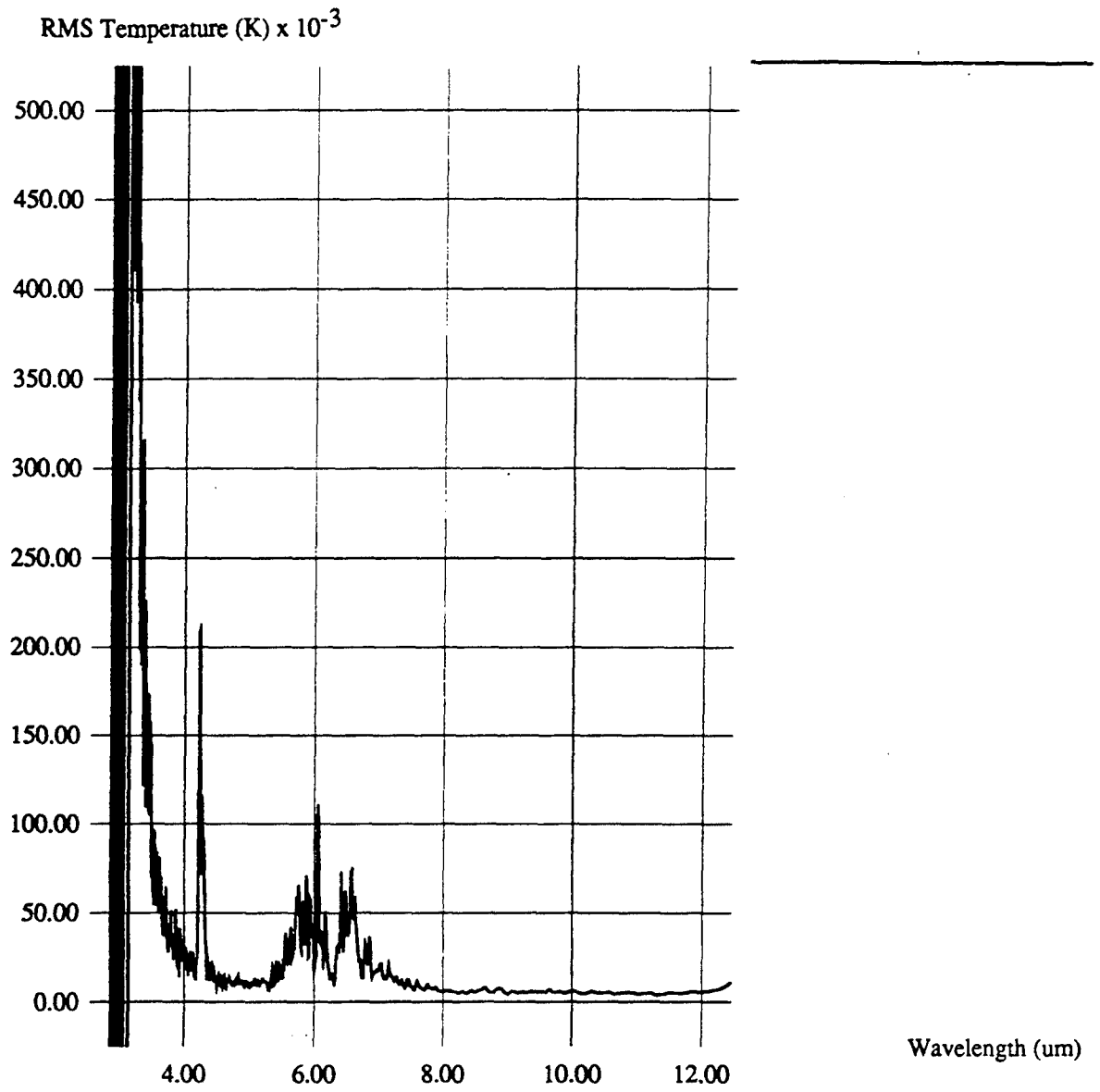


Figure 4-10. Blackbody Stability on 7-7-93 (#2).

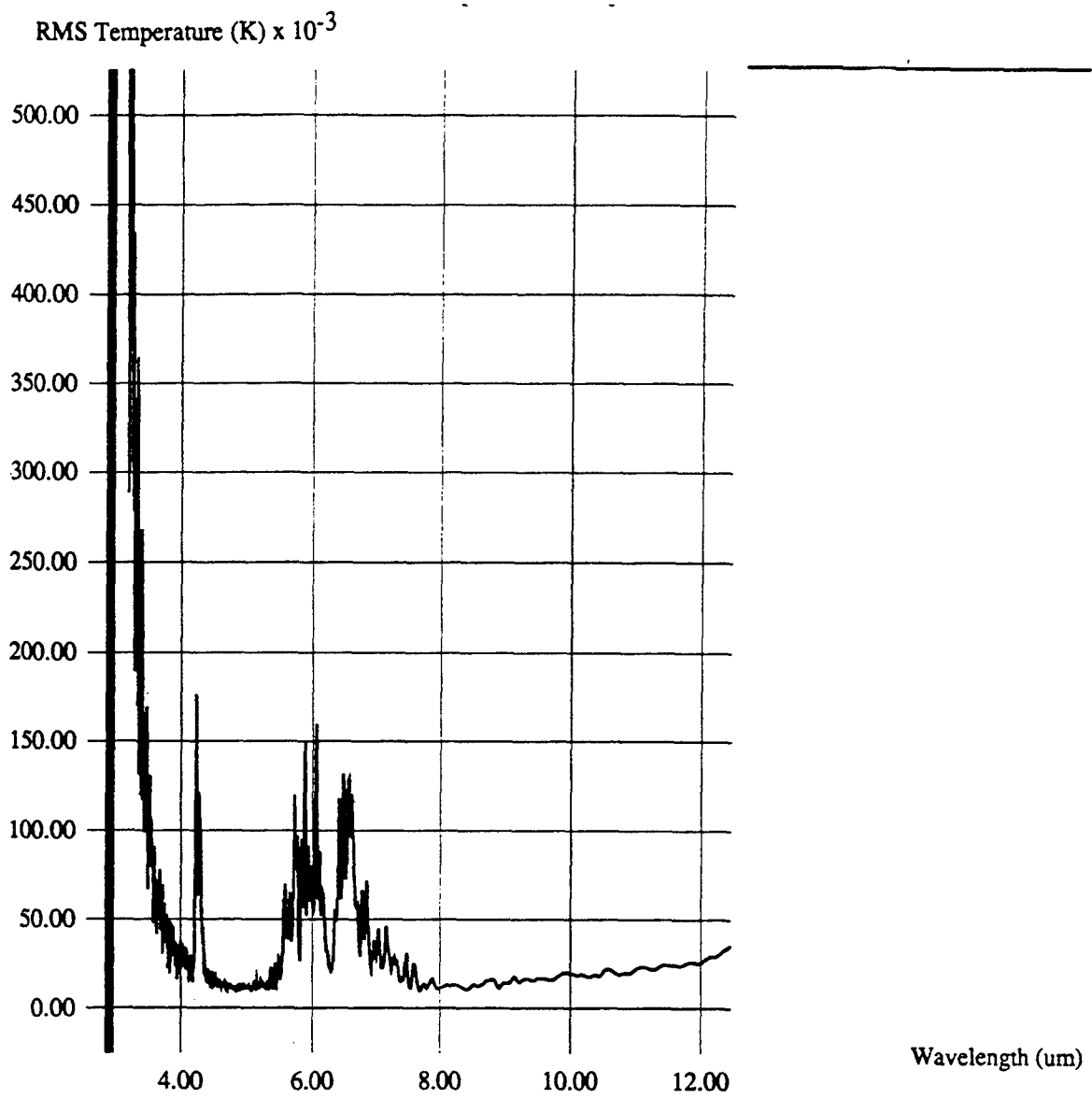


Figure 4-11. Blackbody Stability on 7-16-93.

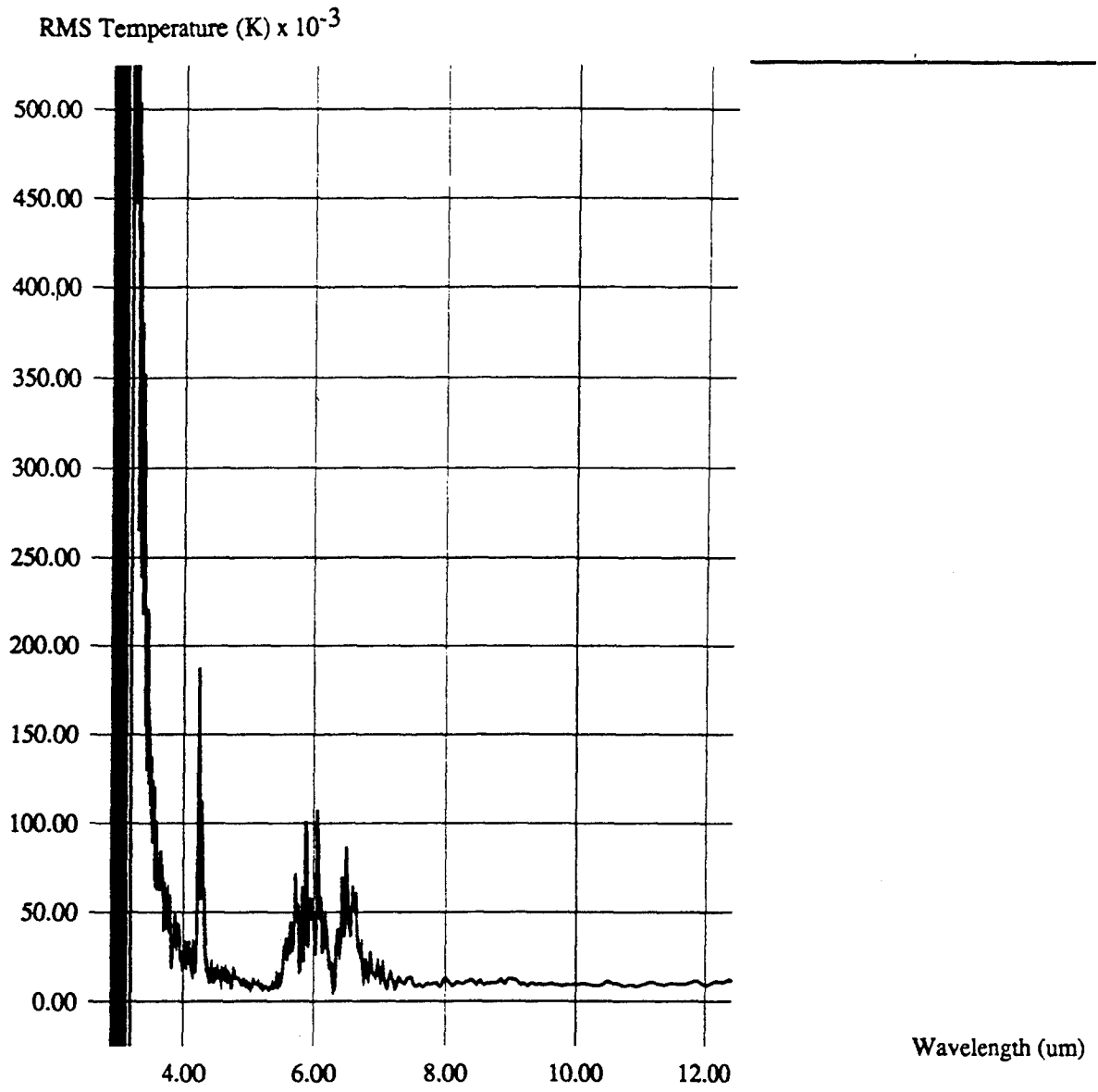


Figure 4-12. Blackbody Stability on 7-17-93.

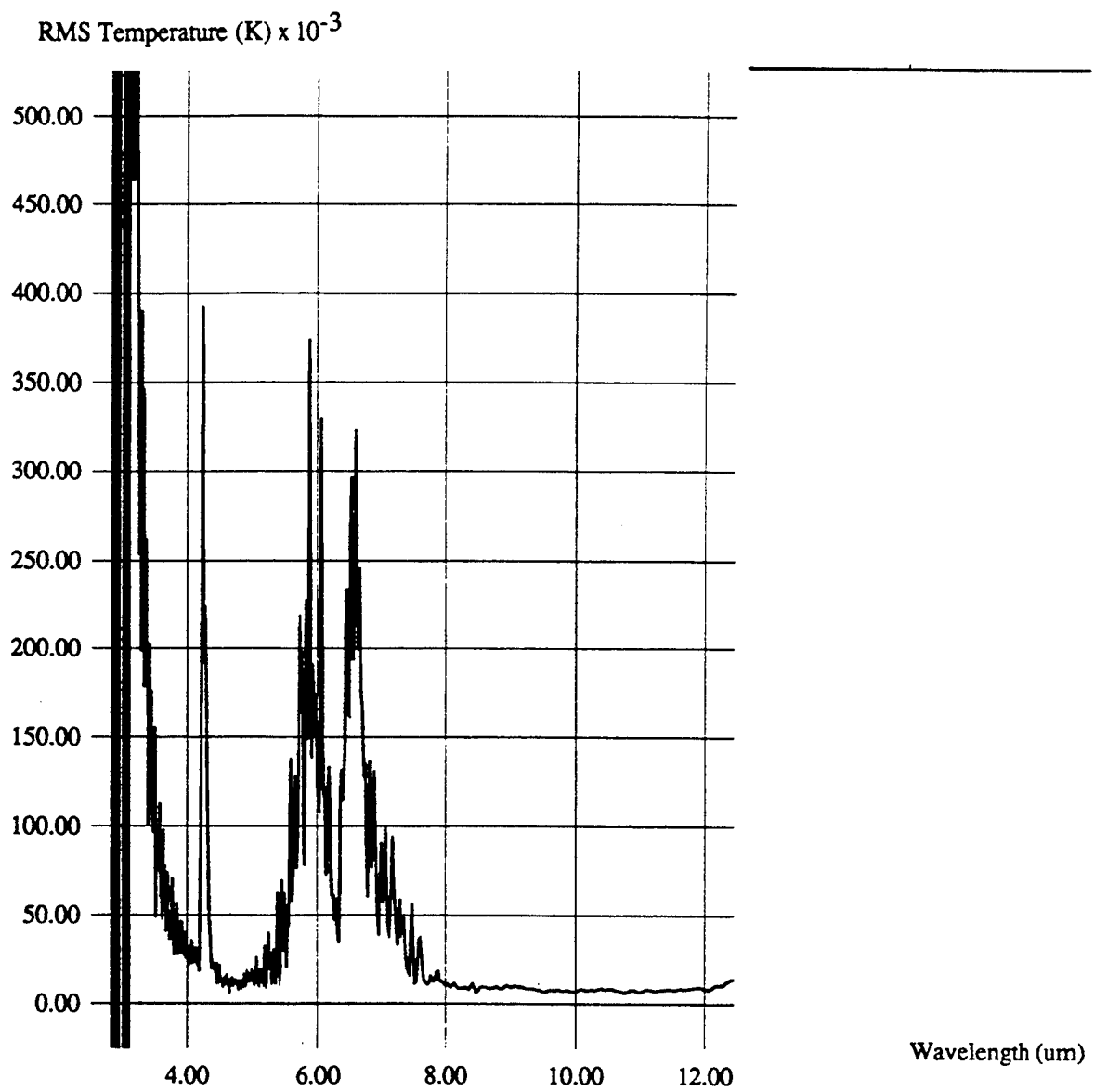


Figure 4-13. Blackbody Stability on 7-19-93.

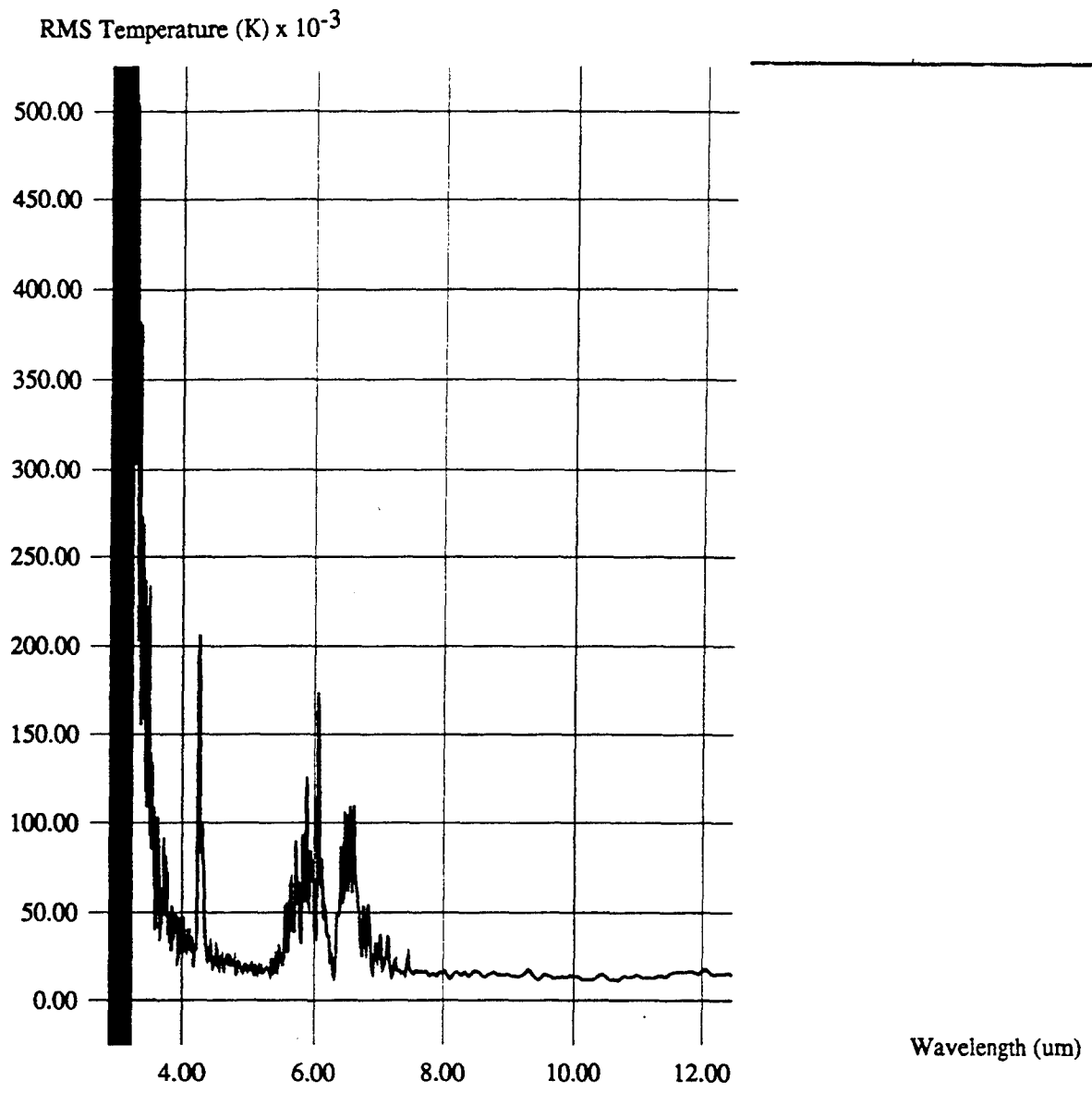


Figure 4-14. Blackbody Stability on 7-20-93.

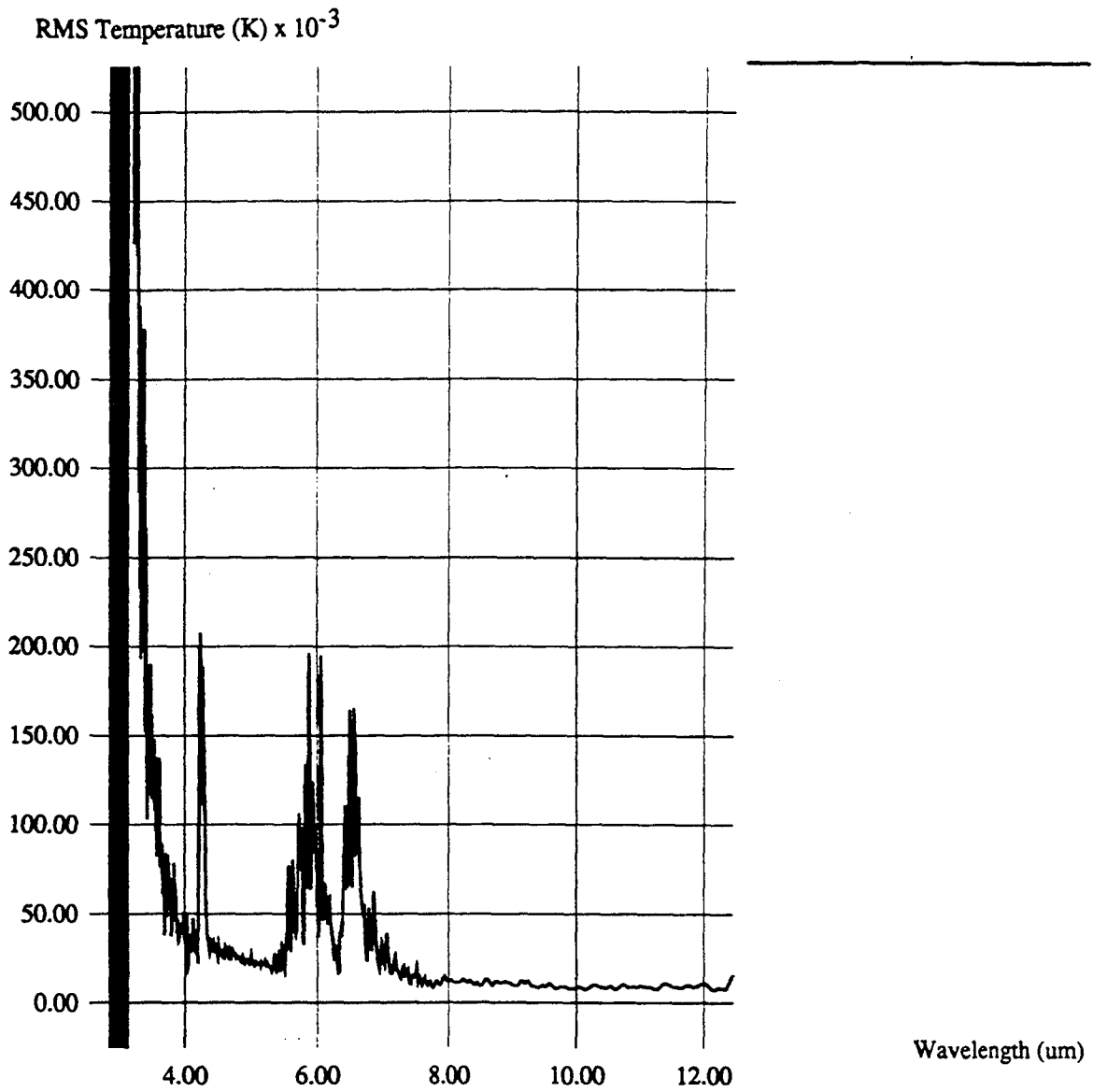


Figure 4-15. Blackbody Stability on 7-21-93.

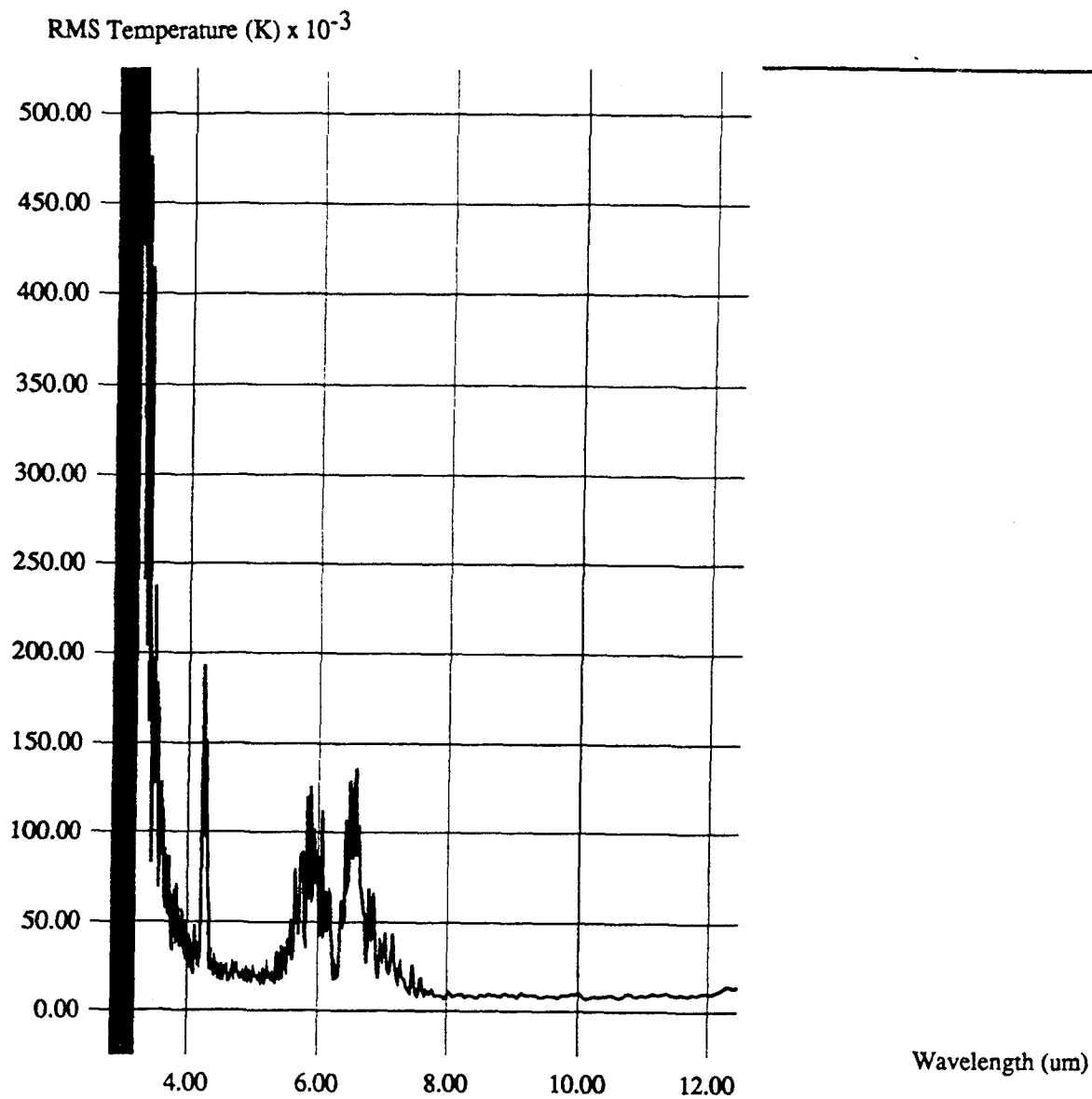


Figure 4-16. Blackbody Stability on 7-22-93.

of 10 mK at 4.7 microns and 7.5 mK at 10 microns. The average of the illustrated results (Figure 4-17) indicates a measured blackbody instability of 15 mK at 4.7 microns and 10 mK at 10 microns, which is just above this measurement limit. These results are better than anticipated.

Assuming the instability is similar at the 20C and 45C setpoints where calibration measurements are made, the relative calibration accuracy of the entire system can be shown to be (see Section 5):

$$\begin{aligned} \frac{dL_T}{L_T} = & \frac{1}{\sqrt{2}} \frac{1}{L_H - L_C} \left[\frac{hc}{\lambda KT^2_H} L_H + \frac{hc}{\lambda KT^2_C} L_C \right] \sigma_{CAL} \\ & + \frac{1}{\sqrt{2}} \frac{L_H L_C}{L_H - L_C} \left[\frac{hc}{\lambda KT^2_H} + \frac{hc}{\lambda KT^2_C} \right] \frac{\sigma_{CAL}}{L_T} \end{aligned} \quad (4-3)$$

where T_C and T_H are the cold and hot temperature setpoints and σ_{CAL} is the blackbody temperature instability. The instability and radiance parameters are explicitly spectrally dependent. Figure 4-18 shows this result for 20C, 30C, and 40C blackbody targets, which falls within our expectation of 0.3% (see Section 5).

The conclusions with regard to the relative calibration accuracy of the FTS sensor system are:

- 1) The relative calibration accuracy is dictated by the stability of the blackbody sources.
- 2) The measured blackbody instability is in the 10-15 mK range, which is near the noise limit of the FTS.
- 3) The relative calibration accuracy of the sensor system is better than 0.25% in the MWIR and 0.15% on the LWIR.

No system modifications were made to explicitly improve relative calibration accuracy.

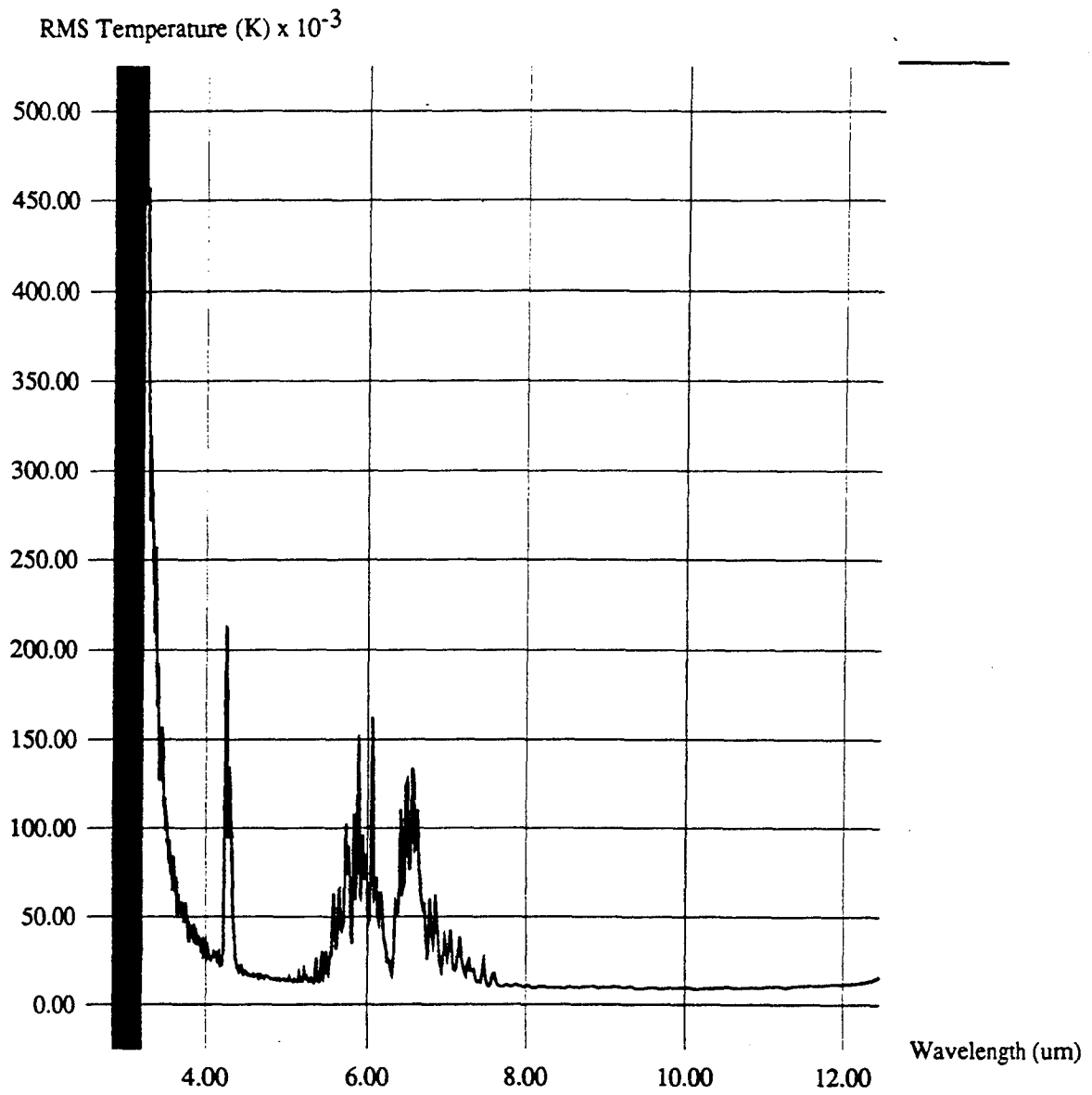


Figure 4-17. Average Blackbody Stability.

Pct. Accuracy

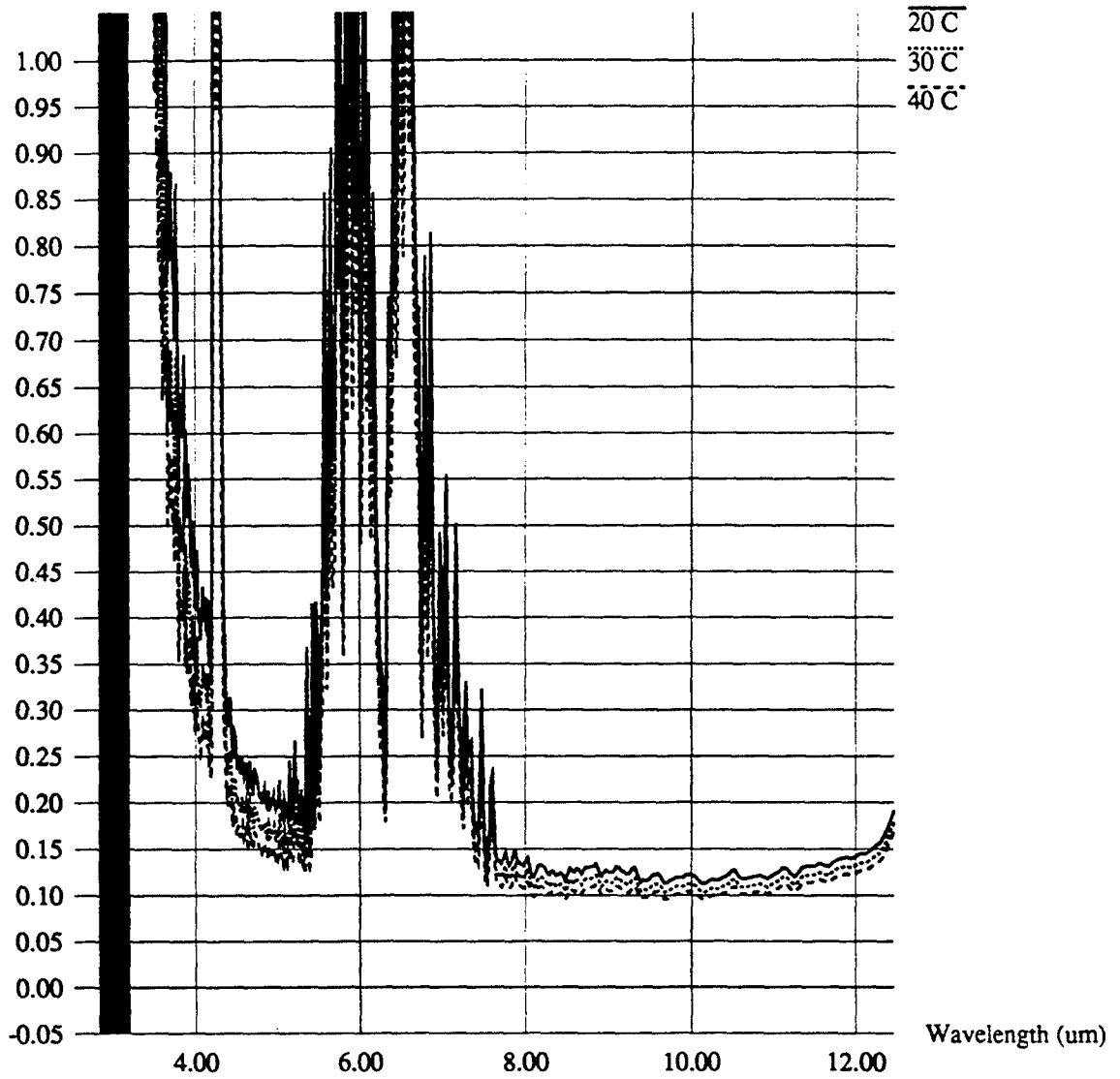


Figure 4-18. Relative Calibration Accuracy.

4.4 TEMPORAL RADIOMETRIC STABILITY

Within a calibration cycle, the relative accuracy of spectroradiometric measurements will be limited by the stability of the FTS response. The major sources of instability are stray radiances either external or internal to the interferometer, detector instability due to bias fluctuations or detector cooling variances, and electronic instability in the preamp to A/D chain. The former will most likely be strongly correlated between detector modules, while the latter two will be uncorrelated.

Early in the WPAFB data collection campaign, FTS instability was recognized to be a problem, primarily due to large instabilities in the InSb detector, which was configured in a reentrant dewar. Apparently, the dewar was not providing a stable thermal environment for the detector, which induced fluctuations in its response. Several theories exist with regard to the specific cause, including insufficient dewar vacuum, defective pressure control valves, and/or design limitations. The chosen solution was to replace the detector with a similar InSb detector mounted in a standard dewar. This approach provided a significant increase in MWIR stability.

The Cassegrain telescope is potentially another source of instability. Because of its 10% obscuration, stray radiances emanating from the front field aperture wheel are measured by the instrument. Since these radiances are not controlled, they can introduce variances in the measured signal, although the instability will likely be correlated band to band, including between detector modules. To minimize this effect, however, the collimator assembly was wrapped with a insulating blanket. This reduced both the thermal instability of the aperture wheel as well as the fluctuations in the reflected radiative environment.

Another problem identified (although fairly small) was a systematic throughput variation with depression angle, presumably due to slight mechanical shifts of the front aperture as a function of sensor orientation. Originally, the sensor was operated with the front aperture matched in size to the two secondary field apertures in each of the detector modules. By operating the sensor in this manner, any shifts in the front aperture will cause a throughput reduction via vignetting. Further, if there is any misalignment in relative positioning of the secondary apertures, this instability could be uncorrelated

between detector modules. To eliminate this effect, the front aperture could be either increased or decreased in size. In the latter case, the signal throughput would be reduced. Also, the residual instability may increase due to stray radiances from the front aperture edges. Note that stray radiances from the secondary apertures are not a problem since they are not modulated by the interferometer. Due to these factors, we chose to make the front aperture slightly larger than the secondary apertures.

After the described modifications were made, a residual FTS instability remained over the nominal 20-30 minute time frame of an experiment. A portion of this instability appears to be thermally driven and correlated between detector modules, but part appears to be in the detector chains themselves and uncorrelated between modules. In most cases, however, the residual instability is slowly varying with a strong linear component. Because of this, we adopted a temporal calibration procedure which involves making hot and cold calibration measurements immediately prior to and after the set of target/background measurements. These measurements are used to estimate the sensor gain and offset drift over the collection time, and each of the intervening target measurements are then adjusted using a temporally linear interpolation of these estimates. The result is a complete removal of the linear gain and offset drift component. The residual instability will be fundamentally limited to $\sqrt{2}$ times the blackbody instability (or 15-20 mK).

The difficulty in measuring FTS stability is the necessity of having a suitably stable radiance standard. Because the telescope plays potentially a significant role in instability, utilizing a cavity blackbody with the telescope removed was judged not satisfactory. Rather, the same method (and, in fact, the same data) used for estimating blackbody instability was used for measuring FTS stability. To measure FTS stability, however, the instability of the mean radiance of adjacent measurements was estimated. This separates out the differential instability that is attributed to the blackbodies, as described in Section 4.3. Once again, this was performed using a typical set of experiment parameters (30 measurements, 25 coadded scans, 20-30 min total duration) on several days throughout the WPAFB and MICOM data collections.

Figures 4-19 to 4-26 illustrate the results of the FTS instability tests in the form of the estimated rms temperature fluctuation as a function of wavelength. Due to the various sources, some of which are not thermally driven, there is no reason to expect the curves to be spectrally constant. The graphs indicate the instability both prior to and after temporal calibration of the data. In most cases, temporal calibration provides a significant reduction in instability. Furthermore, the estimated linear component is typically different between detector modules, implying that its source is apparently in the detector chain.

The average of the individual test sets is shown in Figure 4-27, indicating an average instability of 40-70 mK (0.1 to 0.15%) prior to temporal calibration and 15-20 mK (0.03 to 0.06%) after temporal calibration. This corrected instability is on the order of the fundamental limit due to blackbody instability.

The conclusions with regard to FTS stability are:

- 1) FTS stability was recognized to be a problem.
- 2) Modifications were performed to minimize instability, including the replacement of the InSb detector, the use of a thermal blanket around the collimator, and the use of a larger front aperture size.
- 3) The residual instability is generally dominated by a linear gain and offset drift component, which can be eliminated using a temporal calibration procedure.
- 4) The corrected instability is limited to 15-20 mK by the instability of the blackbody calibration sources, which is near the sensor noise floor.

4.5 RESPONSE LINEARITY

The linearity of the FTS system is important particularly for MSSP correlation measurements since differential nonlinearity between bands can cause decorrelation. Since the blackbody function itself is nonlinear, it provides a fundamental limit to correlation such that it is only necessary that the instrument not further exacerbate the problem. The only possible sources of nonlinearity are the detector response and analog electronics. With a Fourier transform spectrometer, such nonlinearities will manifest

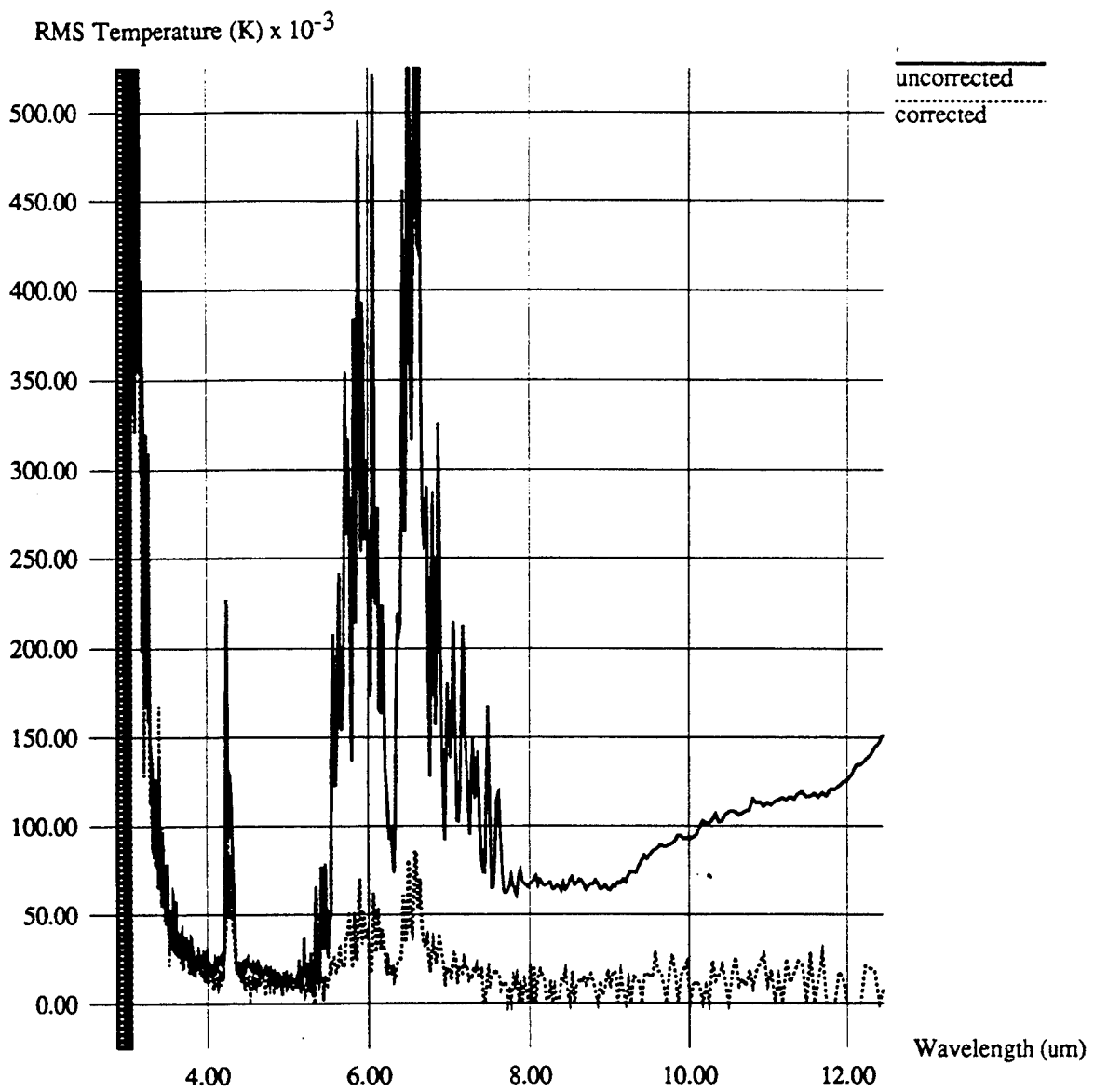


Figure 4-19. FTS Stability on 7-7-93 (#1).

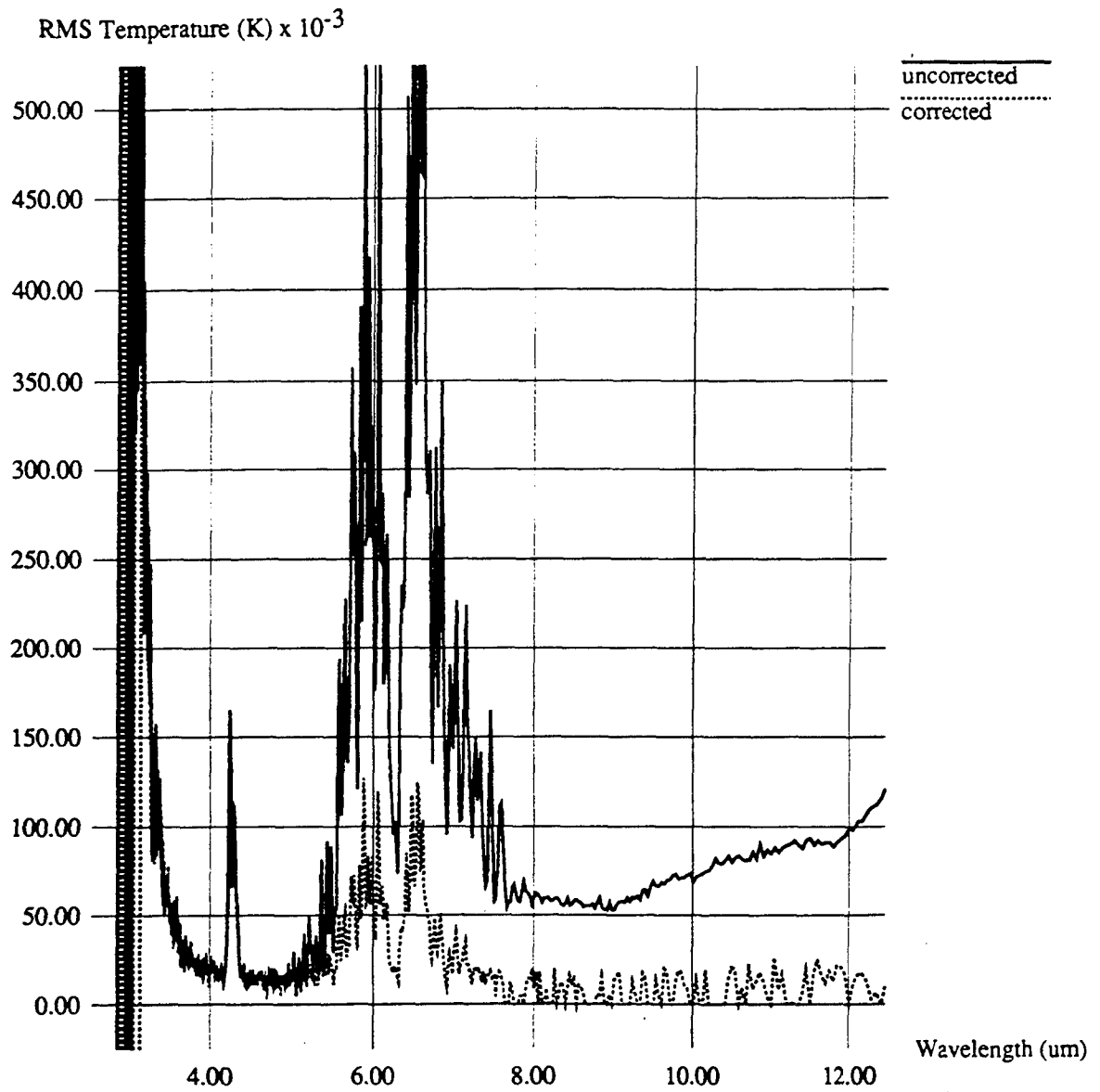


Figure 4-20. FTS Stability on 7-7-93 (#2).

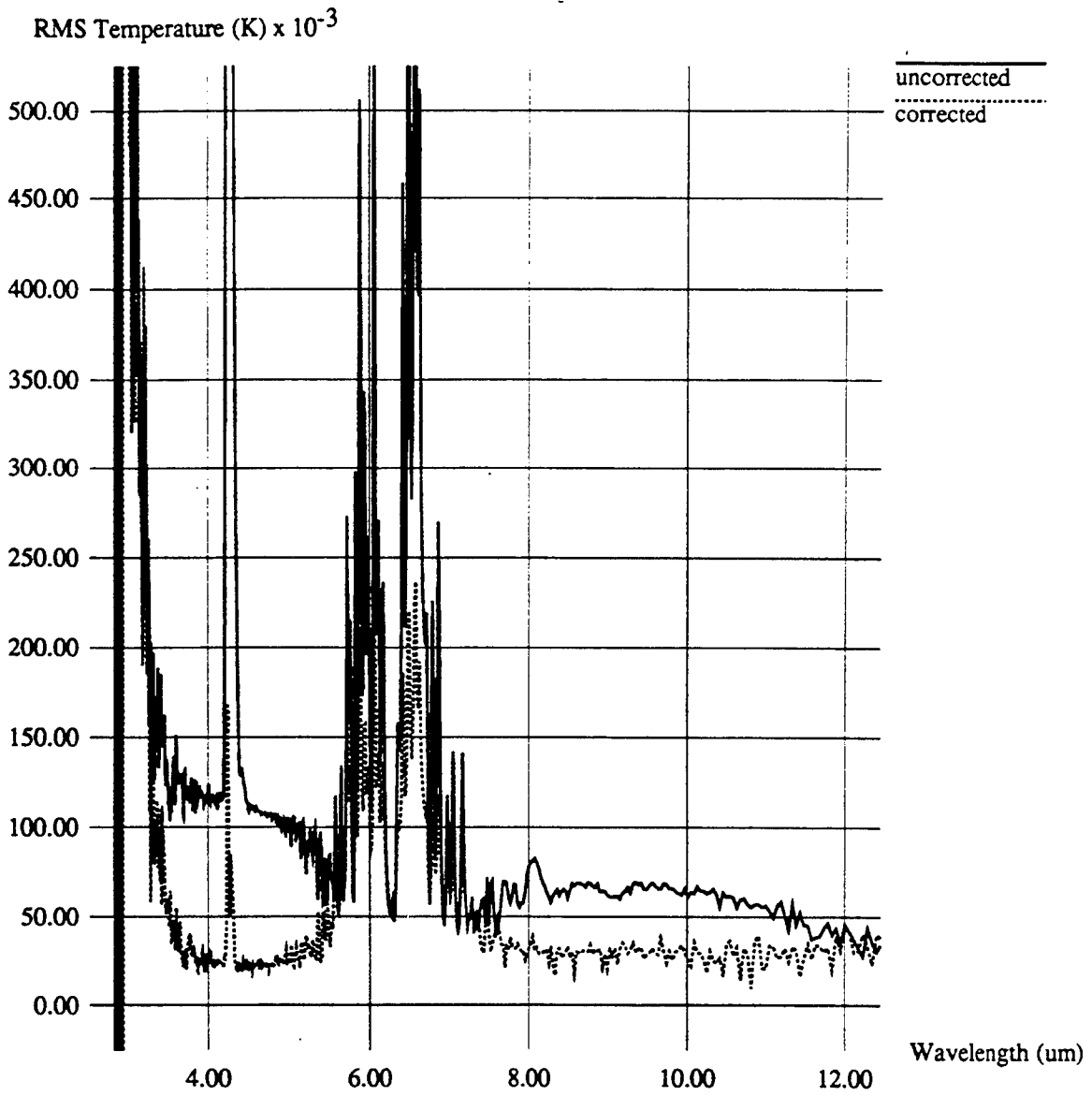


Figure 4-21. FTS Stability on 7-16-93.

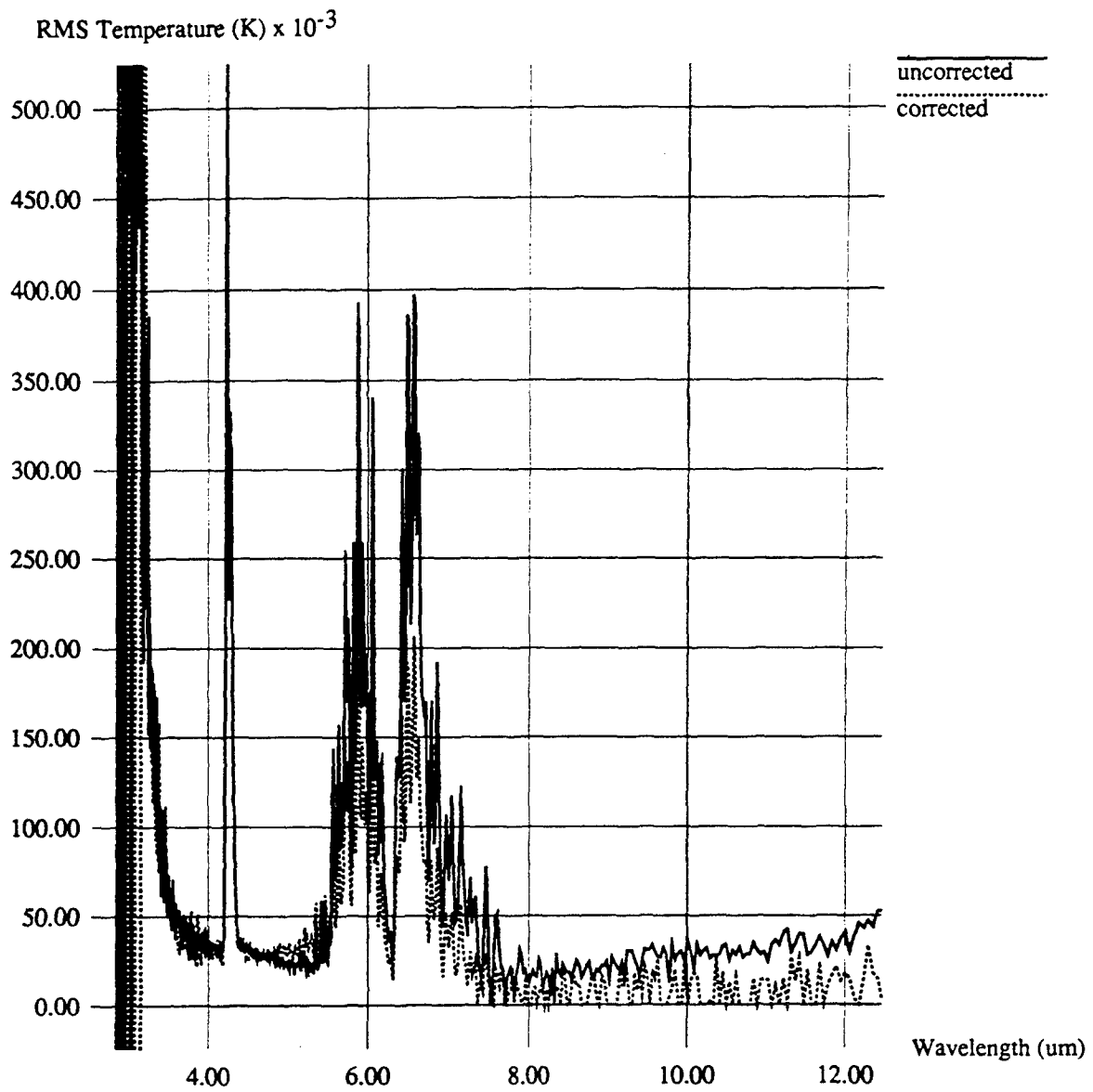


Figure 4-22. FTS Stability on 7-17-93.

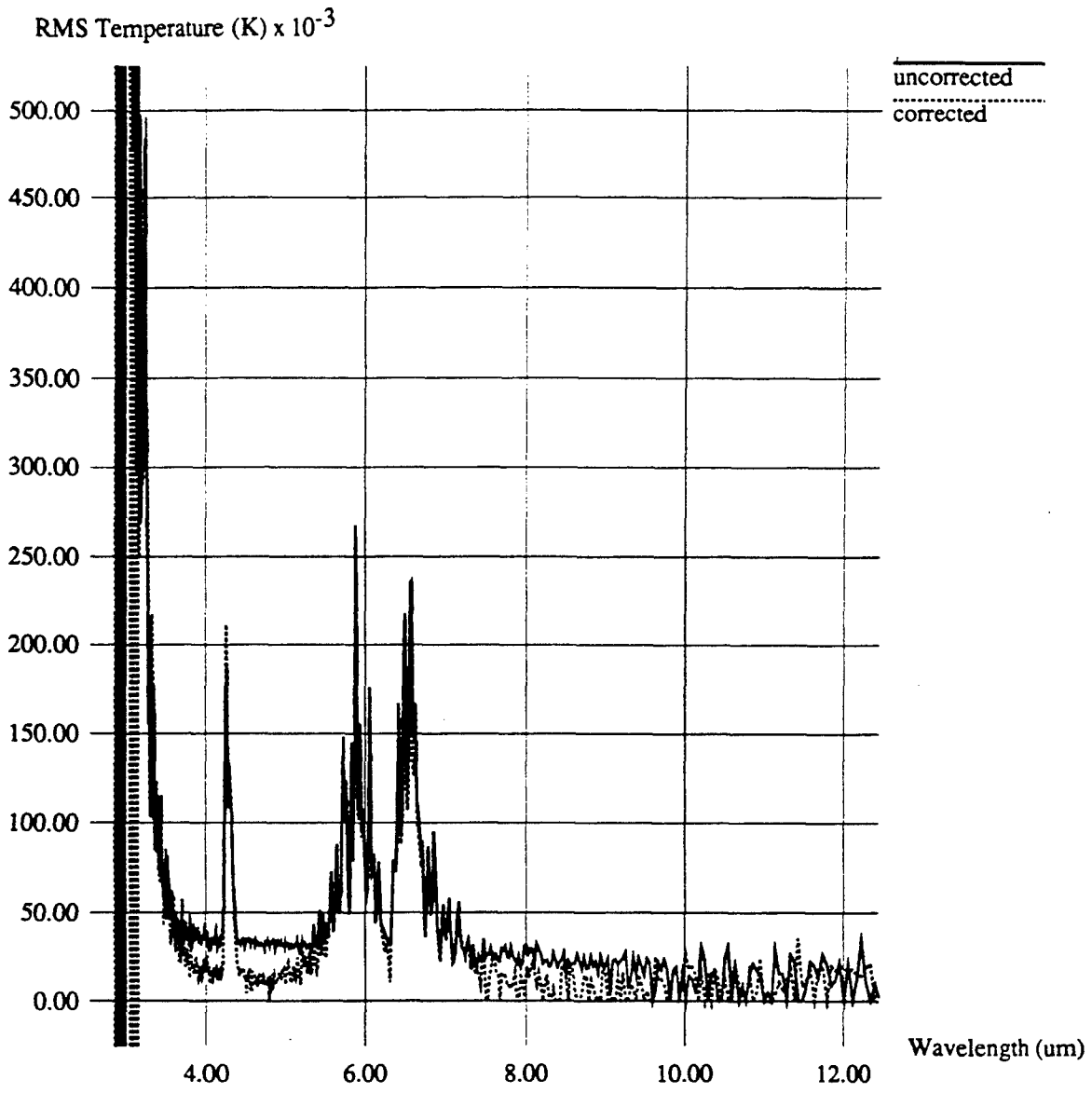


Figure 4-23. FTS Stability on 7-19-93.

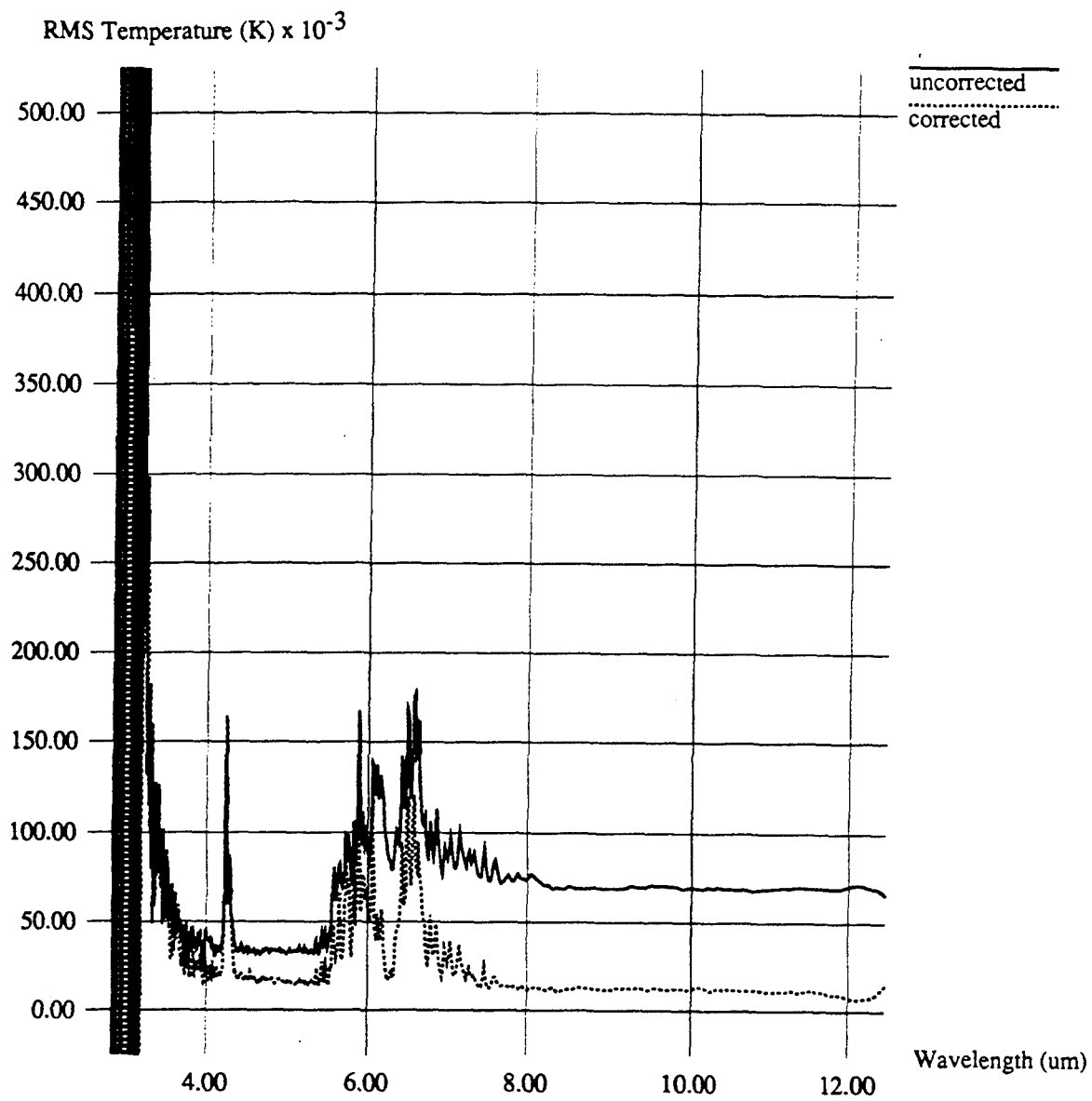


Figure 4-24. FTS Stability on 7-20-93.

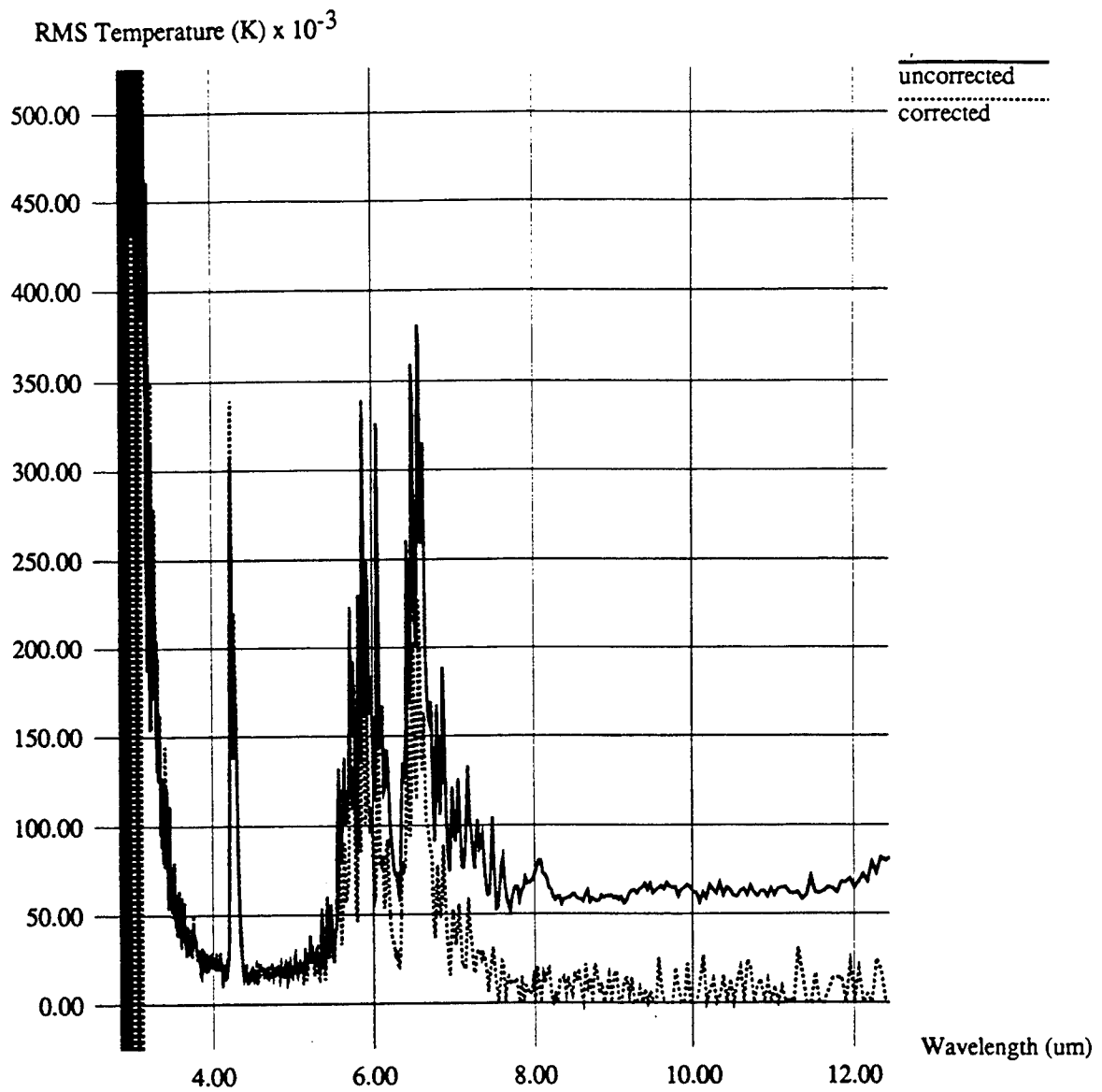


Figure 4-25. FTS Stability on 7-21-93.

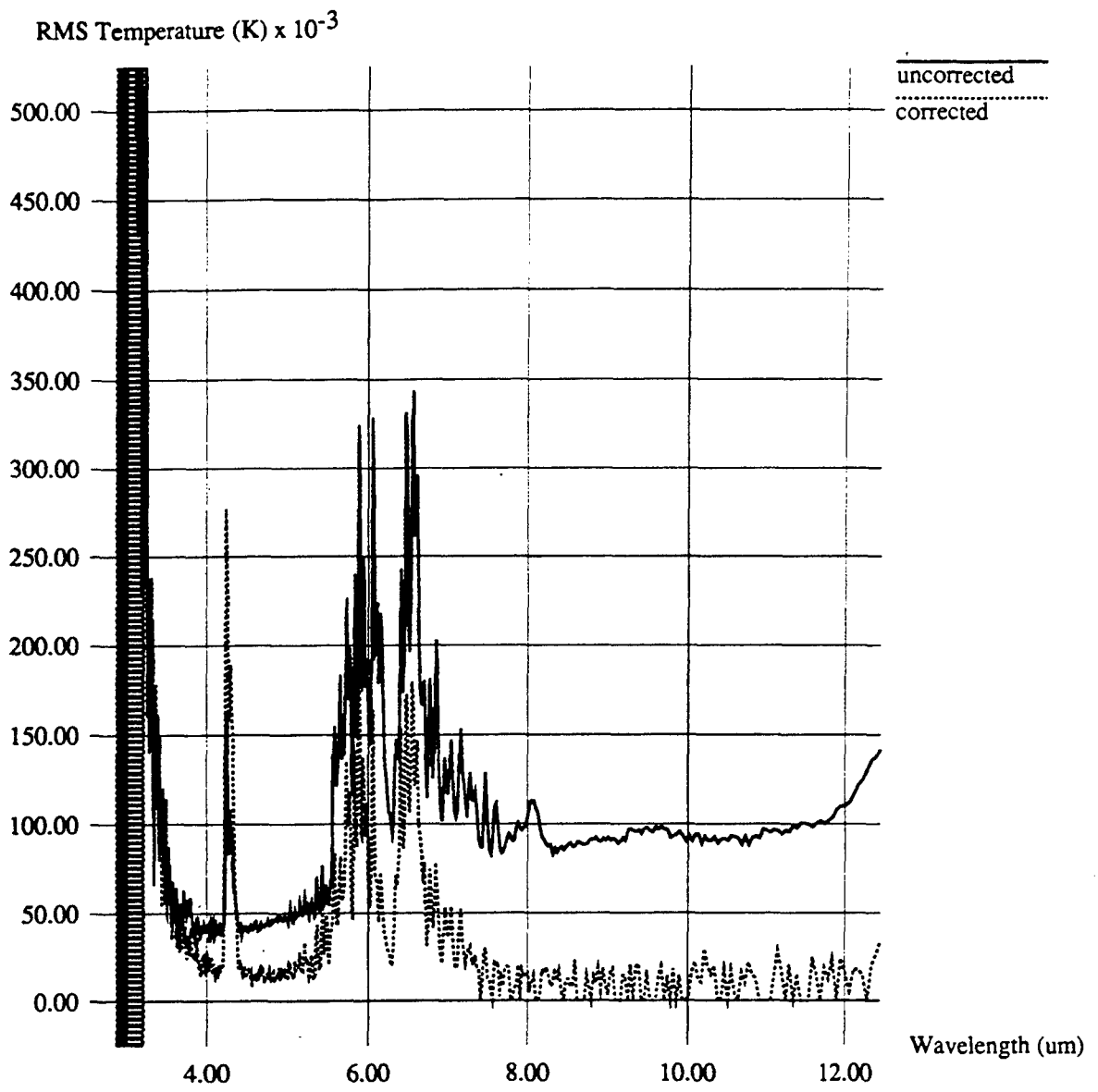


Figure 4-26. FTS Stability on 7-22-93.

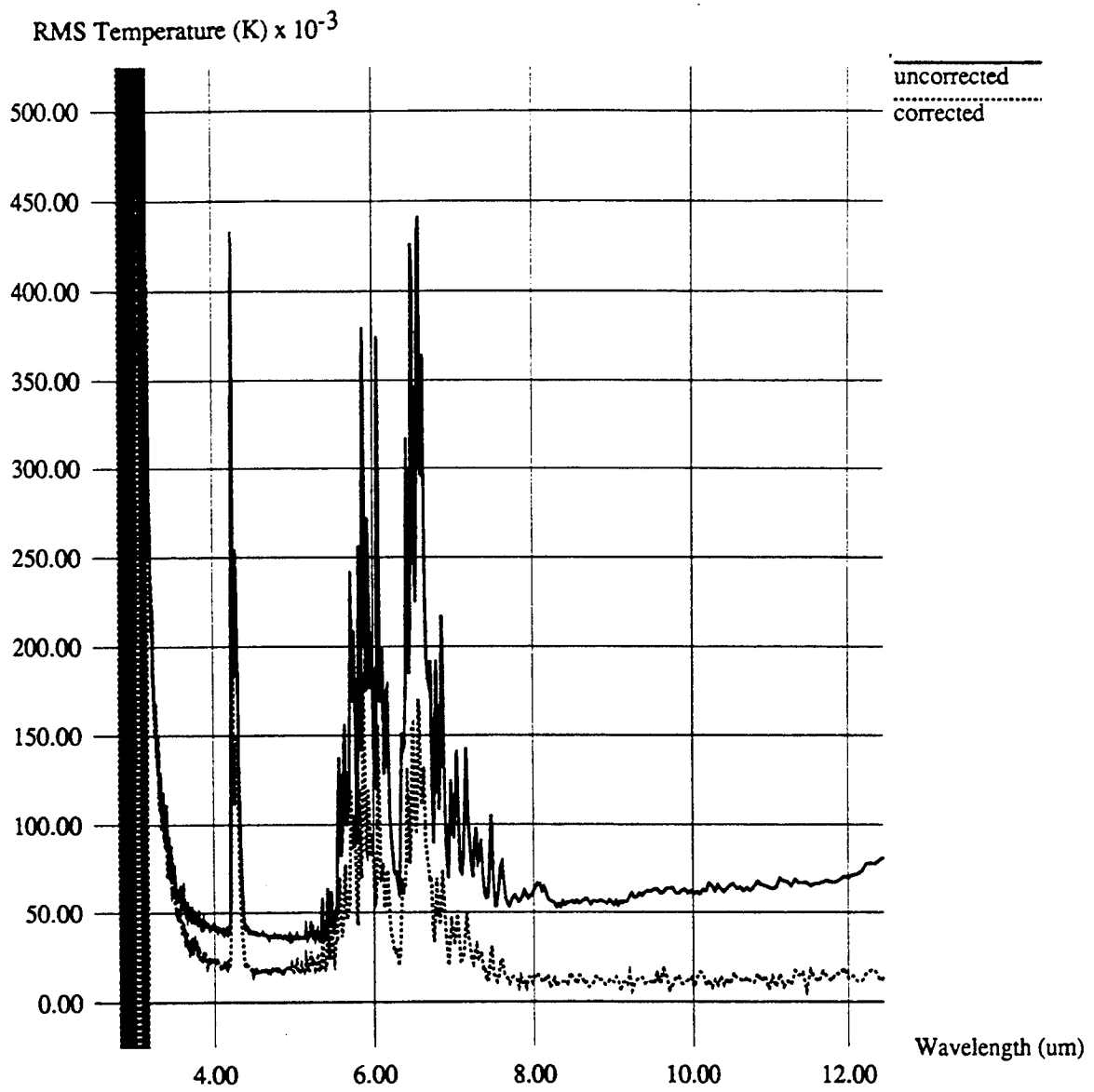


Figure 4-27. Average FTS Stability.

themselves in the interferogram and it is not clear how exactly they affect the measured spectrum.

The objective of the response linearity tests was not to understand the source of nonlinearities and how they propagate to the spectral domain, but to measure whether differential nonlinearities exist in the measured spectra and, if so, whether a significant decorrelation results. To facilitate this, measurements were made of the EOI blackbody at 15C, 20C, 25C, 30C, 35C, 40C, and 45C setpoints. The large temperature range was chosen to maximize the anticipated small nonlinearity. In order to minimize the effect of FTS instability, the measurements were made over as short a time frame as possible. This obviously had to be traded off for the effect of blackbody stability since minimizing the latter effect implies a long settling time at each setpoint. A 15-minute interval between setpoints was chosen as a compromise.

Figure 4-28 shows a scatter plot of the 4.7 and 10 micron measurements as compared to blackbody predictions. The nearly constant offset between the measurements and predictions is due to the fact that calibration was performed with old calibration data. This is of no consequence with regard to linearity. What is important is the curvature of plots, which illustrates differential nonlinearity. This is seemingly the same for the measured and predicted data, which suggests that there is no visible response nonlinearity beyond that predicted by the blackbody function. This suggests that any FTS response nonlinearity is at least somewhat less than that of the blackbody function.

A better test of the effect of nonlinearity is the spectral correlation of the measurements. This is shown in Figures 4-29 and 4-30 with 4.7 and 10 micron reference wavelengths. The measured curves clearly follow the theoretical limit, which was computed from a set of theoretical spectra of blackbodies of the same temperature points as the measured data. It is possible that the residual difference is due to additional response nonlinearity, but it could equally be due to FTS instability over the 1.5-2 hour total measurement time. In any case, these results indicate strong linearity of response to incoming radiance.

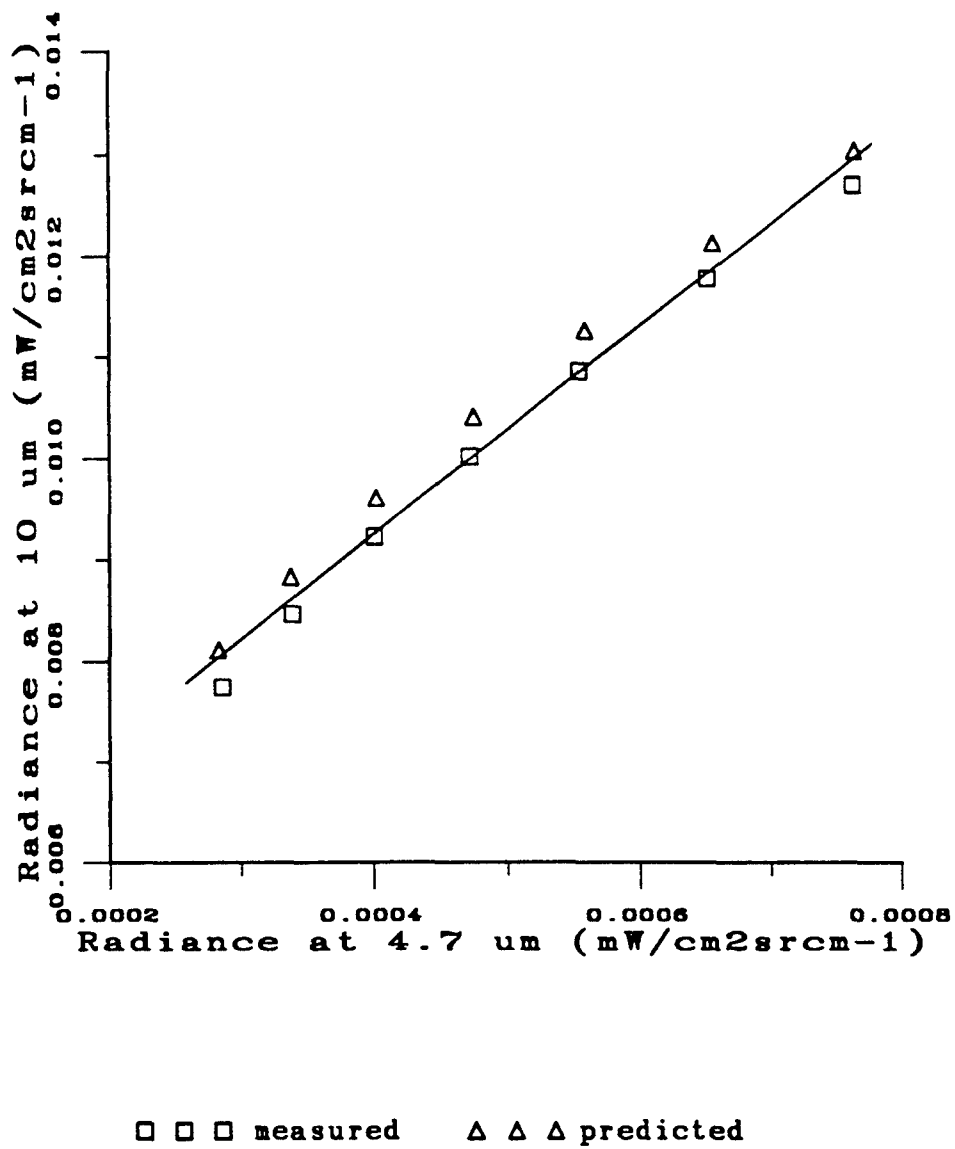


Figure 4-28. Scatter Plot of Linearity Measurements Compared to Blackbody Predictions.

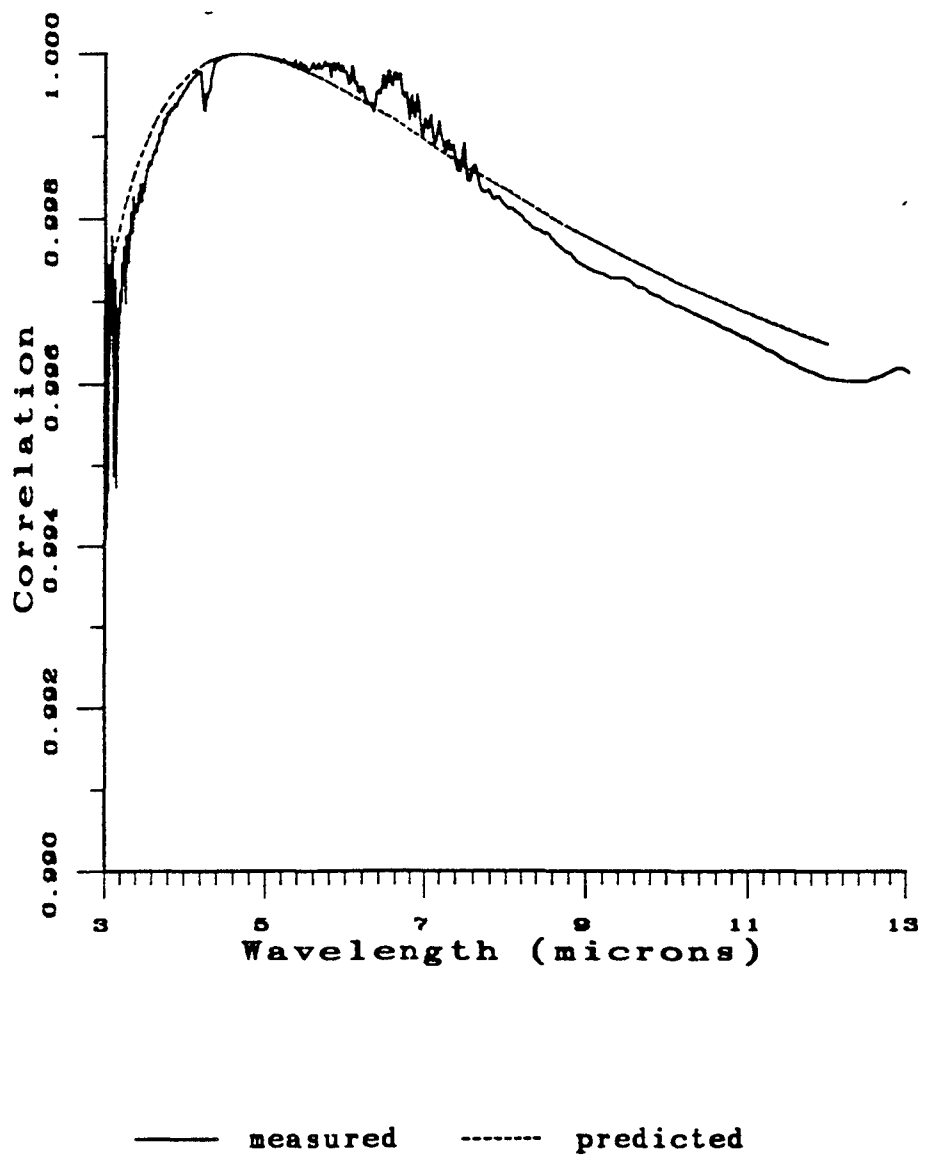


Figure 4-29. Linearity Test via Correlation With 4.7 microns.

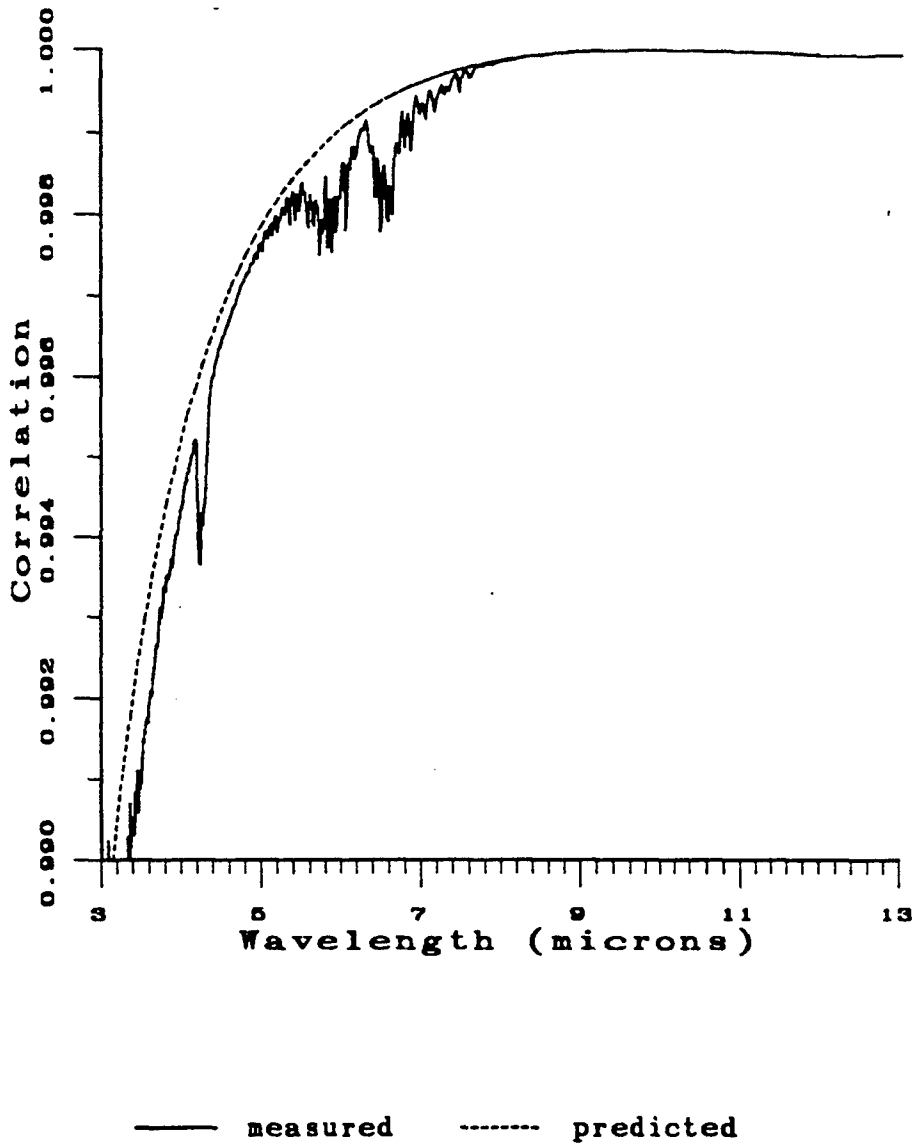


Figure 4-30. Linearity Test via Correlation With 10 microns.

The conclusions with regard to linearity are:

- 1) The response nonlinearity of the FTS is, at most, a fraction of theoretical blackbody nonlinearity.
- 2) The resulting effect on spectral correlation is negligible.

No sensor modifications were made to explicitly improve response linearity.

4.6 POLARIZATION SENSITIVITY

A sensor polarimetric throughput difference, particularly if it is spectrally dependent, can result in measured spectral variations which are truly due to polarization variances of the measured target. The extent of this problem in a radiometric sense is ultimately tied to the polarimetric nature of the target. Therefore, a full understanding of polarization sensitivity requires detailed knowledge of these polarization properties.

This, however, was not the objective of the polarization sensitivity tests. Rather, the objective was to understand the origin and extent of sensor throughput as a function of polarization orientation (i.e., horizontal and vertical) and wavelength. Given this information, along with a suitable polarimetric target model, the spectroradiometric perturbations can confidently be predicted.

There are two possible sources of polarization sensitivity in the FTS optical design a ZnSe dichroic beamsplitter used to extract boresight video and a KBr beamsplitter in the Michelson interferometer. Both optics are coated; therefore, their polarimetric throughput can not be readily computed from their material properties using Fresnel Equations. Because of this, as well as the fact that Bomem was unable to provide polarization data on these components, we had no basis for estimating polarization sensitivity prior to FTS delivery.

Several techniques were utilized for measuring the sensor polarization sensitivity, all of which were based on the use of a thin film wire grid polarizer to produce polarized radiation from a cavity blackbody source. The polarizer achieves better than a 200:1 extinction ratio of the cross polarized transmitted radiation over the entire spectral range, which is more than adequate. The difficulty, however, is in canceling out the effect of

the cross polarized reflected ambient radiation, which is significant even with a 90-100C cavity.

We found the following procedure to be the best for overcoming this difficulty. First, calibration data were collected at 20C and 45C cavity setpoints. Next, the polarizer was placed between the cavity and the FTS. From this point on, extreme care was taken such that the orientation (tilt) of the polarizer did not change. Measurements were then made at vertical and horizontal rotational orientations of the polarizer of the 45C cavity. Finally, the cavity was slewed to a 90C setpoint and measurements were repeated for horizontal and vertical polarizer orientations. This procedure was followed with the video diverter in place and with it removed (along with the collimator since removal from the collimator would require a complete optical system realignment).

The results were computed in the form of a polarimetric contrast defined by

$$C_P = \frac{[L_V(90C) - L_V(45C)] - [L_H(90C) - L_H(45C)]}{[L_V(90C) - L_V(45C)] + [L_H(90C) - L_H(45C)]}$$

where L_V and L_H are the measured radiances at the indicated cavity setpoints for vertical and horizontal polarizer orientations, and all quantities are implicitly spectrally dependent. By differencing the measured 90C and 45C radiances for each polarizer orientation, the common reflected component is removed such that the bracketed terms will indicate purely polarized radiances.

The results are shown in percent form in Figure 4-31. The instrument clearly shows some polarization sensitivity. The spectrally dependent portion is attributed to the KBr beamsplitter, and exhibits on the order of 5% spectral variability. In addition, the ZnSe video diverter apparently produces an additional 6% polarimetric throughput difference, although this is roughly spectrally constant.

The conclusions with regard to polarization sensitivity are:

- 1) The FTS exhibits an appreciable polarimetric response.
- 2) The KBr beamsplitter is the primary source of the spectrally dependent component

Pct. Contrast

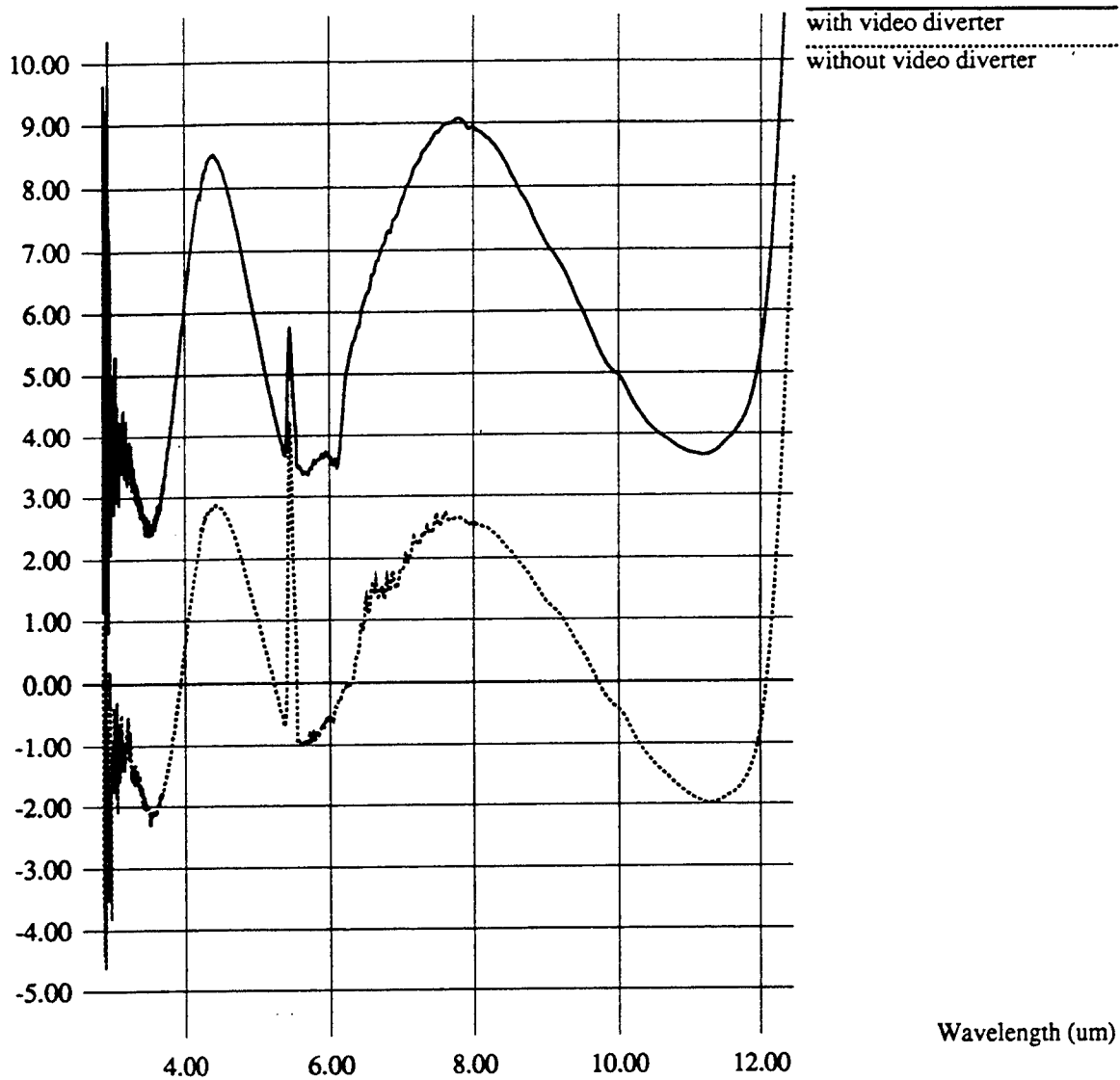


Figure 4-31. Polarization Test on 8-31-93.

- 3) The video diverter is the primary source of the mean, spectrally flat component.
- 4) Further analysis incorporating a polarimetric target model is needed to evaluate the effect of this sensitivity on spectroradiometric measurements.

No sensor modifications were made to explicitly improve polarization sensitivity.

4.7 SPATIAL REGISTRATION

The Bomem FTS has several attributes that allow it to achieve very good band-to-band spatial registration. First, all optical elements with power are reflective and hence achromatic. Second, the Fourier transform spectrometer design allows all wavelength bands to be measured with a single detector. Finally, the optical design is that of a pupil plane radiometer such that spatial responsivity variations of the detector are not a factor.

The exception to the above is the use of two detector modules (InSb and MCT) to maximize sensitivity over the entire spectral range. These two channels are complimentary outputs of the Michelson interferometer. The optical design is such that there is a secondary field aperture in each postinterferometer optical train, which is at the image plane of the front aperture. If these apertures are equal in size or smaller than the front aperture, small relative misalignments in these optical trains or secondary aperture positions result in spatial misregistration between the MWIR and LWIR channels through a vignetting effect. This would not occur if the front aperture was always the limiting aperture (i.e., smaller). The penalty paid in this instance, however, is reduced sensitivity and potentially increased radiometric instability.

The objectives of the spatial registration tests were to verify the high degree of registration within each detector module and to quantify the amount of mis-registration between modules. The initial approach to perform this was to spatially scan the FTS across a distant bright infrared line source and directly map the spatial footprint of the sensor as a function of a wavelength. This failed, however, due to the inability to find a compact source with sufficiently high existence. The fallback was a line spread test

in which the sensor was scanned across an edge discontinuity formed by abutting an emissive panel and a reflective panel specular to the sky.

The normalized line spread function for several wavelengths is shown in Figure 4-32. The 3.8 and 4.7 micron bands were measured with the InSb detector and the other bands with the MCT detector. Within each detector module, registration is clearly exceptionally good. Between modules, however, the measurements indicate roughly an IFOV/14 mis-registration and 2% difference in IFOV width. This is on the order of Bomem's expectation.

The conclusions with regard to the spatial registration of the FTS sensor system are:

- 1) Spatial misregistration between wavelength bands measured by the same detector module (MWIR or LWIR) are negligible.
- 2) Module to module spatial registration is on the order of an IFOV/14.
- 3) The effect of this mis-registration on spectroradiometric measurements is dependent on the particular type of measurement made as well as target/background characteristics.

No sensor modifications were made to explicitly improve spatial registration, although we are currently working with Bomem to determine the possibilities. Decreasing the front aperture size is one option, but is not necessarily desirable.

4.8 CORRELATION PRESERVATION

One of the overriding requirements of the MSSP field data collection was the ability to measure environment limited spectral correlation. This was anticipated in some cases to be on the order of 0.9999 for a 1 degree Celsius temperature standard deviation. The objective of the correlation preservation tests was to directly measure the sensor spectral correlation measurement limit throughout the field data collection campaign.

The test developed for this purpose consisted of taking an alternating sequence of measurements of the blackbody calibration sources at setpoints of 24C and 26C (one degree Celsius standard deviation). Because the blackbodies are, in principle

Relative Response

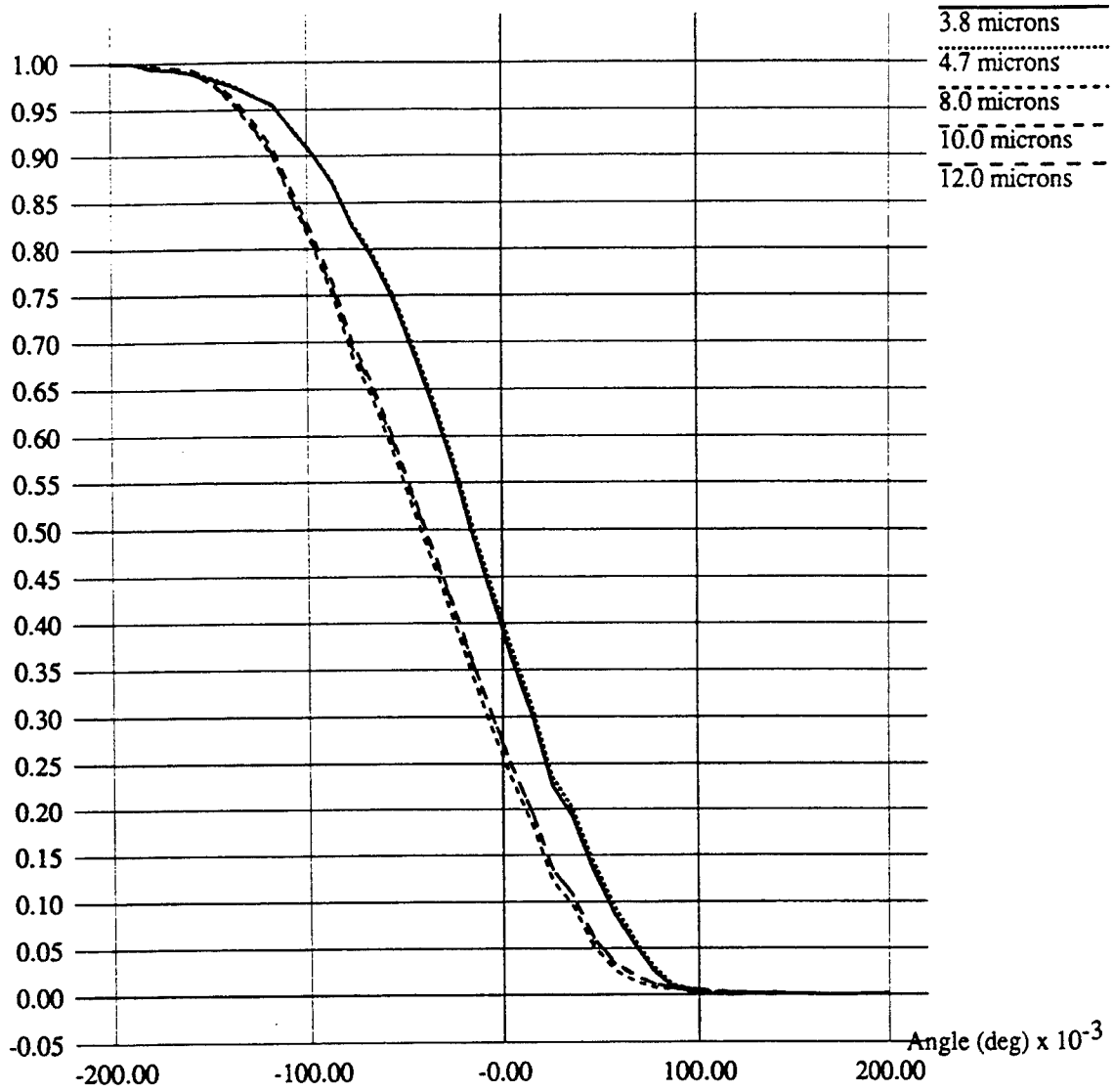


Figure 4-32. Spatial Registration Test via Line Spread Function.

deterministic, the measured spectral correlation should be unity, such that any measured decorrelation is due to sensor limits. This method directly measures the limitation on spectral correlation due to sensor noise, calibration inaccuracy and radiometric instability. Since only two temperature setpoints could be measured, effects of nonlinearity are not included, although decorrelation due to nonlinearity was specifically addressed in a separate test. Decorrelation due to polarization sensitivity and spatial mis-registration are also not included since the blackbodies are non-polarimetric and spatially uniform.

The correlation preservation tests were performed on several days throughout the WPAFB and MICOM data collection campaigns (they are, in fact, the same tests as used for estimating FTS and blackbody instability). A typical set of experiment parameters (30 measurements, 25 coadded scans, 20-30 minute total measurement time) was used and the temporal calibration was employed to remove linear FTS gain and offset drifts.

The results for each separate measurement are given in Figures 4-33 to 4-40 in the form of the spectral decorrelation (one minus the measured correlation) with both a 4.7 and 10 micron reference wavelength on a logarithmic scale. Table 4-3 summarizes the average measured correlation between several wavelengths with and without temporal calibration. With temporal calibration, the sensor typically achieves better than 0.99995 correlation within the LWIR, 0.9999 within the MWIR, and 0.9995 between the MWIR and LWIR. This ignores the short end of the MWIR (< 4 microns) where the correlation rolls off (0.999 at 3.8 μm) due to sensor noise. Figure 4-41 shows the averaged measured sensor correlation limit.

Table 4-3: Correlation Test Results With and Without Temporal Calibration.

	No Temporal Calibration		With Temporal Calibration	
	4.7 μm	10 μm	4.7 μm	10.0 μm
3.8 μm	0.99933	0.99530	0.99930	0.99898
4.7 μm	1.00000	0.99627	1.00000	0.99966
8.0 μm	0.99710	0.99976	0.99973	0.99998
10.0 μm	0.99625	1.00000	0.99966	1.00000
12.0 μm	0.99367	0.99959	0.99950	0.99995

Decorrelation

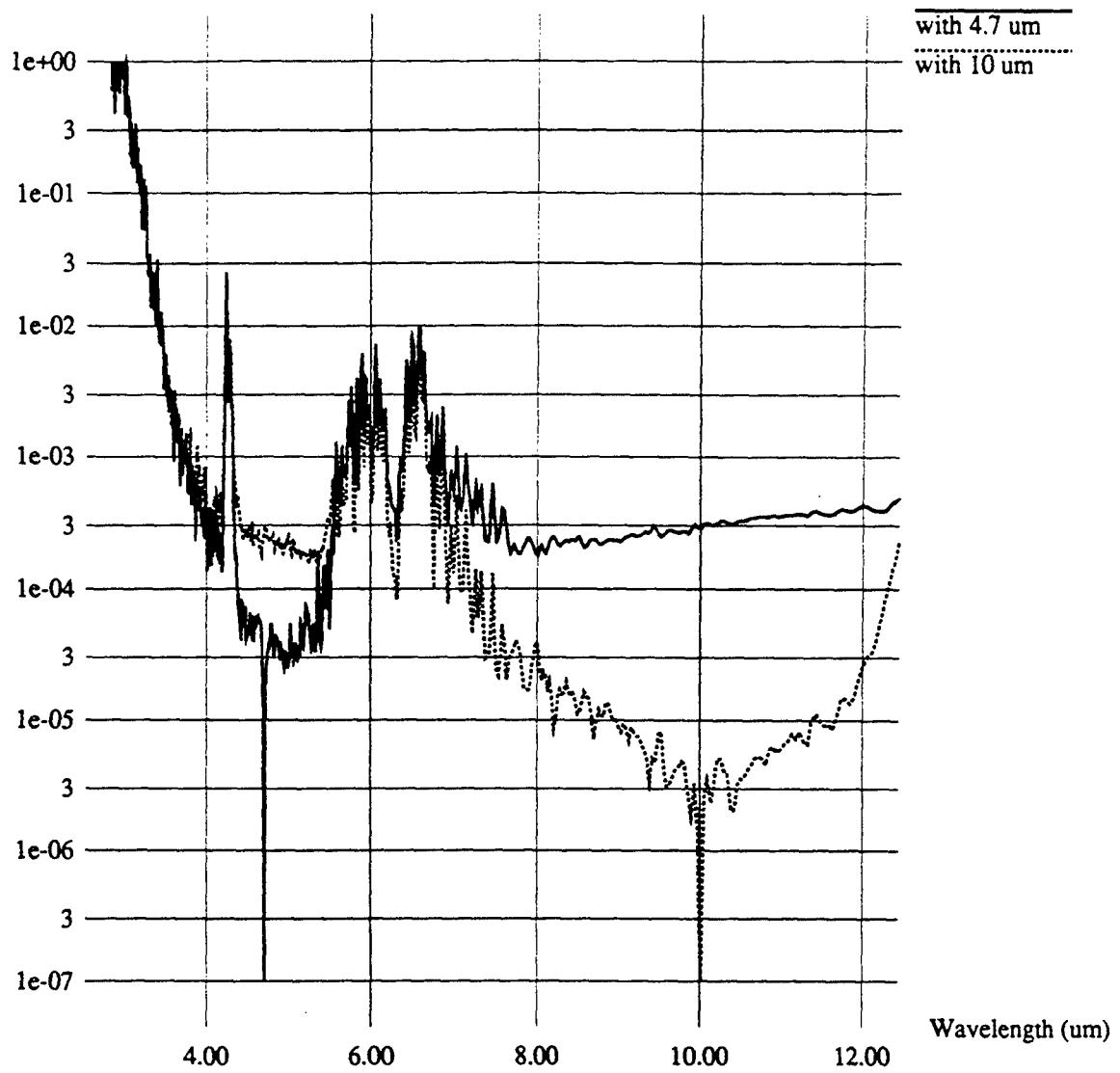


Figure 4-33. Decorrelation on 7-7-93 (#1).

Decorrelation

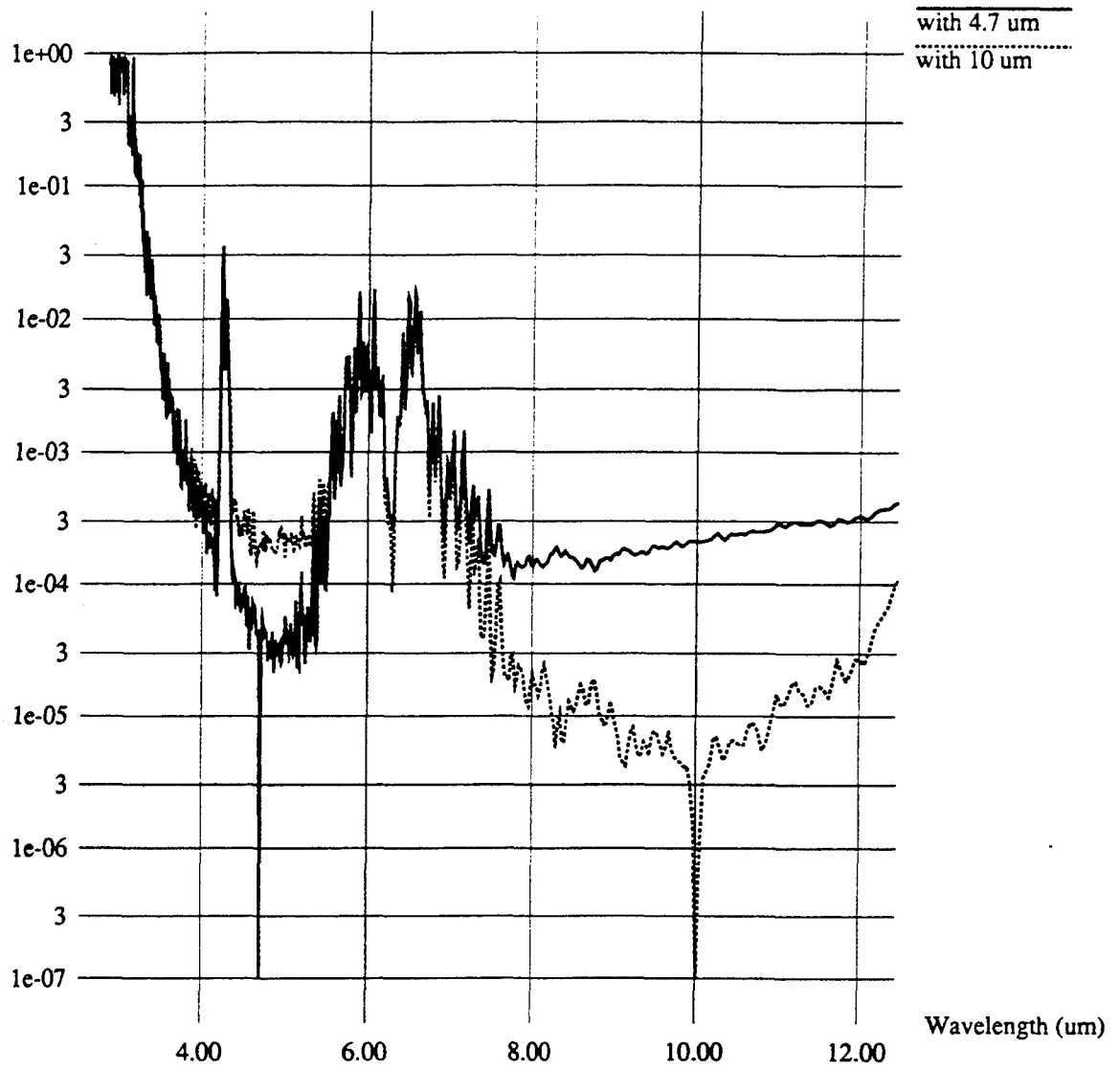


Figure 4-34. Decorrelation on 7-7-93 (#2).

Decorrelation

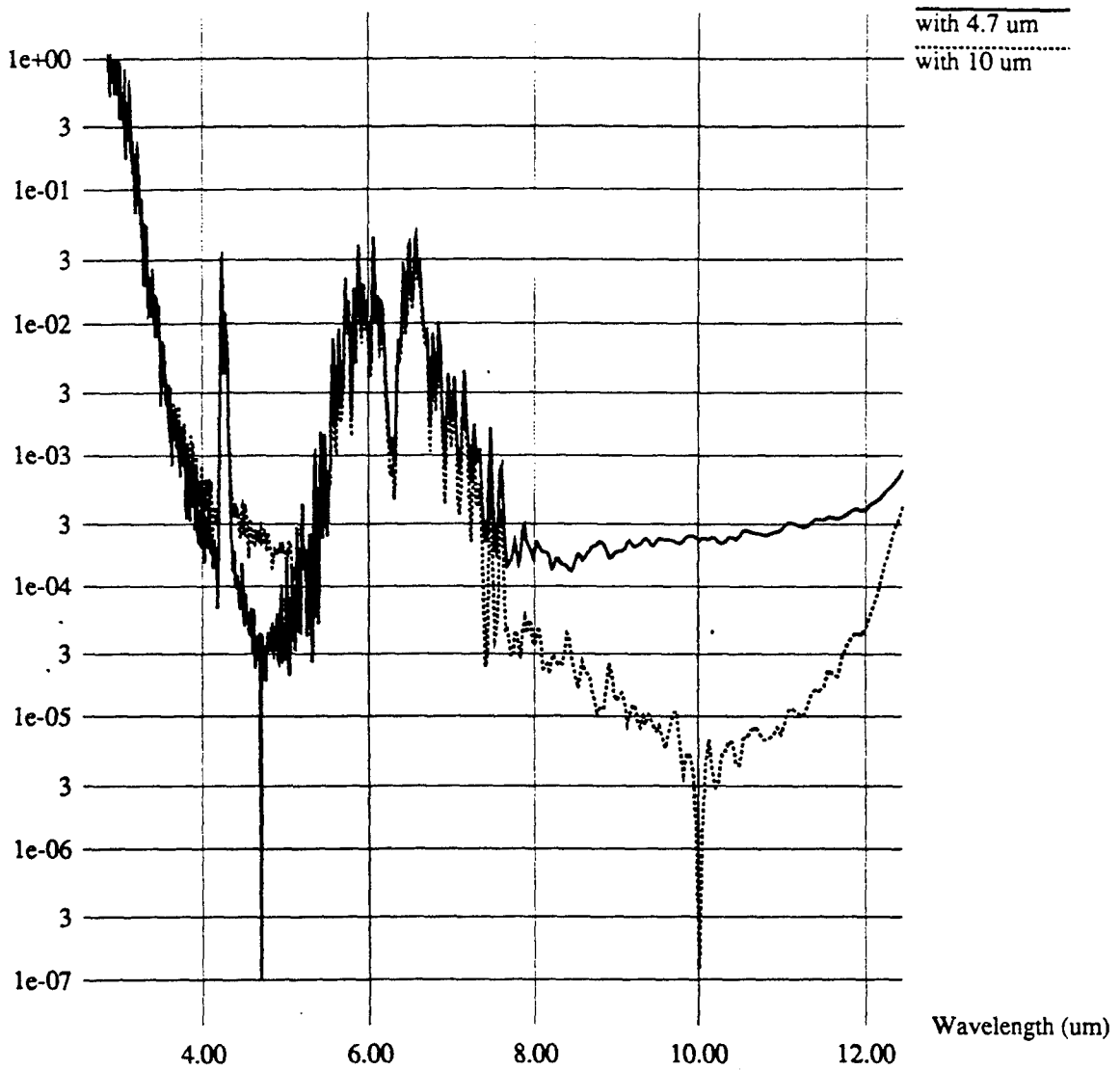


Figure 4-35. Decorrelation on 7-16-93.

Decorrelation

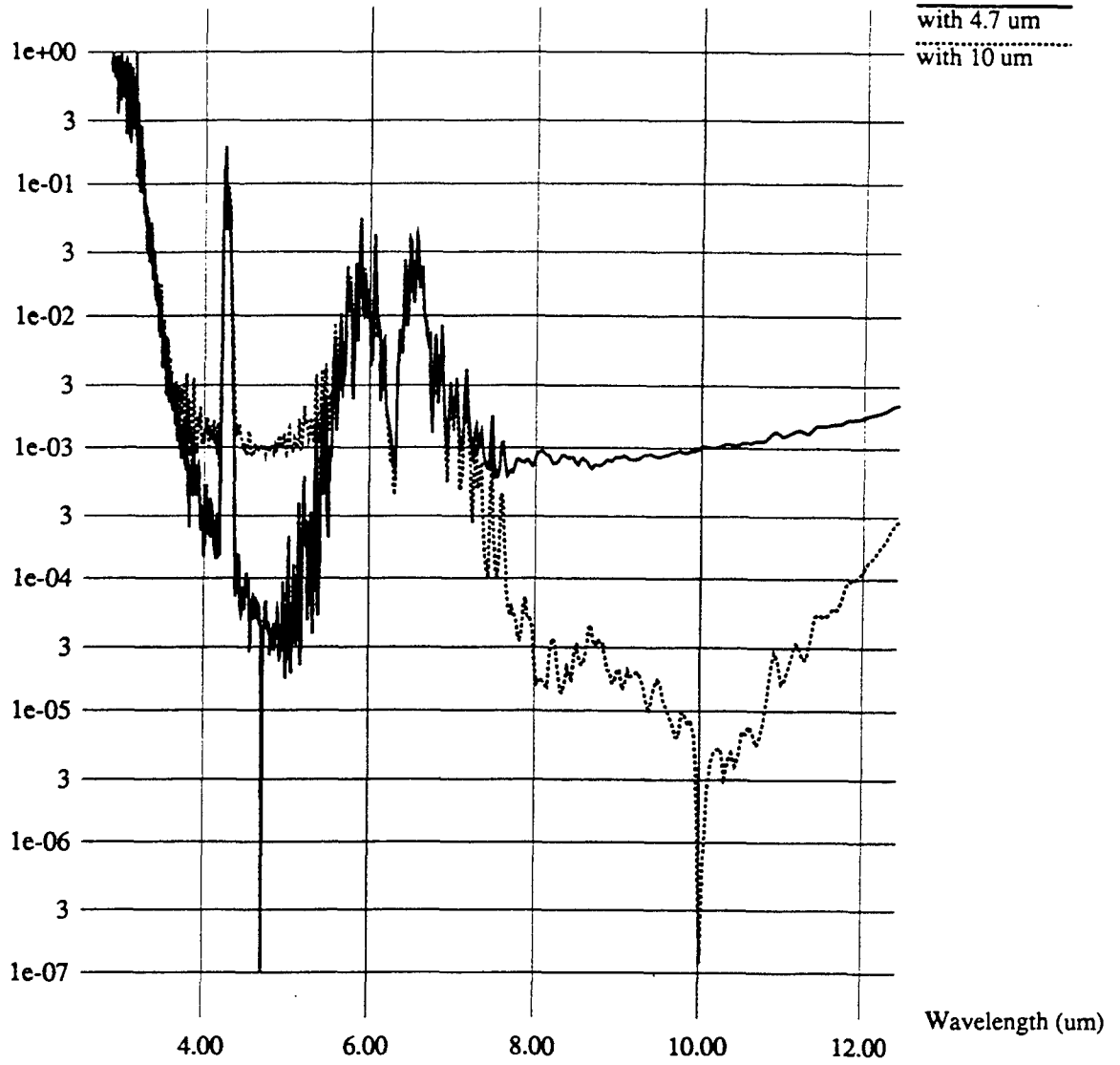


Figure 4-36. Decorrelation on 7-17-93.

Decorrelation

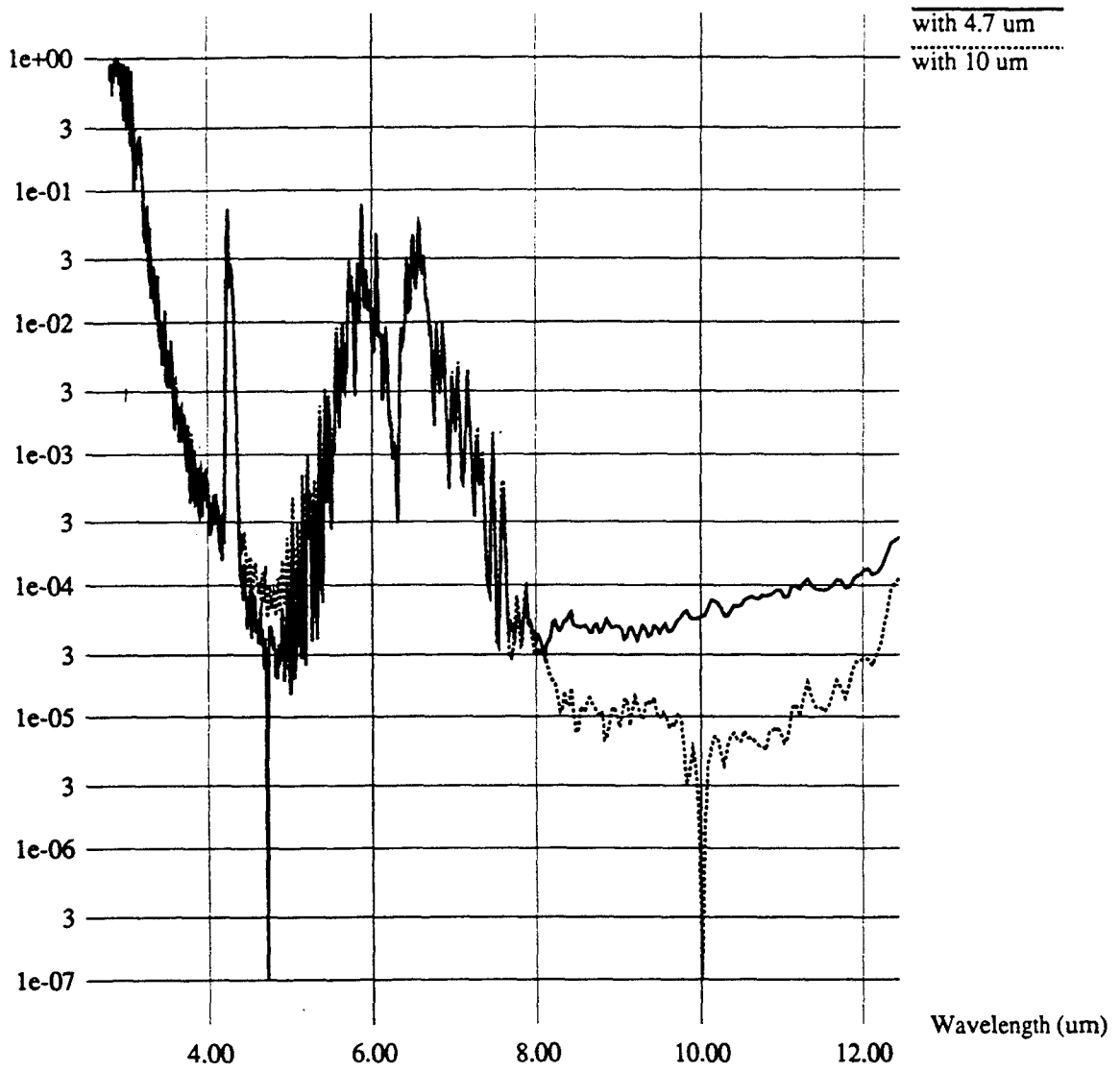


Figure 4-37. Decorrelation on 7-19-93.

Decorrelation

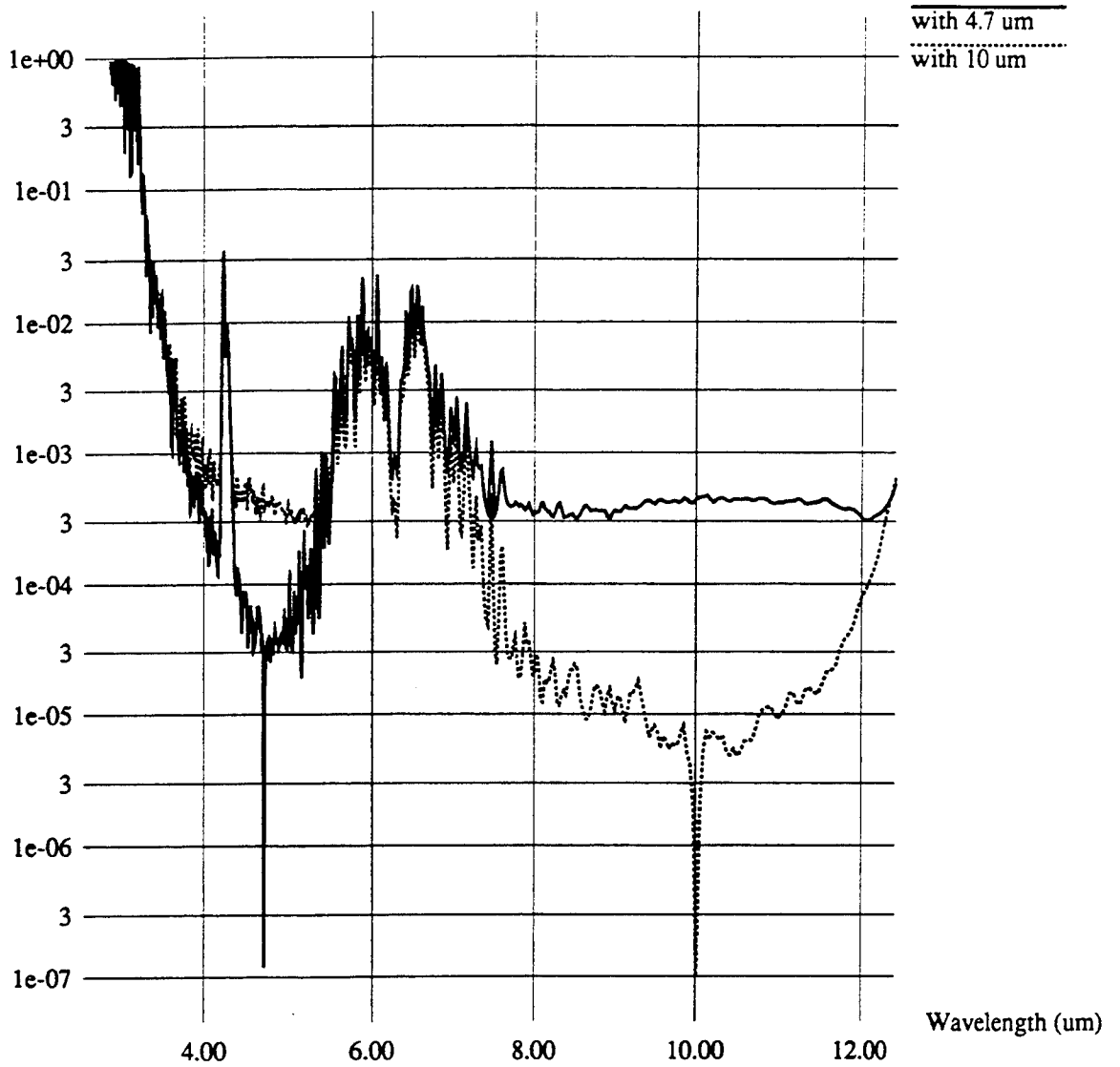


Figure 4-38. Decorrelation on 7-20-93.

Decorrelation

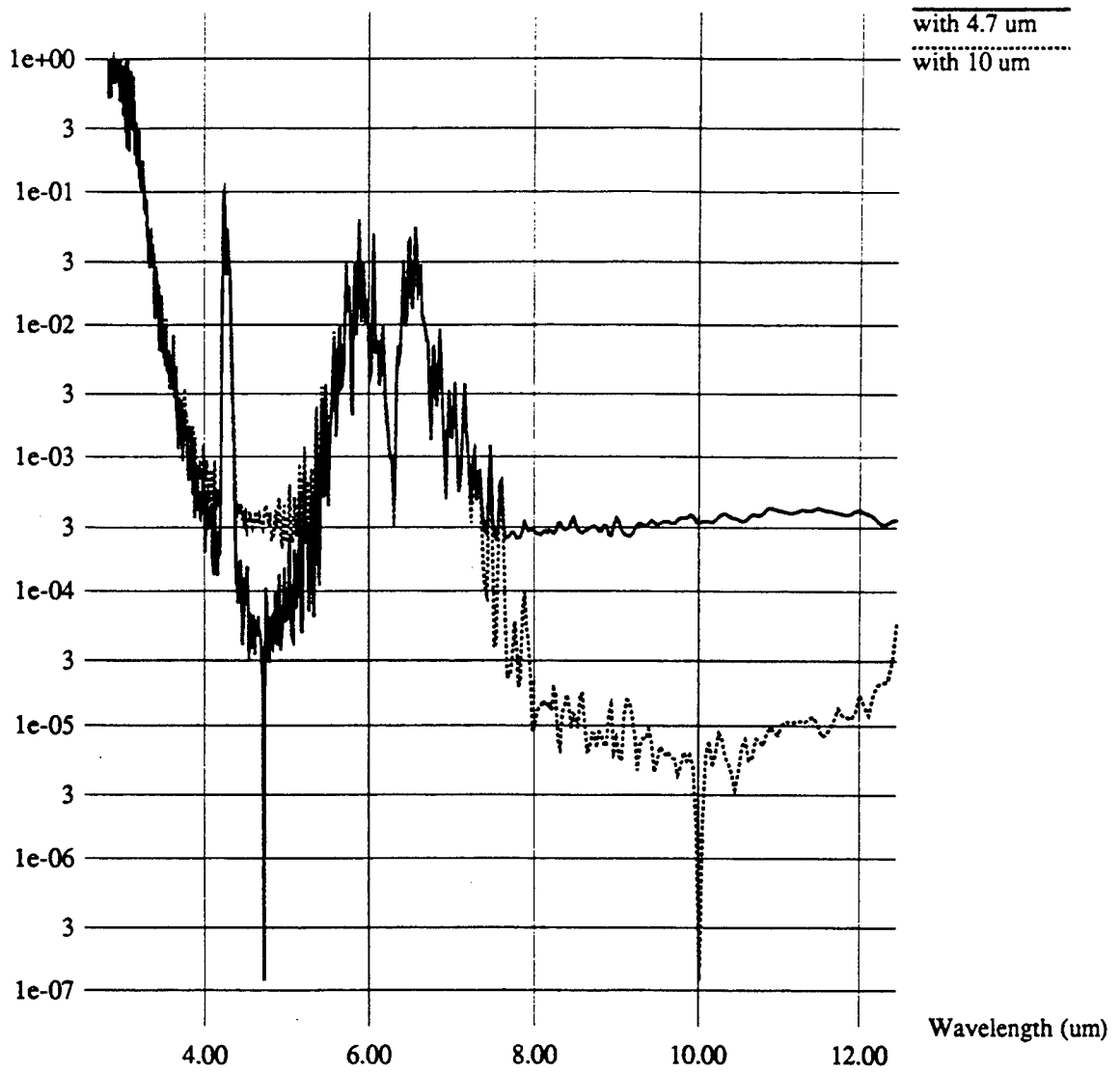


Figure 4-39. Decorrelation on 7-21-93.

Decorrelation

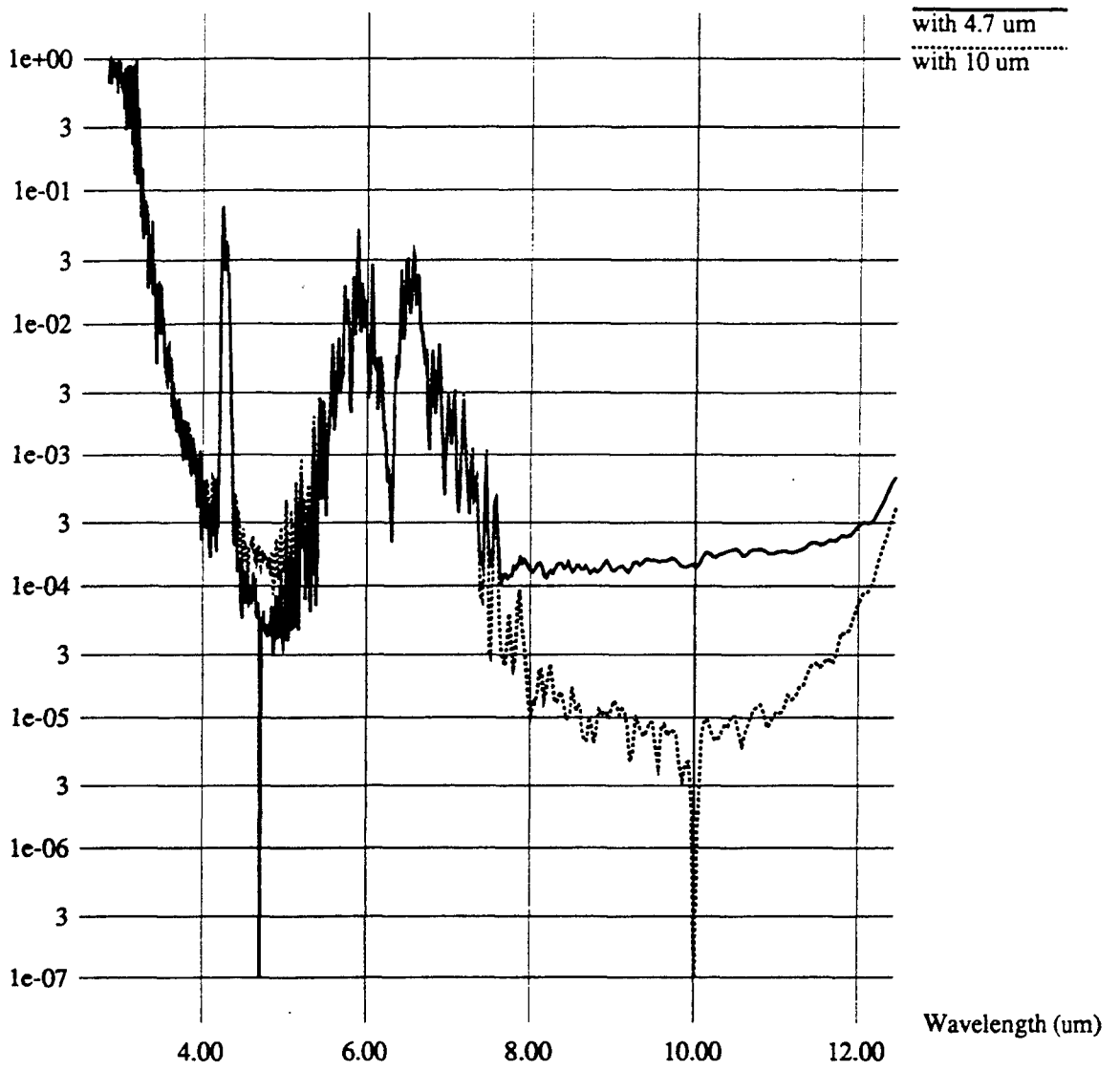


Figure 4-40. Decorrelation on 7-22-93.

Decorrelation

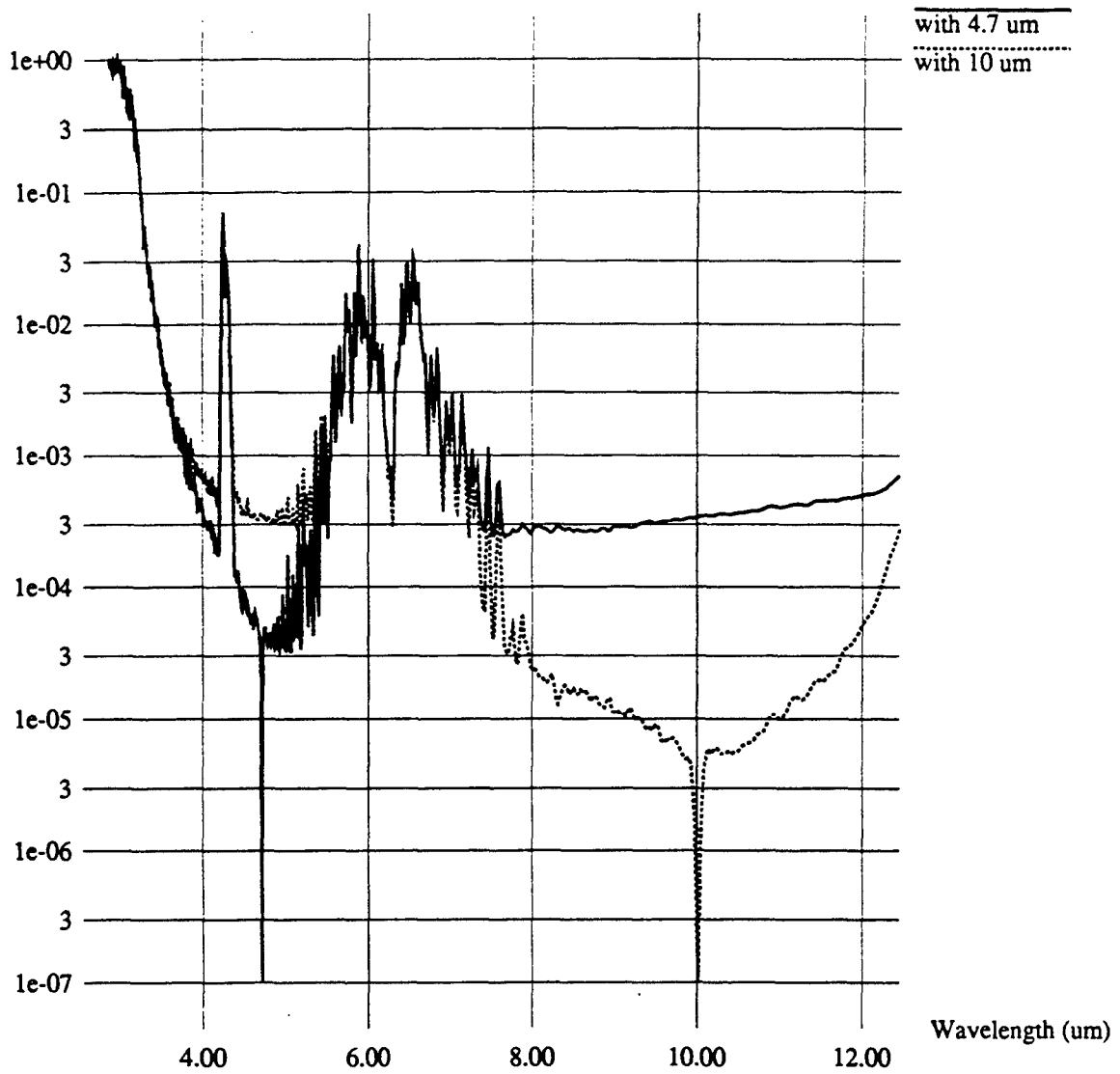


Figure 4-41. Average Decorrelation.

The conclusions with regard to the correlation preservation of the FTS sensor systems are:

- 1) Measurements indicate the sensor's ability to measure levels of correlation in the 0.9999 range.
- 2) Achievement of good correlation preservation relies in most instances on the use of temporal calibration.
- 3) The measurement technique did not allow the evaluation of possible decorrelation due to polarization sensitivity and spatial mis-registration.

Sensor modifications made to improve FTS stability were primarily geared to maximizing the sensor ability to preserve spectral correlation. Ideally, one should develop test procedures for incorporating decorrelation due to polarization sensitivity and spatial registration, but this is difficult due to problems associated with developing a controlled test object and the extremely target dependent nature of these effects.

4.9 POINTING REPEATABILITY

Pointing repeatability is determined by the backlash and run-out of the azimuth and elevation rotary drives as well as the rigidity of the entire mechanical pointing system. The objective of the pointing repeatability tests was to quantify the overall performance as a function of scan characteristics (step size and direction). This was performed by using the boresight video with a spatially calibrated target. The sensor was pointed repetitively to the target using an approach from different angular deviations and directions. The measurement limit was on the order of an IFOV/100 or roughly 10 arc sec. The rotary stages are specified to maintain 5 arc sec unidirectional repeatability. Backlash is adjustable, but is expected to be on the order of 30 arc sec.

The results of the measurements are summarized in Table 4-4. For a unidirectional approach or small bidirectional approaches ($<0.01^\circ$), deviations on the order of the measurement limit existed. For larger bi-directional approaches, the deviations were on the order of the anticipated backlash. In all cases, the deviations were well within requirements.

Table 4-4: Pointing Repeatability Measurements Results

Step Size	Repeatability	
	Unidirectional	Bidirectional
<0.01°	< 10 arc sec	< 10 arc sec
0.01 to 1.0°	< 10 arc sec	< 30 arc sec
> 10°	< 10 arc sec	< 30 arc sec

Note: Sensor IFO = 5 mrad = 17.2 arc min = 1030 arc sec

The conclusions with regard to pointing repeatability of the FTS sensor system are:

- 1) The measured unidirectional and bi-directional repeatability was consistent with the stringent specifications of the rotary drives.
- 2) The measured deviations are well within the MSSP requirements.

No sensor system modifications were made to explicitly improve pointing repeatability.

4.10 POINTING STABILITY

The pointing stability of the FTS sensor system is dictated primarily by three factors the rigidity of the pointing mount, the rigidity of the FTS telescope mount, and the stability of the sensor platform (i.e., tower). Each of these factors will influence stability differently whether the pointing system is at rest (steady state) or is in the process of or just ended a move (transient).

The objectives of the stability tests were to understand the magnitude and source of the transient and steady state instabilities due to the first two factors, as well as estimate the settling time (time lag after a move at which steady state is achieved). The final effect is site specific. For example, we found it to be negligible in the WPAFB tower, but significant in the MICOM tower, especially when the elevator was in motion

or, even more so, when the sensor was situated in the elevator ("significant" refers to on the order of IFOV/20 to IFOV/10 instability).

Pointing stability tests were conducted in a similar manner as the pointing repeatability tests. The sensor was repetitively pointed to the spatially calibrated target using an approach from different angular deviations and directions. The boresight video was recorded on a time-stamped VCR and played back in slow motion to estimate the temporal behavior of the pointing errors. Angular measurement accuracy was on the order of an IFOV/100 or 10 arc sec, and temporal accuracy was roughly 0.5 sec.

The results of the measurements are summarized in Table 4-5. The steady state stability was near the measurement limit. The test was performed, however, on a fairly calm day. On windy days, the telescope mount becomes the major source of steady state instability, which can rise to roughly an IFOV/20. For small angular displacements, there are no significant transient deviations. For large displacements, however, transient fluctuations do occur, but settle out mostly in the first second and completely after 3 seconds. Due to the simultaneity of the FTS, even these fluctuations will have no effect on spectral correlation and negligible effect on the measurements.

Table 4-5: Pointing Stability Measurements Results

Step Size	Time After Step	Stability
< 1°	0-1 sec	< 10 arc sec
	1-3 sec	< 10 arc sec
	> 3 sec	< 10 arc sec
> 10°	0-1 sec	100 arc sec
	1-3 sec	25 arc sec
	> 3 sec	< 10 arc sec

Note: Sensor IFOV = 5 mrad = 17.2 arc min = 1030 arc sec.

The conclusions with regard to pointing stability of the FTS sensor system are:

- 1) A small amount of steady state instability can occur due to wind-induced telescope vibration or tower instability; otherwise, it was immeasurable.
- 2) Transient instabilities only occur for large (10° or larger) angular displacements and settle out after 1-3 seconds.
- 3) The effects of these measured levels of pointing instability are negligible with respect to spectroradiometric measurements, primarily due to the simultaneity aspect of the FTS.

No sensor system modifications were made to explicitly improve pointing stability.

4.11 REFERENCES

- [4.1] H.E. Revercomb, et al., "Radiometric Calibration of IR Fourier Transform Spectrometers: Solution to a Problem With the High-Resolution Interferometer Sounder," *Applied Optics*, Vol. 27, No. 15, pp. 3210-3218, 1 August 1988.

5.0 SENSOR CHARACTERISTICS ANALYSIS

5.1 MEASUREMENT STATISTICS

For most of the sensor characteristics considered in this chapter, we can use a linear model for the measured signal radiance $\hat{L}(\lambda)$ such that:

$$\hat{L}(\lambda) = a(\lambda)L(\lambda) + b(\lambda) \quad (5-1)$$

where $a(\lambda)$ is the sensor gain with unity mean and variance $\sigma_a^2(\lambda)$, $b(\lambda)$ is the sensor bias with zero mean and variance $\sigma_b^2(\lambda)$, and $L(\lambda)$ is the received radiance with mean $\mu_L(\lambda)$ and variance $\sigma_L^2(\lambda)$. The gain $a(\lambda)$ and bias $b(\lambda)$ are assumed uncorrelated with $L(\lambda)$. Given this linear model, the measured mean radiance $\hat{\mu}_L(\lambda)$ is:

$$\hat{\mu}_L(\lambda) = E[a(\lambda)L(\lambda) + b(\lambda)] = \mu_L(\lambda), \quad (5-2)$$

the measured variance is:

$$\begin{aligned} \hat{\sigma}_L^2(\lambda) &= E[\{a(\lambda)L(\lambda) + b(\lambda)\}^2] - \mu_L^2(\lambda) \\ &= \sigma_L^2(\lambda) + \sigma_b^2(\lambda) + \sigma_a^2(\lambda)\mu_L^2(\lambda) + 2\sigma_a(\lambda)\sigma_b(\lambda)\mu_L(\lambda)\rho_{ab}(\lambda) + \sigma_a^2(\lambda)\sigma_L^2(\lambda), \end{aligned} \quad (5-3)$$

and the measured correlation between two bands λ_1 and λ_2 is:

$$\hat{\rho}_L(\lambda_1, \lambda_2) = \frac{E[\{a(\lambda_1)L(\lambda_1) + b(\lambda_1) - \mu_L(\lambda_1)\} \{a(\lambda_2)L(\lambda_2) + b(\lambda_2) - \mu_L(\lambda_2)\}]}{\hat{\sigma}_L(\lambda_1)\hat{\sigma}_L(\lambda_2)} \quad (5-4)$$

$$\begin{aligned} &= \frac{\{\sigma_L(\lambda_1)\sigma_L(\lambda_2) + \sigma_a(\lambda_1)\sigma_a(\lambda_2)\rho_{aa}(\lambda_1, \lambda_2)\sigma_L(\lambda_1)\sigma_L(\lambda_2)\}}{\hat{\sigma}_L(\lambda_1)\hat{\sigma}_L(\lambda_2)} \times \rho_L(\lambda_1, \lambda_2) \\ &\quad + \frac{1}{\hat{\sigma}_L(\lambda_1)\hat{\sigma}_L(\lambda_2)} \{\sigma_a(\lambda_1)\sigma_a(\lambda_2)\rho_{aa}(\lambda_1, \lambda_2)\mu_L(\lambda_1)\mu_L(\lambda_2) \\ &\quad + \sigma_a(\lambda_1)\sigma_b(\lambda_2)\rho_{ab}(\lambda_1, \lambda_2)\mu_L(\lambda_1) + \sigma_a(\lambda_2)\sigma_b(\lambda_1)\rho_{ab}(\lambda_2, \lambda_1)\mu_L(\lambda_2) \\ &\quad + \sigma_b(\lambda_1)\sigma_b(\lambda_2)\rho_{bb}(\lambda_1, \lambda_2)\}, \end{aligned}$$

where $E[\]$ denotes the expectation operator. The cross-correlations between $a(\lambda)$ and $b(\lambda)$ over λ_1 and λ_2 are $\rho_{aa}(\lambda_1, \lambda_2)$, $\rho_{ab}(\lambda_1, \lambda_2)$, $\rho_{ab}(\lambda_2, \lambda_1)$, and $\rho_{bb}(\lambda_1, \lambda_2)$. Notice how the measured correla-

tion is written as a decorrelation factor times the actual environment correlation $\rho_L(\lambda_1, \lambda_2)$ plus a correlation bias term. Further analysis on measured statistics can be found in Appendix B.

5.2 NOISE

5.2.1 Effects on Measurements

Noise in the interferogram signal from the FTS will result in a variance in the measured spectral radiance for a given spectral band. Theoretically this noise variance could be correlated band to band. For the Bomem FTS, however, the interferogram noise is nearly white for each detector and is therefore uncorrelated between wavelength bands in the spectrum.

In the case of contrast measurements, sensor noise will limit the mean target to background contrast that can be measured. Noise is modeled here as a zero mean offset error $b(\lambda)$, uncorrelated between spectral bands (i.e., $\rho_{bb}(\lambda_1, \lambda_2) = 0$) with variance $\sigma_n^2(\lambda)$. The minimum detectable mean contrast will be:

$$\mu_{\Delta L}^{MIN}(\lambda) = \sqrt{2} \cdot \sigma_n(\lambda). \quad (5-5)$$

In the case of correlation measurements, sensor noise will cause decorrelation. In practice, this will reduce the measured correlation, or limit the correlation which can ultimately be measured by the sensor. The sensor limited correlation, determined by substituting the noise variance into EQ 5-4 with $\sigma_a(\lambda) = 0$, $\rho_{aa}(\lambda_1, \lambda_2) = 0$, $\rho_{ab}(\lambda_1, \lambda_2) = 0$, and $\rho_L(\lambda_1, \lambda_2) = 1$, is given by:

$$\hat{\rho}_L(\lambda_1, \lambda_2)_{max} = \frac{1}{\sqrt{\left(1 + \frac{\sigma_n^2(\lambda_1)}{\sigma_L^2(\lambda_1)}\right) \left(1 + \frac{\sigma_n^2(\lambda_2)}{\sigma_L^2(\lambda_2)}\right)}} \quad (5-6)$$

where $\sigma_L^2(\lambda)$ is the background clutter variance (also in spectral radiance units).

5.2.2 Anticipated Noise Effects

For the Bomem FTS, the noise is given by:

$$\sigma_n(\lambda) = \frac{NESR}{\sqrt{N_s N_\lambda}} \quad (5-7)$$

where N_s is the number of integrated scans, N_λ is the number of integrated spectral bins, and $NESR$ is the noise equivalent spectral radiance of the sensor. The sensor $NESR$ is a function of the detector, the spectral resolution of the instrument, and the type of apodization utilized in the transform of the interferogram. The measured $NESR$ for a 25C blackbody source at 8 cm^{-1} spectral resolution is given in Section 4.1. Table 5-1, shown below, provides computed noise levels based on the measured $NESR$. Each bandwidth is approximately 100nm, produced from an integer number of 8 cm^{-1} resolution wavelength samples.

Table 5-1: Sensor Noise for $N_s=15$ Coadded Scans

Wavelength (microns)	Spectral Bandwidth (nm)	Required Spectral Binning N_λ	$NESR$ (μflicks)	σ_n (μflicks)
3.8	92.4	8	0.34 (InSb)	0.031
4.7	88.4	5	0.40 (InSb)	0.047
8.0	102.4	2	0.72 (MCT)	0.13
10.0	80.0	1	0.64 (MCT)	0.17
12.0	115.2	1	0.63 (MCT)	0.16

Figure 5-1 shows the computed minimum detectable contrast (EQ 5-5) as a function of the number of coadded scans. The assumed spectral bandwidths are given in Table 5-1. These results show that the anticipated FTS minimum detectable contrast is less than $0.25\ \mu\text{flicks}$ ($\mu\text{W}/\text{cm}^2/\text{sr}/\mu\text{m}$) for bands in the LWIR (8.0 - 12.0 μm), with 15 or more coadded scans. For bands in the MWIR (3.0 - 5.0 μm), the minimum detectable contrast is less than $0.07\ \mu\text{flicks}$ with 15 or more co-added scans.

Estimates of the effect of sensor noise on band-to-band correlation measurements require specification of the background clutter level. The clutter radiance variance per temperature variance is given approximately by:

$$\frac{\sigma_L(\lambda)}{\sigma_T} = \frac{dL(\lambda)}{dT} = \frac{hc}{\lambda k T^2} L(\lambda). \quad (5-8)$$

This relationship can be used with EQ 5-6 to estimate the noise limited maximum band-to-band correlation as a function of the temperature clutter level σ_T . Maximum equivalent clutter suppression levels (in dB) can be computed from the maximum band-to-band correlation by:

$$\Upsilon_{max} (dB) = 10 \cdot \log \left[\frac{1}{1 - (\hat{\rho}_L(\lambda_1, \lambda_2)_{max})^2} \right] \quad (5-9)$$

Equivalent clutter suppression provides a convenient logarithmic form in which to display correlation results. Table 5-2 relates clutter suppression and correlation.

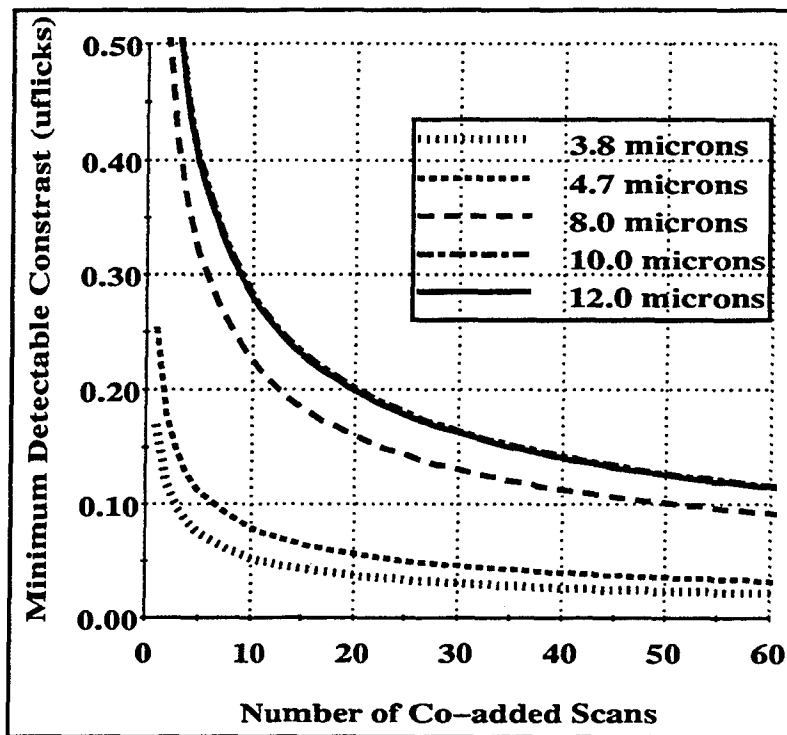


Figure 5-1. Minimum Detectable Contrast (μ flicks) vs. Number of Coadded Scans.

Figure 5-2 provides the maximum equivalent clutter suppression as a function of number of coadded scans for an assumed background clutter level (σ_T) of 1K and mean background temperature of 300K with an assumed emissivity of unity. These results show the sensor noise limited band-to-band correlations to be in excess of 0.9997 (32dB) for a variety of band pairs, with 15 or more coadded scans and a 1K clutter level. Both the (4.7 μ m, 10.0 μ m) and (8.0 μ m, 10.0 μ m) band pairs provide nearly equal results and are thus difficult to differentiate in Figure 5-2.

Table 5-2: Correlation vs. Equivalent Clutter Suppression

Band-to-Band Correlation	Equivalent Clutter Suppression Level (dB)
0.9	7
0.97	12
0.99	17
0.997	22
0.999	27
0.9997	32
0.9999	37
0.99997	42
0.99999	47

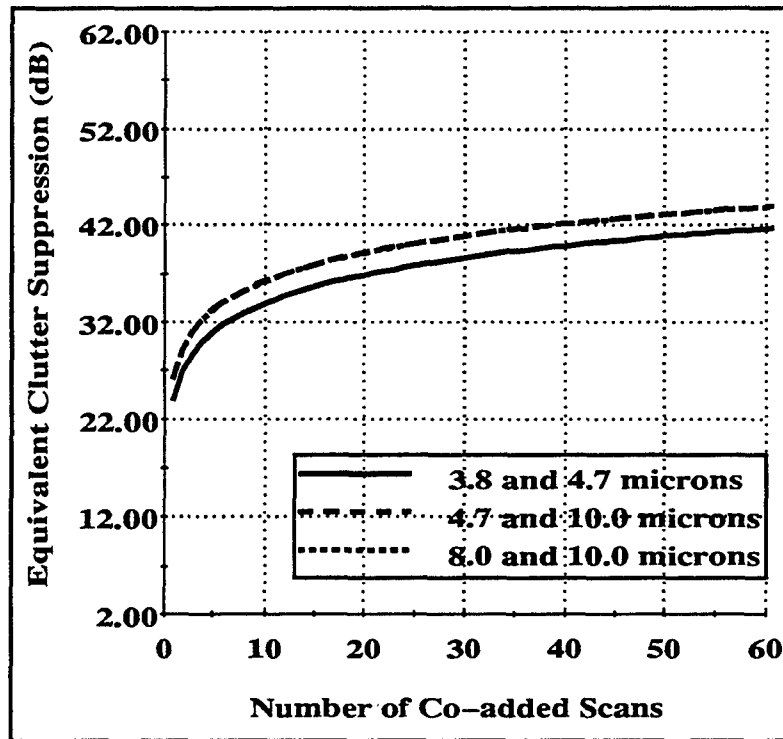


Figure 5-2. Maximum Equivalent Clutter Suppression (dB) vs. Number of Coadded Scans.

Figures 5-3 and 5-4 provide maximum equivalent clutter suppression as a function of background clutter level (σ_T). Figure 5-3 provides the results for a total of 15 co-added scans and Figure 5-4 for 25 co-added scans. These results show that 15 to 25 co-added scans are sufficient to maintain sensor noise limited band-to-band correlations in excess of 0.9999 (37dB) for clutter levels of 1 K. Again, both the (4.7 μm , 10.0 μm) and (8.0 μm , 10.0 μm) band pairs provide nearly equal results and are thus difficult to differentiate in Figures 5-3 and 5-4.

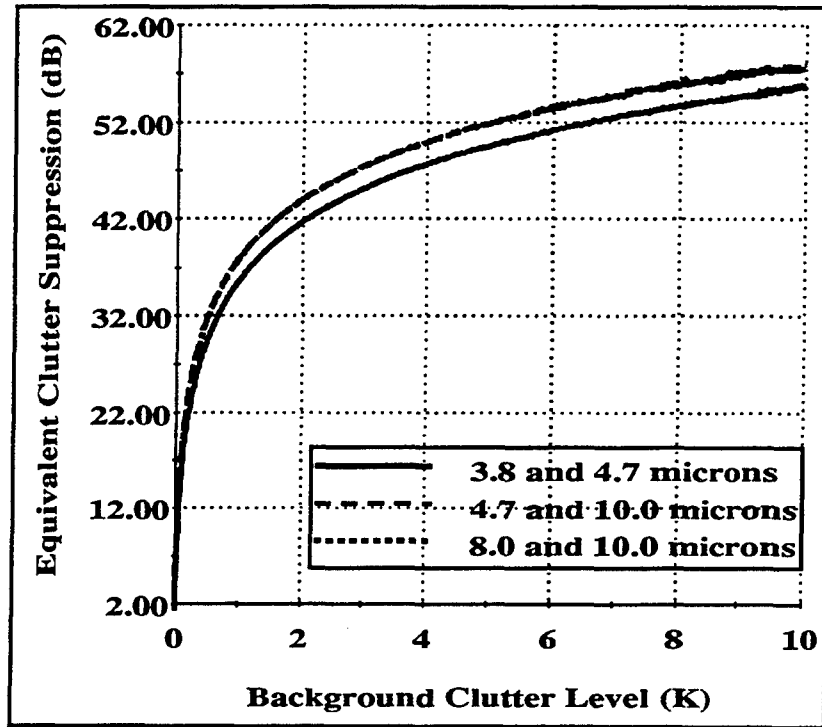


Figure 5-3. Maximum Equivalent Clutter Suppression (300K Target, $N_s=15$) vs. Background Clutter Level (σ_T).

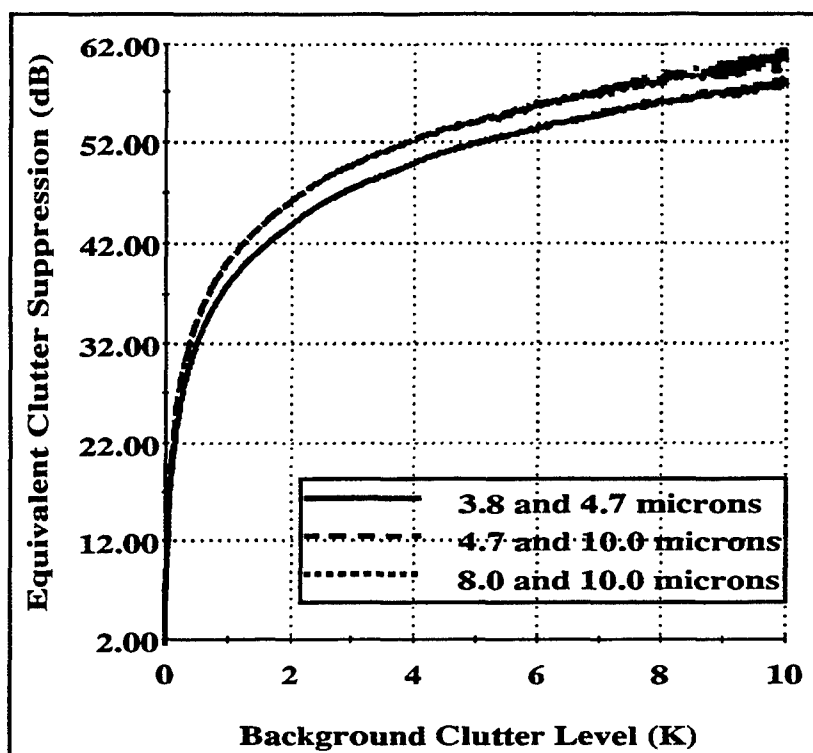


Figure 5-4. Maximum Equivalent Clutter Suppression (300K Target, $N_s=25$) vs. Background Clutter Level (σ_T).

5.3 ABSOLUTE CALIBRATION ACCURACY

5.3.1 Effects on Measurements

The target detection algorithms being considered are primarily interested in spectral radiance differences between the target and the background. For this reason, absolute calibration accuracy is of lesser importance than relative calibration accuracy. Absolute calibration errors will not affect measured target/background contrast or background correlation levels (see Appendix B). Nevertheless, absolute calibration accuracy will be analyzed as it does affect model validation and other potential uses of the data.

The absolute calibration accuracy will be determined by the characteristics of the calibration sources. Specifically, the absolute temperature uncertainty dT and the emissivity uncertainty $d\epsilon$. The uncertainty in a radiance measurement is shown in Appendix B to be:

$$d\mu_L(\lambda) = da \cdot \mu_L(\lambda) + db \quad (5-10)$$

where da and db are the uncertainties in the calibration gain and offset coefficients given by:

$$da = \frac{1}{\sqrt{2}} \cdot \frac{1}{L_H - L_C} \left(\frac{hc}{\lambda k T_H^2} L_H + \frac{hc}{\lambda k T_C^2} L_C \right) dT + \frac{1}{\sqrt{2}} \cdot \frac{L_H + L_C}{L_H - L_C} \cdot \frac{d\epsilon}{\epsilon}, \quad (5-11)$$

$$\text{and } db = \frac{1}{\sqrt{2}} \cdot \frac{L_H \cdot L_C}{L_H - L_C} \left(\frac{hc}{\lambda k T_H^2} + \frac{hc}{\lambda k T_C^2} \right) dT + \frac{L_H \cdot L_C}{L_H - L_C} \cdot \frac{d\epsilon}{\epsilon}. \quad (5-12)$$

Here T_H and T_C are the hot and cold calibration source temperatures and L_H and L_C are the resulting spectral radiances at the wavelength of interest. The blackbody calibration source emissivity is specified by ϵ .

5.3.2 Anticipated Accuracy Levels

As an example, the anticipated absolute calibration accuracies were computed for five representative wavelengths and a 300K blackbody target. The assumption is that two-point calibration is performed with 20 C and 45 C calibration source temperatures. This range in calibration source temperature is reasonable for calibrating mid-day summer target and background radiance measurements. The calibration sources are reported by the manufacturer to at least meet the following specifications: $dT = 0.03$ K, $d\epsilon = 0.01$, and $\epsilon = 0.99$. The results are given in Table 5-3 below. It is seen that we anticipate, based on the manufacturer specifications, roughly 3-8% absolute radiometric calibration accuracy. In fact, the measured absolute radiometric calibration accuracy far exceeds these levels and was found to be about 1% (Section 4.2). This indicates that the blackbody sources performed better than the manufacturer specifications.

Table 5-3: Anticipated Absolute Calibration Accuracies (Based on the Blackbody Source Manufacturer's Specifications)

Wavelength (microns)	L_C (μ flicks)	L_H (μ flicks)	da	db (μ flicks)	μ_L (μ flicks)	$(d\mu_L/\mu_L)$ x 100 (%)
3.8	36.72	101.42	0.0170	0.681	49.65	3.07
4.7	150.67	342.58	0.0201	3.093	192.27	3.62
8.0	786.47	1275.96	0.0318	22.393	907.88	5.65
10.0	884.21	1305.37	0.0388	29.484	992.45	6.85
12.0	813.18	1129.04	0.0456	30.953	896.17	8.01

5.4 RELATIVE CALIBRATION ACCURACY

5.4.1 Effects on Measurements

Relative calibration of the instrument will either be of great or only of moderate concern depending on how the spectral contrast and correlation measurements are taken. If enough measurements can be made within a calibration cycle for a given correlation or contrast estimate, then relative calibration accuracy is not a concern. Rather, it will only affect the absolute spectral radiance measurements in the manner described in Section 5.3.

Relative calibration will be an important issue, however, if it is required to utilize data taken in different calibration cycles to make contrast or correlation measurements. Since it is unlikely (although possible) that the emissivity of the calibration sources will change in time, errors will be caused primarily by the temperature instability of the calibration sources.

If the calibration sources exhibit a temperature variance σ_{CAL}^2 , then the resulting sensor gain σ_a^2 and offset σ_b^2 variances are given by (See Appendix B or EQ 5-11 and EQ 5-12):

$$\sigma_a = \frac{1}{\sqrt{2}} \cdot \frac{1}{L_H - L_C} \left(\frac{hc}{\lambda k T_H^2} L_H + \frac{hc}{\lambda k T_C^2} L_C \right) \sigma_{CAL} \quad (5-13)$$

$$\text{and } \sigma_b = \frac{1}{\sqrt{2}} \cdot \frac{L_H \cdot L_C}{L_H - L_C} \left(\frac{hc}{\lambda k T_H^2} + \frac{hc}{\lambda k T_C^2} \right) \sigma_{CAL}. \quad (5-14)$$

In the case of measurements made over several calibration cycles, we will treat these uncertainties as an rms error over the measurements. The contrast measurement limitations are then given by:

$$\sigma_{\mu_{\Delta L}}(\lambda) = \sqrt{2} (\sigma_a \mu_L(\lambda) + \sigma_b). \quad (5-15)$$

In the case of correlation, it is insufficient to know only the variance of the introduced errors at any wavelength. It is also necessary to know the auto- and cross-correlation of the gain and offset errors between bands of interest. Based on the gain and offset error expressions given in Appendix B, we see that the errors will be completely correlated band to band and with each other. The correlation limit, based on EQ 5-4, reduces to:

$$\hat{\rho}_L(\lambda_1, \lambda_2)_{max} = \frac{\sigma_L(\lambda_1)\sigma_L(\lambda_2)}{\hat{\sigma}_L(\lambda_1)\hat{\sigma}_L(\lambda_2)} (1 + \sigma_a(\lambda_1)\sigma_a(\lambda_2)) \quad (5-16)$$

$$+ \frac{\sigma_a(\lambda_1)\sigma_a(\lambda_2)\mu_L(\lambda_1)\mu_L(\lambda_2) + \sigma_a(\lambda_1)\mu_L(\lambda_1)\sigma_b(\lambda_2) + \sigma_a(\lambda_2)\mu_L(\lambda_2)\sigma_b(\lambda_1) + \sigma_b(\lambda_1)\sigma_b(\lambda_2)}{\hat{\sigma}_L(\lambda_1)\hat{\sigma}_L(\lambda_2)}$$

where

$$\hat{\sigma}_L(\lambda) = \sqrt{\sigma_L^2(\lambda) [1 + \sigma_a^2(\lambda)] + (\sigma_a(\lambda)\mu_L(\lambda) + \sigma_b(\lambda))^2}. \quad (5-17)$$

This maximum correlation limit assumes that the environmentally limited background correlation is unity (i.e., $\rho_L(\lambda_1, \lambda_2) = 1.0$).

5.4.2 Anticipated Accuracy Levels

The temperature instability (σ_{CAL}) of the blackbody sources is anticipated to be less than 0.03 K (based on the manufacturer's specifications), resulting in the anticipated relative calibration accuracies for mean contrast given in Table 5-4. Again, the assumption is that two-point calibration is performed with 20 C and 45 C calibration source temperatures and that target and background temperatures are 300K. A relative calibration accuracy of better than 0.40% is anticipated.

Table 5-4: Anticipated Relative Calibration Accuracies for Mean Contrast Measurements (Based on the Blackbody Source Manufacturer's Specifications)

Wavelength (microns)	L_C (μ flicks)	L_H (μ flicks)	σ_a	σ_b (μ flicks)	μ_L (μ flicks)	$\left(\frac{\sigma_{\mu_{\Delta L}}}{\mu_L}\right) \times 100$ (%)
3.8	36.72	101.42	0.00178	0.0996	49.65	0.38
4.7	150.67	342.58	0.00174	0.3762	192.27	0.37
8.0	786.47	1275.96	0.00170	1.6845	907.88	0.36
10.0	884.21	1305.37	0.00168	1.8015	992.45	0.35
12.0	813.18	1129.04	0.00166	1.5922	896.17	0.34

Figure 5-5 provides the calibration error limited maximum equivalent clutter suppression as a function of source temperature instability (σ_{CAL}) and spectral band combinations. It is assumed

that the environmentally limited background correlation is unity and that the clutter variance (σ_T) is 1K. These results show that for the anticipated instability (i.e., $\sigma_{CAL} < 0.03K$), the effect of relative calibration error over several calibration cycles is significant. The (3.8 μ m, 4.7 μ m) band pair provides calibration error limited correlations in excess of 0.9999 (37dB) for source temperature instabilities less than 0.03K. However, the two remaining band pairs, (4.7 μ m, 10.0 μ m) and (8.0 μ m, 10.0 μ m), suffer significant clutter suppression loss due to relative calibration error across several calibration cycles. The 8.0 and 10.0 μ m band pair only provides a calibration error limited correlation of 0.999 (27dB) at $\sigma_{CAL}=0.03K$. The 4.7 and 10.0 μ m band pair's performance is limited to about 0.995 (20dB) at $\sigma_{CAL}=0.03K$. These results suggest that environment limited background correlation measurements may not be possible if the data must be collected across multiple calibration cycles. The effect of calibration error across multiple calibration cycles can be reduced if the source temperature differences are increased. However, this is not expected to sufficiently compensate for the relative calibration error and it also potentially introduces additional absolute calibration error. Thus, all background correlation measurements should be made within a single calibration cycle. Again, it should be noted that decorrelation due to source instability is not a factor when the correlation measurements can be made within a single calibration cycle.

Figures 5-6 and 5-7 provide the decorrelation gain factor and correlation bias as a function of source temperature instability. Thus, the anticipated measured correlations can be computed for any environment correlation level using these two plots. Notice that the correlation bias increases towards unity as σ_{CAL} increases. For very large temperature instabilities the measured correlation will essentially be that of the calibration sources and not the environment.

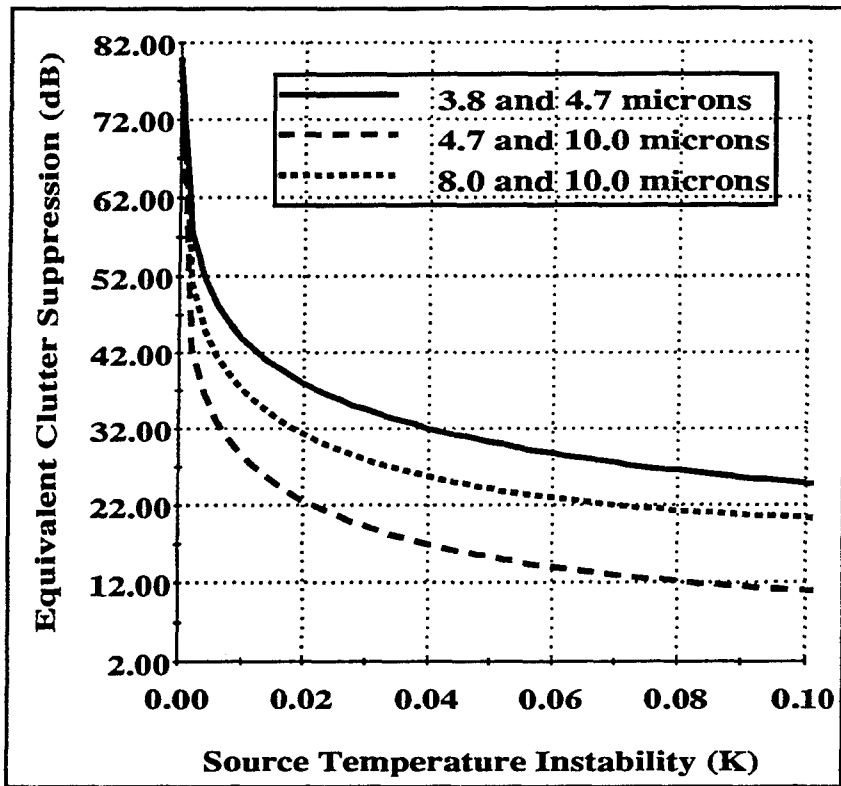


Figure 5-5. Maximum Equivalent Clutter Suppression vs. Source Temperature Instability σ_{CAL} (300K Target, 45C and 20C Calibration Points, $\sigma_T = 1.0K$).

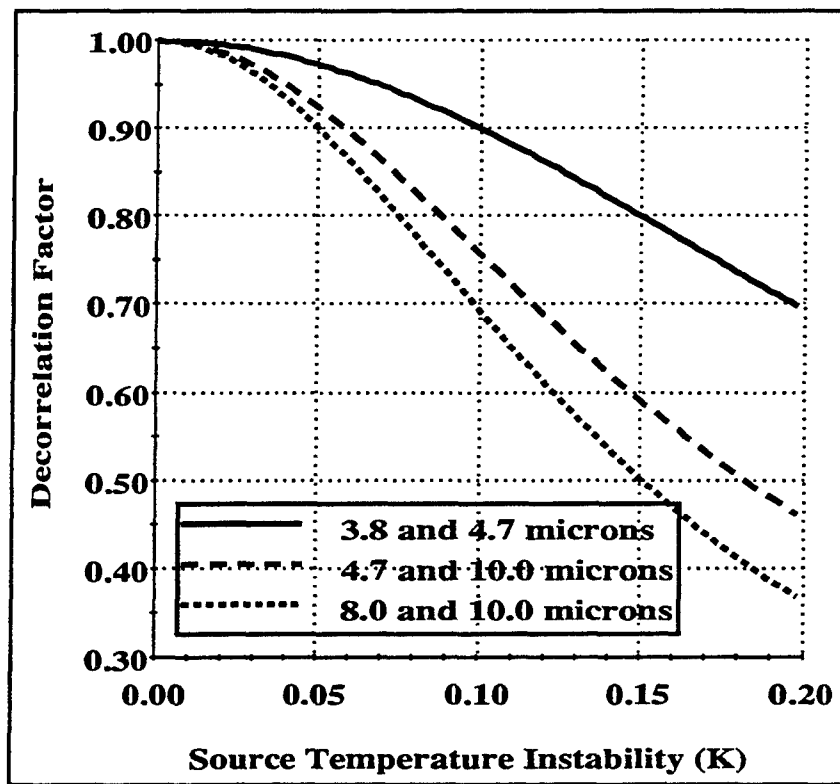


Figure 5-6. Decorrelation Factor vs. Source Temperature Instability σ_{CAL} (300K Target, 45C and 20C Calibration Points, $\sigma_T = 1.0K$).

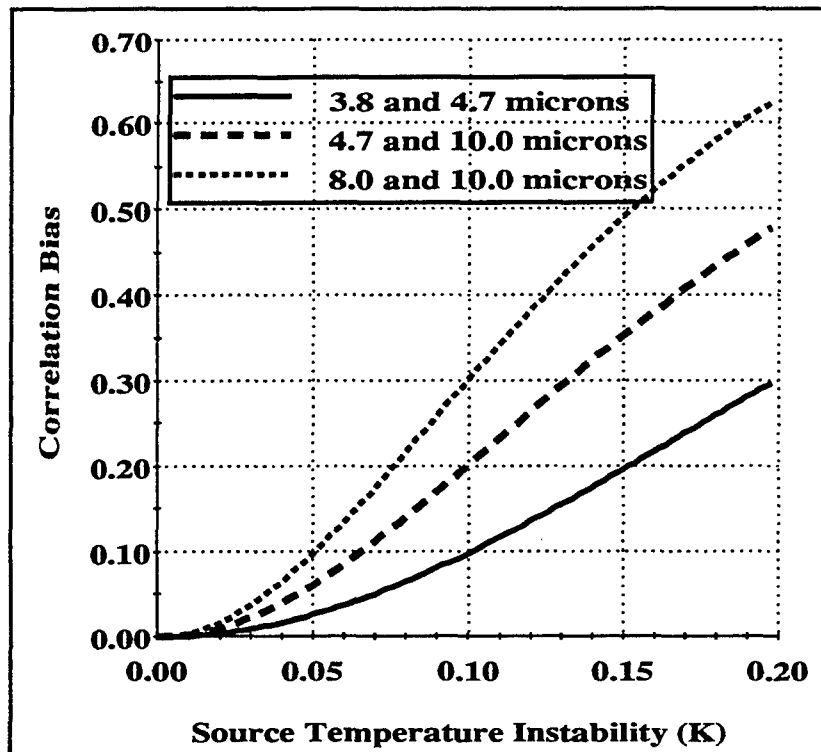


Figure 5-7. Correlation Bias vs. Source Temperature Instability σ_{CAL} (300K Target, 45C and 20C Calibration Points, $\sigma_T = 1.0K$).

The previous correlation limits were computed assuming a background clutter level of 1K. The decorrelation due to relative calibration error is decreased with increasing clutter level due to a decrease in the relative magnitude of the source temperature instability compared to the clutter. Figure 5-8 provides the maximum equivalent clutter suppression, assuming an environment correlation of unity, as a function of the clutter level. These results show that higher correlations can be measured when the clutter levels are high. However, remember that the relative calibration error decorrelation factor will still prohibit environment limit correlation measurements. Also, actual clutter levels near or below 1K are not uncommon, supporting the premise that background correlation measurements should still not be made across multiple calibration cycles.

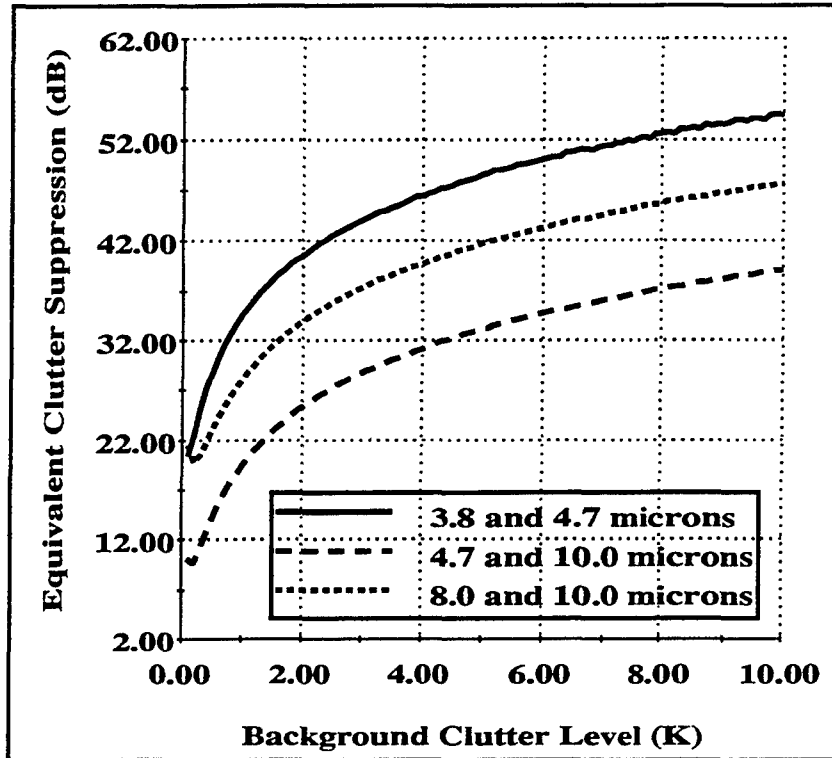


Figure 5-8. Maximum Equivalent Clutter Suppression vs. Clutter Level σ_T (300K Target, 45C and 20C Calibration Points, $\sigma_{CAL} = 0.03$ K).

5.5 SENSOR STABILITY

5.5.1 Effects on Measurements

Within a calibration cycle, the relative accuracy of radiometric measurements will be limited by the temporal stability of the sensor. FTS sensor instability can be due to temporally varying stray radiances (either external or internal), detector instability, and electronics instability. A temporal calibration procedure can be used to remove the linear component of this instability. Sensor characterization measurements have shown the average sensor instability to be 40 to 70 mK prior to temporal calibration and 15 to 20 mK after temporal calibration (See Section 4.4). The residual 15 to 20 mK instability is limited by the blackbody calibration source instability and is near the sensor noise. It is this residual instability (15-20mK) which can degrade sensor mean contrast and band-to-band correlation measurement performance.

We can model this residual instability as a signal dependent bias error which can effectively increase the variance of the measured signature. The bias error has an rms level of:

$$\sigma_b(\lambda) = \frac{dL(\lambda)}{dT} \sigma_{INS}(t) \approx \frac{hc}{\lambda kT^2} L(\lambda) \sigma_{INS}(t) \quad (5-18)$$

where $\sigma_{INS}(t)$ is the residual temperature instability over the measurement time t . This residual instability can increase due to linear signal drifts as the collection time increases.

The error introduced in a mean contrast estimate made from single target and background measurements collected during the time interval t is then given by:

$$\sigma_{\mu_{\Delta L}}(\lambda) = \sigma_b(\lambda). \quad (5-19)$$

For band-to-band correlation measurements, EQ 5-4 is once again used but with $\sigma_a(\lambda)=0$ and $\sigma_b(\lambda)$ as given above. In this case EQ 5-4 reduces to:

$$\hat{\rho}_L(\lambda_1, \lambda_2)_{max} = \frac{1}{\sqrt{(\sigma_L^2(\lambda_1) + \sigma_b(\lambda_1)) (\sigma_L^2(\lambda_2) + \sigma_b(\lambda_2))}} (\sigma_L(\lambda_1) \sigma_L(\lambda_2) \rho_L(\lambda_1, \lambda_2) + \sigma_b(\lambda_1) \sigma_b(\lambda_2) \rho_{bb}(\lambda_1, \lambda_2)). \quad (5-20)$$

The instability cross-correlation $\rho_{bb}(\lambda_1, \lambda_2)$ will be studied parametrically since it is possible to have both positive and negatively correlated drifts. Temporal instability measurements of the FTS sensor have shown drifts between the InSb and MCT detector channels to sometimes be anti-correlated (negative).

5.5.2 Anticipated Accuracy Levels

In the case of mean measurements, Table 5-5 provides the anticipated error levels for both uncorrected sensor instabilities ($\sigma_{INS} = 70\text{mK}$) and corrected residual (nonlinear) instabilities ($\sigma_{INS} = 20\text{mK}$). For an assumed 300K blackbody target, the mean signal error is expected to be less than 0.085% of the total signal for all wavelengths.

For band-to-band correlation measurements, the sensor stability limited maximum correlation (or equivalent clutter suppression) is a strong function of the instability correlation (i.e., $\rho_{bb}(\lambda_1, \lambda_2)$) between bands. Within a detector band (i.e., the MWIR (InSb) or LWIR (MCT)), one would expect the sensor drifts causing instability to be correlated between bands since the same detector and associated electronics are used. However, it is possible for a highly spectral stray radiance source to decorrelate the single-detector band-to-band drifts. The lower limit is expected to be zero correlation (i.e., $\rho_{bb}(\lambda_1, \lambda_2) = 0$). For sensor band pairs across detectors (i.e., MWIR/LWIR

band pairs), it is possible for the instability drifts to be negatively correlated (anti-correlated) due to differences in detectors and electronics. Figure 5-9 displays maximum equivalent clutter suppression, limited by sensor stability, as a function of instability correlation for the MWIR/LWIR band pair shown. It was assumed that the background had a physical temperature of 300K, a clutter level of 1K (σ_T), and that the residual sensor instability, after temporal calibration, was 20mK. These results show that, for these typical background and sensor parameter levels, the maximum stability limited correlation is below 0.9997 (32dB) for MWIR/LWIR drift correlations less than 0.25 and can be as poor as 0.999 (27dB) for pure anti-correlated drifts (i.e., $\rho_{bb}(\lambda_1, \lambda_2) = -1$).

Table 5-5: Anticipated Instability Mean Contrast Error Levels (Assuming a 300K Target)

Wavelength (microns)	L(λ) (μ flicks)	Pre-Temporal Calibration Mean Signal Errors		Post-Temporal Calibration Mean Signal Errors	
		$\sigma_b(\lambda)$ for $\sigma_{INS}=$ 70mK (μ flicks)	Signal Error (%)	$\sigma_b(\lambda)$ for $\sigma_{INS}=$ 20mK (μ flicks)	Signal Error (%)
3.8	49.65	0.146	0.294	0.042	0.084
4.7	192.27	0.458	0.238	0.131	0.068
8.0	907.88	1.270	0.140	0.363	0.040
10.0	992.45	1.111	0.112	0.317	0.032
12.0	896.17	0.836	0.093	0.239	0.027

Figure 5-10 shows that, for an assumed instability correlation of 0.0 (i.e., $\rho_{bb}(\lambda_1, \lambda_2) = 0$), the anticipated residual instability level of 15 to 20mK is sufficiently low to maintain correlations in excess of 0.9997 (32dB) for various band pairs, assuming a 1K (σ_T) clutter level. This result is practically independent of band pair because the instability is given as a wavelength independent temperature instability and because the instability correlations were assumed to be zero for all band pairs. An increase in the true clutter level (σ_T), with respect to the residual instability, can dramatically increase the stability limited correlation performance, as shown in Figure 5-11.

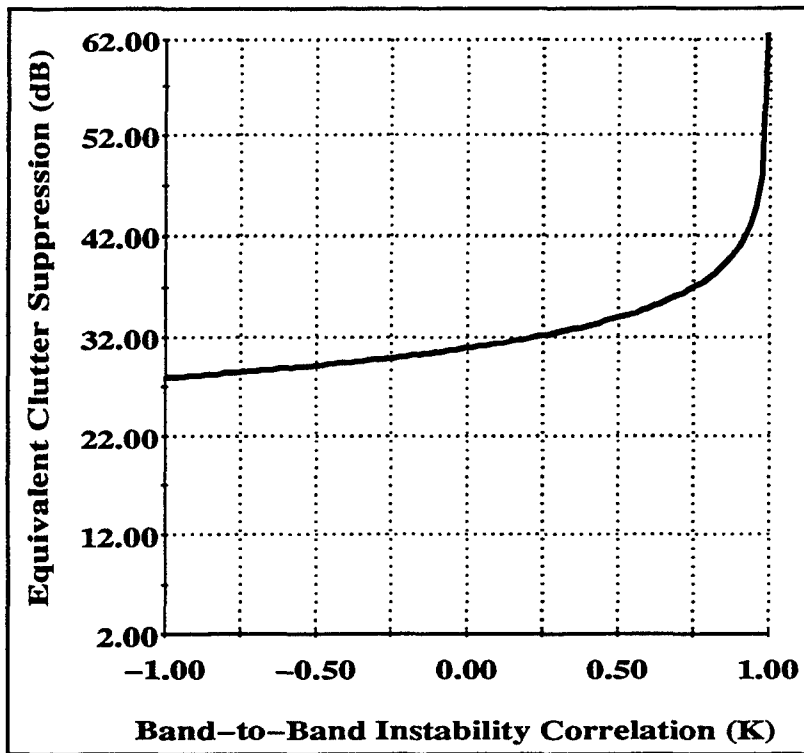


Figure 5-9. Maximum Equivalent Clutter Suppression vs. $\rho_{bb}(\lambda_1, \lambda_2)$ for $\lambda_1 = 4.7\mu\text{m}$ and $\lambda_2 = 10.0\mu\text{m}$ (Assuming $\sigma_{\text{INS}} = 0.02\text{K}$, $\sigma_{\text{T}} = 1\text{K}$, and a 300K Background).

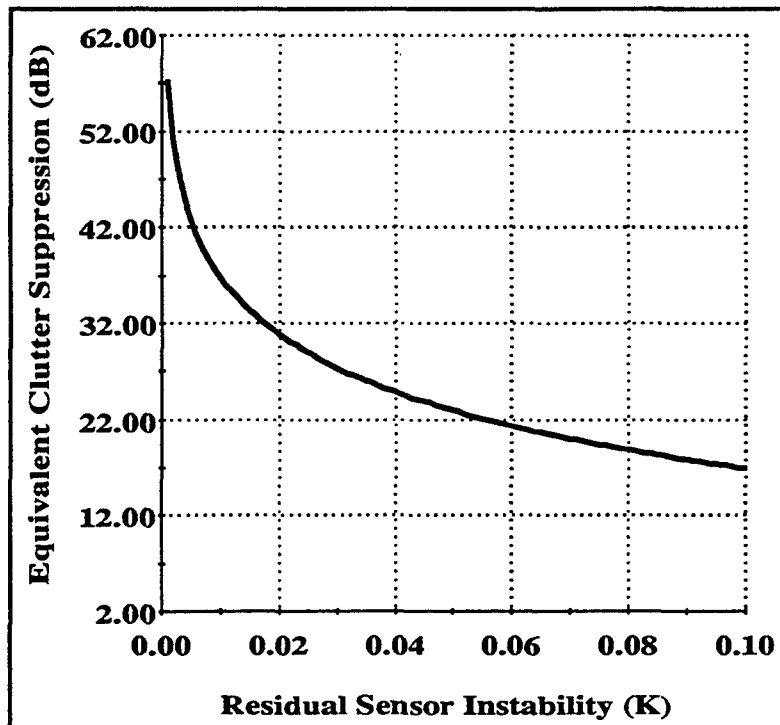


Figure 5-10. Maximum Equivalent Clutter Suppression vs. σ_{INS} for Various Band Combinations ((3.8 μm ,4.7 μm), (4.7 μm ,10.0 μm), and (8.0 μm ,10.0 μm)) (Assuming $\sigma_{\text{T}} = 1\text{K}$, $\rho_{bb}(\lambda_1, \lambda_2) = 0.0$, and a 300K Background).

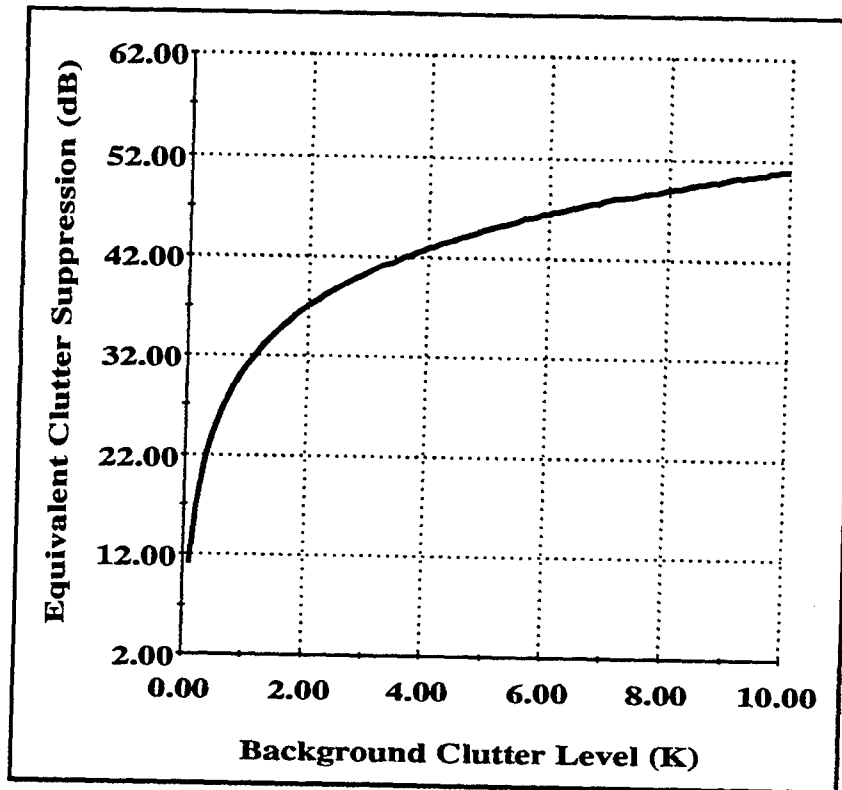


Figure 5-11. Maximum Equivalent Clutter Suppression vs. Background Clutter Level (σ_T) for Various Band Combinations ((3.8 μm ,4.7 μm), (4.7 μm ,10.0 μm), and (8.0 μm ,10.0 μm)) (Assuming $\sigma_{\text{INS}} = 0.02\text{K}$, $\rho_{\text{bb}}(\lambda_1, \lambda_2) = 0.0$, and a 300K Background).

5.6 RESPONSE LINEARITY

5.6.1 Effects on Measurements

Nonlinearity in the case of a Fourier transform spectrometer is very complicated to analyze because the nonlinearity will manifest itself in the detected interferogram rather than the corresponding spectrum. The result of nonlinearity in the spectral domain, therefore, will be very dependent on the spectrum itself. A first order effect is a corresponding nonlinearization in the spectral domain which we will analyze here and measure in the course of the sensor characterization experiments. Second order effects could be harmonics and crosstalk in the spectral domain. We anticipate that these will be extremely small effects, but it is difficult to rigorously evaluate the magnitude of these effects and the resulting limitations to contrast and correlation measurements. Nonlinearity in the spectrum will not be a significant factor in the case of contrast measurements because the introduced error will always be a small fraction of the mean difference.

In the case of correlation measurements, however, uncorrected nonlinearity can result in a spectral decorrelation. We can treat this nonlinearity as a difference between the estimated and true spectral radiances over the ensemble of measurements (i.e., an offset error, albeit signal dependent). The correlation limit will depend on both the variance and correlation of this error, given by:

$$\sigma_b^2(\lambda) = E[(\hat{L}_i(\lambda) - L(\lambda))^2] - (E[\hat{L}_i(\lambda) - L(\lambda)])^2 \quad (5-21)$$

$$\rho_{bb}(\lambda_1, \lambda_2) = \frac{E[(\hat{L}_i(\lambda_1) - L(\lambda_1))(\hat{L}_i(\lambda_2) - L(\lambda_2))]}{\sigma_b(\lambda_1)\sigma_b(\lambda_2)}. \quad (5-22)$$

5.6.2 Anticipated Level

Based on linearity specifications for the InSb detector and ambient radiance levels, we expect nonlinearities to be below 0.1% over a 10C clutter variance. A similar result might be expected for the MCT detector. For MWIR/MWIR and LWIR/LWIR band combinations, we further expect the nonlinearity to be highly correlated such that it will have a negligible effect on correlations. Decorrelations will only occur due to differences in nonlinearity across wavelengths. The wavelength dependent difference in nonlinearity is expected to be very small for band combinations contained within the spectral range of a single detector. For MWIR/LWIR band pairs across both detectors, the correlation may be somewhat lower due to potentially larger wavelength dependent differences in nonlinearity. However, it is still not expected to be a limiting factor.

5.7 POLARIZATION SENSITIVITY

5.7.1 Effects on Measurements

If the sensor exhibits a polarimetric response, then variations in the polarization of the scene will show up as variations in radiance. Assume that the sensor exhibits a different throughput for the V and H polarizations ($\tau_V(\lambda)$ and $\tau_H(\lambda)$). Similarly, assume that the scene spectral radiance is different for the V and H polarizations ($L_V(\lambda)$ and $L_H(\lambda)$). The spectral radiance measurement is then given by:

$$\hat{L}(\lambda) = L_V(\lambda)\tau_V(\lambda) + L_H(\lambda)\tau_H(\lambda) \quad (5-23)$$

The polarization characteristics of the sensor can be stated as a degree of polarization $\beta(\lambda)$, given as:

$$\beta(\lambda) = \frac{\tau_V(\lambda) - \tau_H(\lambda)}{\tau_V(\lambda) + \tau_H(\lambda)}. \quad (5-24)$$

Similarly, the scene polarization can also be stated as a degree of polarization $\alpha(\lambda)$, given as:

$$\alpha(\lambda) = \frac{L_V(\lambda) - L_H(\lambda)}{L_V(\lambda) + L_H(\lambda)}, \quad (5-25)$$

where $\alpha(\lambda) = 1$ corresponds to a V-polarized scene, $\alpha(\lambda) = -1$ corresponds to an H-polarized scene, and $\alpha(\lambda) = 0$ corresponds to an unpolarized scene.

Given these definitions, we can write the total scene radiance $L(\lambda)$ as the sum of the two polarized components:

$$L(\lambda) = L_V(\lambda) + L_H(\lambda), \quad (5-26)$$

where

$$L_V(\lambda) = \frac{1}{2}(1 + \alpha(\lambda))L(\lambda) \quad (5-27)$$

$$\text{and } L_H(\lambda) = \frac{1}{2}(1 - \alpha(\lambda))L(\lambda). \quad (5-28)$$

The sensor measured scene radiance can then be written as:

$$\begin{aligned} \hat{L}(\lambda) &= (1 + \beta(\lambda))L_V(\lambda) + (1 - \beta(\lambda))L_H(\lambda) \\ &= (1 + \alpha(\lambda)\beta(\lambda))L(\lambda). \end{aligned} \quad (5-29)$$

Notice that when the degree of polarization of the sensor is zero (i.e., $\beta(\lambda) = 0$), the sensor is invariant to scene polarization and $\hat{L}(\lambda) = L(\lambda)$.

In the case of mean contrast measurements, the sensor's polarization sensitivity will exhibit itself as an additive error in the measured mean spectral radiance given by:

$$\hat{\mu}_L(\lambda) = \mu_L(\lambda) + \beta(\lambda)\mu_\alpha(\lambda)\mu_L(\lambda). \quad (5-30)$$

where $\mu_\alpha(\lambda)$ is the mean degree of scene polarization of the measurement ensemble and it is assumed that $\alpha(\lambda)$ and $L(\lambda)$ are uncorrelated.

When analyzing the case of correlation measurements, some assumptions on the scene statistics must be made. A possible worst case occurs when the scene's degree of polarization is uncorrelated band to band and uncorrelated with the single band radiances, although we still assume the band to band radiances to be correlated as $\rho_L(\lambda_1, \lambda_2)$. Given these assumptions, one can show that the polarization limited measured correlation is:

$$\hat{\rho}_L(\lambda_1, \lambda_2)_{max} = \frac{1}{\sqrt{\left(1 + \frac{\beta^2(\lambda_1)\sigma_\alpha^2(\lambda_1)\mu_{L}^2(\lambda_1)}{(1 + \beta(\lambda_1)\mu_\alpha(\lambda_1))^2\sigma_L^2(\lambda_1)}\right)\left(1 + \frac{\beta^2(\lambda_2)\sigma_\alpha^2(\lambda_2)\mu_{L}^2(\lambda_2)}{(1 + \beta(\lambda_2)\mu_\alpha(\lambda_2))^2\sigma_L^2(\lambda_2)}\right)}} \quad (5-31)$$

where $\sigma_\alpha^2(\lambda)$ is the variance of the degree of scene polarization and $\sigma_L^2(\lambda)$ is the background clutter variance.

5.7.2 Anticipated Accuracy Levels

When analyzing the effect of polarization sensitivity on mean contrast measurements, it is important to know the polarization properties of the targets and backgrounds of interest. One target coating of interest is the Army's current CARC 383 green camouflage paint. Limited bistatic reflectance measurements of this coating reveal some of its polarization properties.

Figure 5-12 displays the measured polarized BSDF (bi-static distribution function) $\rho'_{PP}(\lambda, \theta_p, \theta_r)$ at 10.6 μm for a transmitter angle of 60 degrees measured from the sample unit normal. The directional hemispherical reflectances are the integral of the full BRDF (bidirectional reflectance distribution function), which include the transmitter/receiver out-of-plane measurements. Unfortunately, only the in-plane BSDF at one transmitter angle was measured. Simple hemispheric integration of the single BSDF would generate an azimuthally independent specular annulus, which is not physically correct. For this reason, the directional hemispherical reflectances were approximated by integrating the BSDF about the specular lobe:

$$\rho_V(\lambda, \theta_r) = 2\pi \int_{(\theta_r - 30)}^{(\theta_r + 30)} (\rho'_{VV}(\lambda, \theta_p, \theta_r) + \rho'_{VH}(\lambda, \theta_p, \theta_r)) \cos\theta_i \sin\theta_i d\theta_i \quad (5-32)$$

$$\rho_H(\lambda, \theta_r) = 2\pi \int_{(\theta_r - 30)}^{(\theta_r + 30)} (\rho'_{HH}(\lambda, \theta_p, \theta_r) + \rho'_{HV}(\lambda, \theta_p, \theta_r)) \cos\theta_i \sin\theta_i d\theta_i \quad (5-33)$$

Based on the BSDFs of Figure 5-12, the computed directional hemispherical reflectances are:

$$\rho_V(10.6\mu\text{m}, 60.0^\circ) = 0.035 \quad (5-34)$$

$$\text{and } \rho_H(10.6\mu\text{m}, 60.0^\circ) = 0.198 \quad (5-35)$$

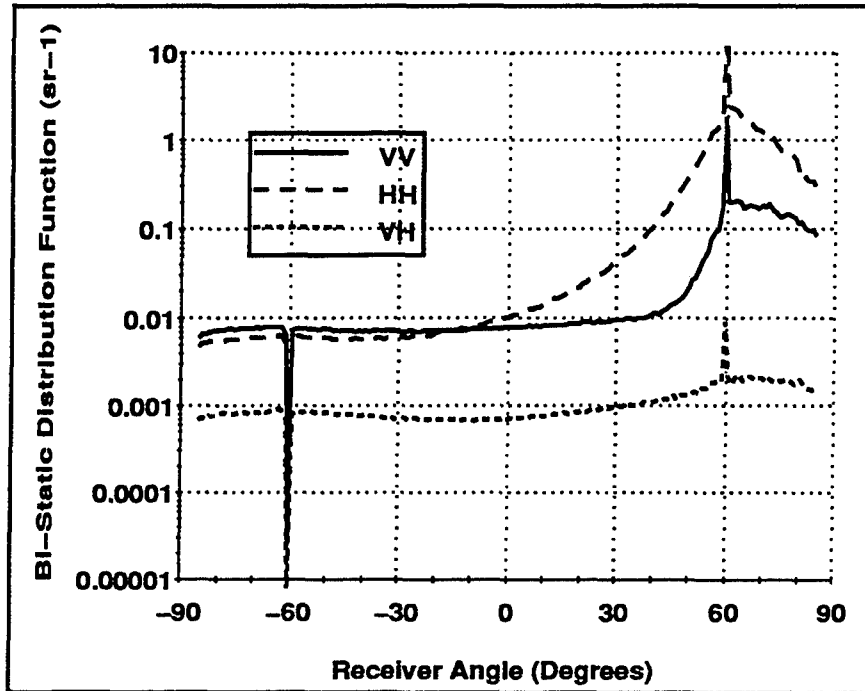


Figure 5-12. Measured BSDF for CARC 383 Green Paint ($\theta_i = 60$ degrees).

In order to study the effects of polarization sensitivity on mean contrast measurements it is necessary to set up a generic example. For this example, it is assumed that the target is coated with the CARC 383 green camouflage paint and has a temperature $T_{trg} = 300\text{K}$. The measured directional hemispherical spectral reflectance of CARC 383 green paint is shown in Figure 5-13. The background is assumed to be grass with a wavelength independent emissivity of 0.98 and a temperature equal to that of the target (i.e., $T_{bkg} = 300\text{K}$). The total radiance of the target and background includes both thermally emitted radiance and reflected sky radiance ($T_{sky} = 250\text{K}$) but ignores atmospheric path transmission and path radiance. The unpolarized total radiance can be written for both the target and background as:

$$L^{TOT}(\lambda) = (1 - \rho_D(\lambda)) L^{BB}(\lambda, T_{trg}) + \rho_D(\lambda) L^{BB}(\lambda, T_{sky}) \quad (5-36)$$

where $\rho_D(\lambda)$ is that of CARC 383 green paint for the target and is 0.02 for the grass background, and where L^{BB} is simply the Planck blackbody radiance for a given wavelength and temperature.

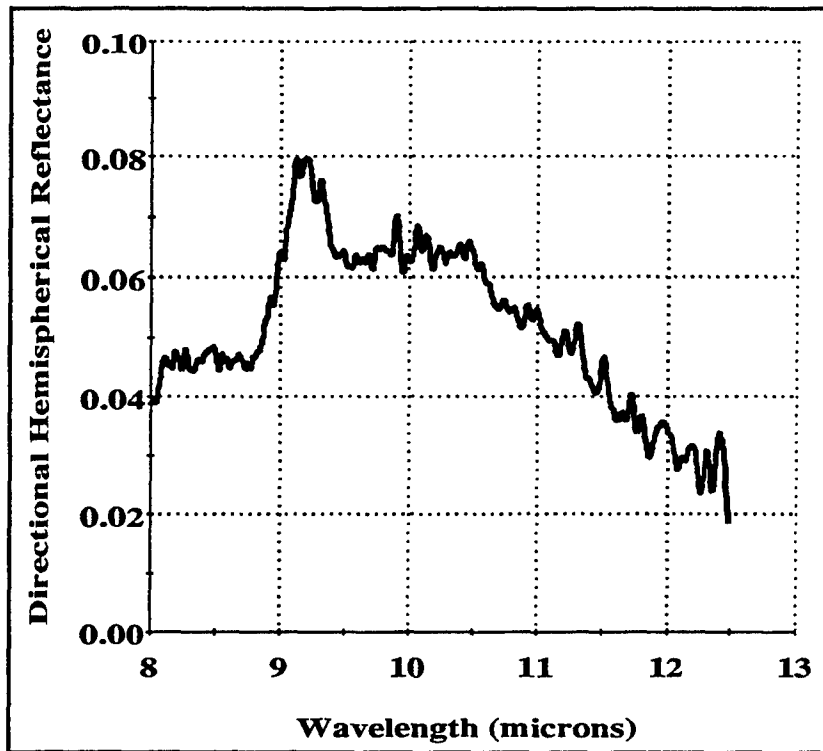


Figure 5-13. Directional Hemispherical Reflectance of CARC 383 Green Camouflage Paint.

For the painted target, the polarized emitted and reflected radiances can be written:

$$L_{V}^{E}(\lambda) = \frac{1}{2}(1 + \alpha^{E})(1 - \rho_{D}(\lambda))L^{BB}(\lambda, T_{trg}) \quad (5-37)$$

$$L_{H}^{E}(\lambda) = \frac{1}{2}(1 - \alpha^{E})(1 - \rho_{D}(\lambda))L^{BB}(\lambda, T_{trg}) \quad (5-38)$$

$$L_{V}^{R}(\lambda) = \frac{1}{2}(1 + \alpha^{R})\rho_{D}(\lambda)L^{BB}(\lambda, T_{sky}) \quad (5-39)$$

$$L_{H}^{R}(\lambda) = \frac{1}{2}(1 - \alpha^{R})\rho_{D}(\lambda)L^{BB}(\lambda, T_{sky}) \quad (5-40)$$

where

$$\alpha^{E} = \frac{\epsilon_{V}(10.6\mu\text{m}, 60.0^{\circ}) - \epsilon_{H}(10.6\mu\text{m}, 60.0^{\circ})}{\epsilon_{V}(10.6\mu\text{m}, 60.0^{\circ}) + \epsilon_{H}(10.6\mu\text{m}, 60.0^{\circ})} \quad (5-41)$$

$$\alpha^{R} = \frac{\rho_{V}(10.6\mu\text{m}, 60.0^{\circ}) - \rho_{H}(10.6\mu\text{m}, 60.0^{\circ})}{\rho_{V}(10.6\mu\text{m}, 60.0^{\circ}) + \rho_{H}(10.6\mu\text{m}, 60.0^{\circ})} \quad (5-42)$$

$$\epsilon_{V}(10.6\mu\text{m}, 60.0^{\circ}) = 1 - \rho_{V}(10.6\mu\text{m}, 60.0^{\circ}) \quad (5-43)$$

$$\epsilon_{H}(10.6\mu\text{m}, 60.0^{\circ}) = 1 - \rho_{H}(10.6\mu\text{m}, 60.0^{\circ}) \quad (5-44)$$

So we see that the target has a different degree of polarization in both emission and reflection. The total target degree of polarization is given as:

$$\alpha = \frac{(L^E_V(\lambda) + L^R_V(\lambda)) - (L^E_H(\lambda) + L^R_H(\lambda))}{(L^E_V(\lambda) + L^R_V(\lambda)) + (L^E_H(\lambda) + L^R_H(\lambda))} \quad (5-45)$$

and is plotted in Figure 5-14. It is expected that the target degree of polarization will decrease for target view angles less than 60 degrees from nadir. This is due to a decrease in induced polarization away from grazing angles. Thus the case presented represents one which may be more polarized than typical target viewing geometries would provide.

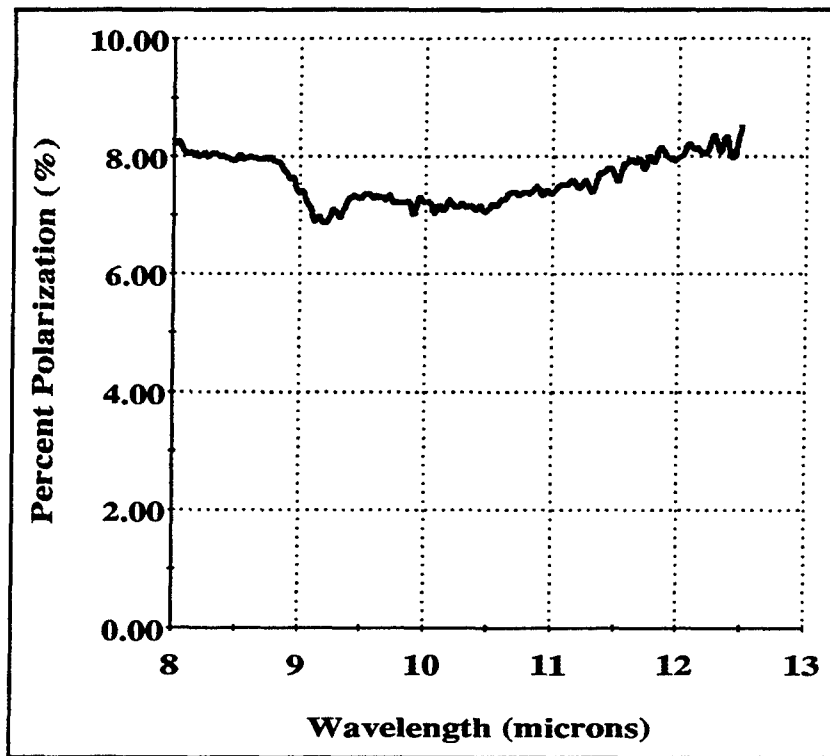


Figure 5-14. Target Degree of Polarization (Includes Both Emission and Reflection).

Polarimeter measurements of backgrounds conducted by ERIM have shown grass backgrounds to be highly unpolarized with the largest measured degree of polarization being 0.003 (0.3%) and typically less. However, for this analysis it will be assumed that the grass background has this level of radiance polarization.

Figure 5-15 displays anticipated results for the case of mean measurement errors due to sensor polarization sensitivity. The mean measurement errors are plotted as a percent radiance error, i.e. the difference between the polarized and unpolarized radiances normalized by the unpolarized

radiance. It is anticipated that for mostly unpolarized backgrounds the mean radiance error is less than 0.05% and negligible. Targets polarized on the level of the CARC 383 green painted example target (at a 60 degree view angle) are expected to provide mean radiance errors of between 0.2 and 1.0 %, depending on the wavelength. Notice the spectral shape of the target mean radiance error. This spectral shape matches the spectral shape of the sensor polarization sensitivity shown in Section 4.7. This spectral shape can be searched for to identify cases where sensor polarization sensitivity has created mean radiance errors.

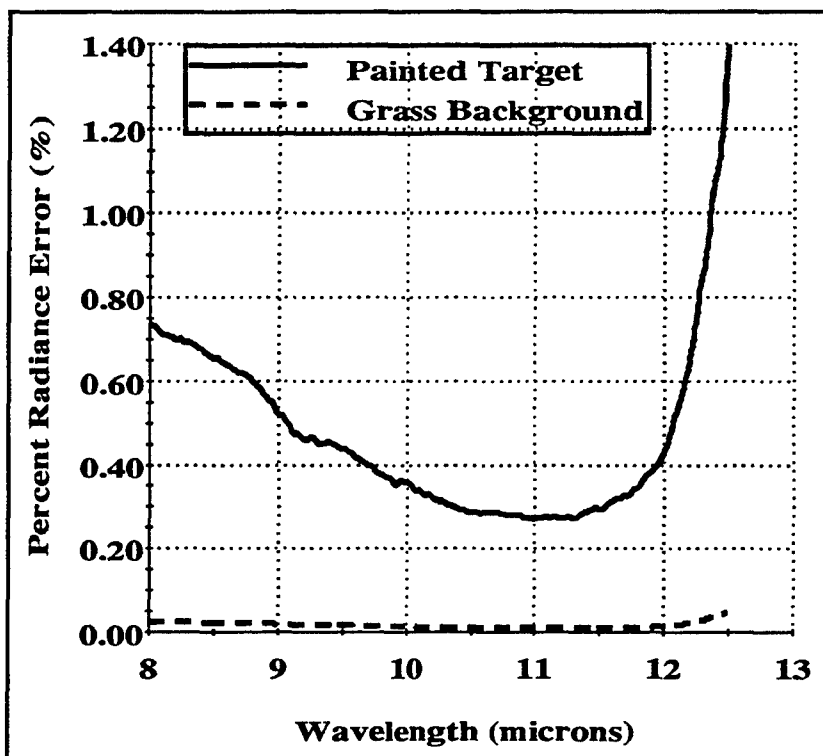


Figure 5-15. Target and Background Radiance Error Due to Sensor Polarization Sensitivity.

Errors in mean contrast due to sensor polarization sensitivity can be more significant, particularly if the mean contrast is small. Figure 5-16 displays the anticipated results when the target and background physical temperatures are perfectly matched. We see that for such an extreme case the sensor polarization sensitivity can create mean contrast errors on the order of 10 to 30%. It should be remembered that this polarized error level is based on the target polarization level defined for a 60 degree view angle from nadir. As the target view angle decreases the target degree of polarization is expected to decrease and thus also the mean contrast errors. In addition, as the mean contrast increases, the proportion of measured mean contrast described by polarization will decrease.

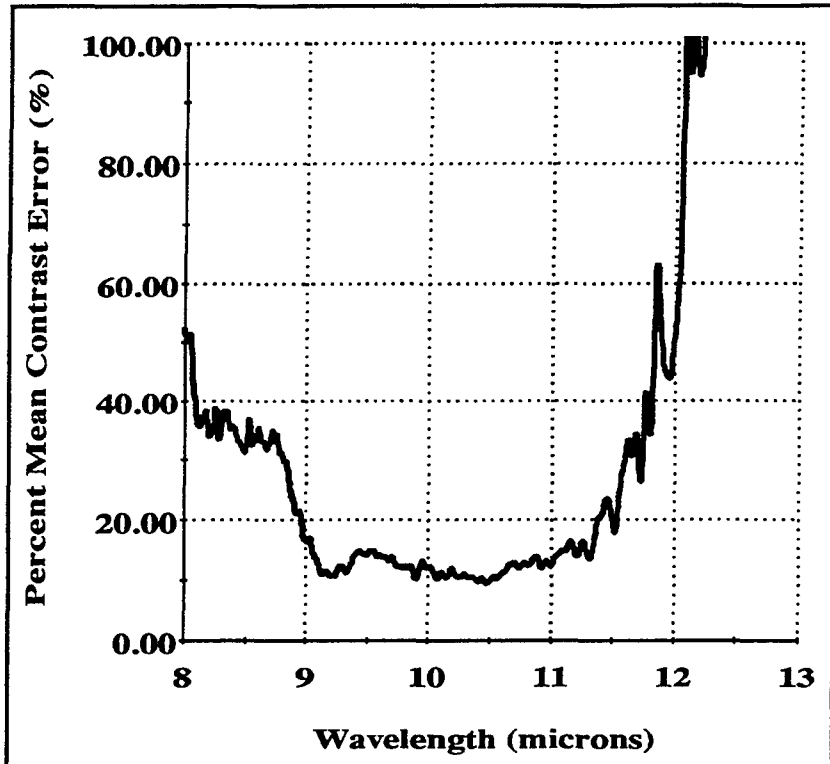


Figure 5-16. Mean Contrast Error Due to Sensor Polarization Sensitivity.

If backgrounds are polarized, then the sensor's spectral polarization sensitivity can limit band-to-band correlation measurements. Figure 5-17 shows the dependence of maximum equivalent clutter suppression on the level of background polarization. It was assumed that the background polarization variance (σ_{α}) was one sixth of the background polarization level (α). This assumption is based on empirical grass background measurements which have shown the degree of polarization to be less than 0.3% with an approximate rms variation of 0.05%. These results suggest that it requires background polarization levels in excess of 1.0% to limit measured band-to-band correlations to less than 0.9999 (37dB) for any band combination and for a moderate clutter level of 1K (σ_T).

Figure 5-18 provides the maximum correlation performance, shown as maximum equivalent clutter suppression, as a function of background clutter level. The same grass background polarization levels discussed above were assumed (i.e., $\alpha = 0.3\%$ and $\sigma_{\alpha} = 0.05\%$). These results suggest that sensor polarization sensitivity is not expected to significantly limit background correlation measurements for any band combination, including MWIR/LWIR band pairs.

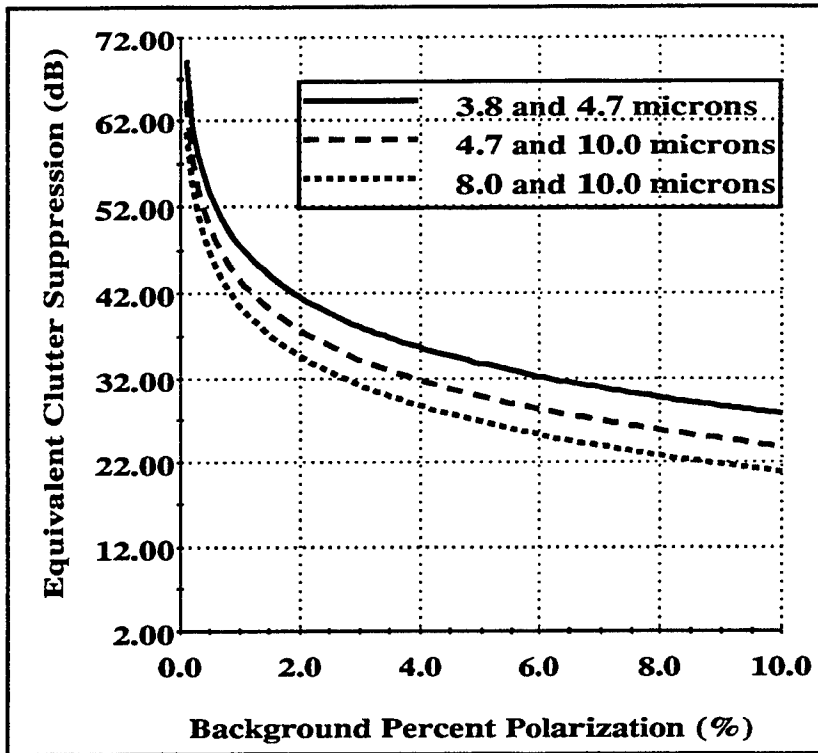


Figure 5-17. Maximum Equivalent Clutter Suppression vs. Background Polarization Level α (%) (Polarization variance $\sigma_\alpha = 0.167\alpha$, $\sigma_T=1K$, $\epsilon_{bkg}=0.98$, $T_{bkg}=300K$, $T_{sky}=250K$).

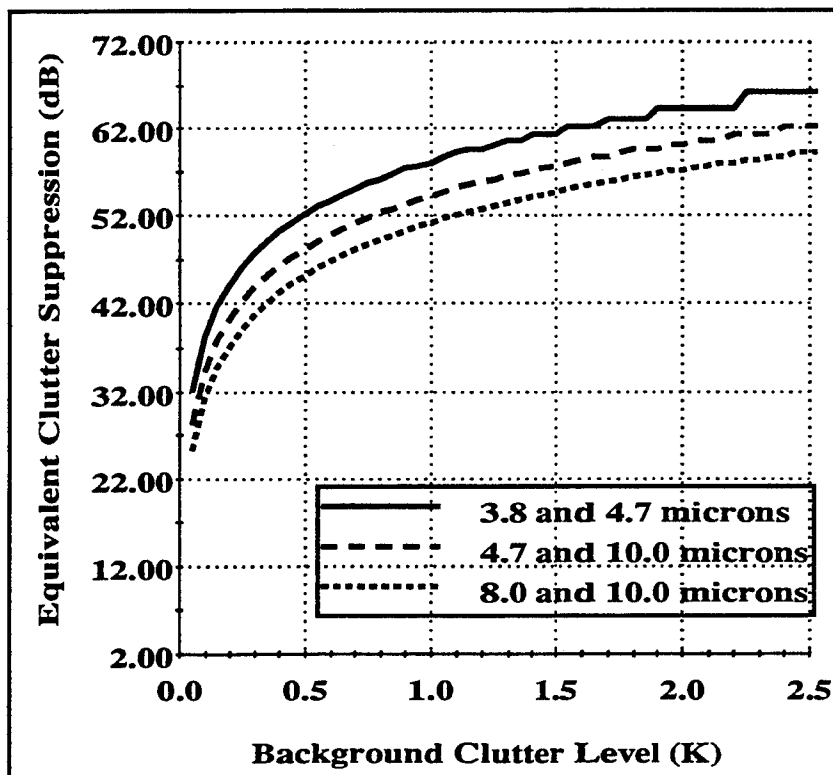


Figure 5-18. Maximum Equivalent Clutter Suppression vs. Background Clutter Level (σ_T) ($\alpha=0.3\%$, $\sigma_\alpha=0.05\%$, $\epsilon_{bkg}=0.98$, $T_{bkg}=300K$, $T_{sky}=250K$).

5.8 SPATIAL FOOTPRINT

5.8.1 Effects on Measurements

The size and shape of the spatial sensor footprint is not a critical concern. It is, however, worthwhile to measure to insure interpretability of the measured data, that is, to know precisely what the instrument is looking at for each measurement.

5.8.2 Anticipated Level

With the 10" Cassegrain telescope, the IFOV of the FTS will be 5 mrad. The shape of the spatial footprint will be roughly uniform with some tapering at the edges due to diffraction. The diffraction-limited blur circle projected out the front of the telescope is roughly 0.1 mrad in the LWIR and 0.05 mrad in the MWIR. At 100 m range, therefore, we anticipate a circular spatial footprint with 0.5 m diameter. Because the size of the footprint is wavelength independent and the sidelobes are very small, spatial footprint will not introduce an error in the measured mean radiances or band-to-band background correlation levels.

5.9 SPATIAL REGISTRATION

Misregistration between detectors can severely limit a sensor's ability to preserve high background correlation levels. When the sensor sees two different spatial locations of a spatially varying target or background in two different bands, then the overall band-to-band correlation decreases due to a lack of correlation between these different spatial locations. The magnitude of expected band-to-band sensor decorrelation is dependent on the joint spatial-spectral statistics of the background and on the degree of band-to-band misregistration. The derivation of an analytic solution describing this relationship is complicated by the requirement of a joint spatial-spectral characterization. The level of effort required to properly analyze this effect was determined to be beyond the scope of the effort described, and will be reserved for future studies.

5.10 POINTING ACCURACY

5.10.1 Effects on Measurements

Pointing inaccuracies do not affect mean radiance and band-to-band background correlation measurements unless the inaccuracies are so large and random such that they reduce the independence of the individual point measurements. If such pointing inaccuracies did exist, they would manifest themselves as an increase in the error bounds of the measured statistics.

5.10.2 Anticipated Level

The absolute accuracy of the pan and tilt stages is specified at 0.5 arc min (0.15 mrad) which corresponds to roughly 1/33 of an IFOV. This level of pointing error is not expected to affect the measured statistics in any meaningful way.

5.11 POINTING REPEATABILITY

5.11.1 Effects on Measurements

Repeatability is only important if one performs experiments in which we need to repetitively point to a target or background pixel and are interested in differences between sequential measurements. In this case, repeatability errors could lead to interpretive analysis errors since one could unknowingly attempt to compare nonsimilar target or background areas.

5.11.2 Anticipated Level

The repeatability of the pan and tilt stages was measured and is discussed in detail in Section 4.11. The results show that, for unidirectional scans, pointing repeatability is better than 1/100 of an IFOV. For bidirectional scans, pointing repeatability was shown to be always better than 1/30 of an IFOV. Motion of the sensor platform (e.g., tower) will likely cause a significantly larger error than this. For example, under some conditions one might expect 6 inches of tower sway which corresponds to 1/13 of an IFOV at a 400 m range.

5.12 POINTING STABILITY

5.12.1 Effects on Measurements

Since the FTS acquires all spectral bands simultaneously, pointing instabilities will not affect the spectral properties. Rather, instabilities will merely blur the effective spatial footprint. Therefore, if they are maintained at a small fraction of the IFOV, the effects will be negligible.

5.12.2 Anticipated Level

Transient instabilities directly after moving the sensor line-of-sight will be dictated by the inertia of the instrument, the torque of the drive motors, the deceleration rate, and how well the instrument is balanced in the mount. For moderate to small step sizes (< 1 degree), the pointing stability was found to be better than $1/100$ of an IFOV. For large step sizes (> 10 degrees), the pointing stability was on the order of $1/10$ to $1/25$ of an IFOV. Wind was also found to sometimes limit pointing stability to about $1/20$ of an IFOV. However, in all of these cases the effects of pointing stability with respect to radiometric measurements is negligible because of the simultaneous collection of all wavelengths.

6.0 PRELIMINARY DATA ANALYSIS RESULTS

Phase 2 data collections will take place at both vegetated and arid sites. Under EO CC&D contract funding, collections were completed at vegetated sites at WPAFB and Redstone Arsenal. The data were collected by an IR Fourier transform spectrometer with InSb and MCT detectors covering 3 to 5 micron and 8 to 12 micron bands, respectively. The spectrometer has a very low noise equivalent spectral radiance to enable high quality measurements. It is on a computer controlled pan/tilt mount to enable automated measurement sequences. Two high quality blackbodies are used for calibration. The spectrometer was placed on towers at elevations from 100 to 300 feet.

Target and test panels of size 5 feet by 5 feet outfitted with temperature probes were used. One target panel is painted with the green (383) component of the current Army chemical agent resistive (CARC) three color camouflage set and the other with a next generation Army low emissivity green camouflage paint. Current and next generation Army camouflage nets were used as targets as well as camouflage painted Army trucks. Data were taken under day, night, and thermal crossover conditions, under clear and cloudy skies, under dry and wet conditions, and with variations in the look angle to the target.

The results of preliminary analysis of the data are shown in Figures 6-1 through 6-5. Figure 6-1 shows the correlation of treeline (including grass, tree trunks, undergrowth, and tree tops) spectra with the treeline radiance at 10.1 microns including confidence bounds and the sensor noise correlation limit. The correlation of greater than 0.9997 in the 8 to 12 micron region is higher than other sensors have been able to measure. These high correlations support high IR multispectral processing gain for target detection in cluttered backgrounds.

Figure 6-2 shows the target/background mean radiance contrast for the CARC 383 green panel (specular to the sky) with the treeline. The measurement was taken at 8 am near the time of thermal crossover. It shows evidence of spectral contrast color variation necessary for high multispectral processing gain.

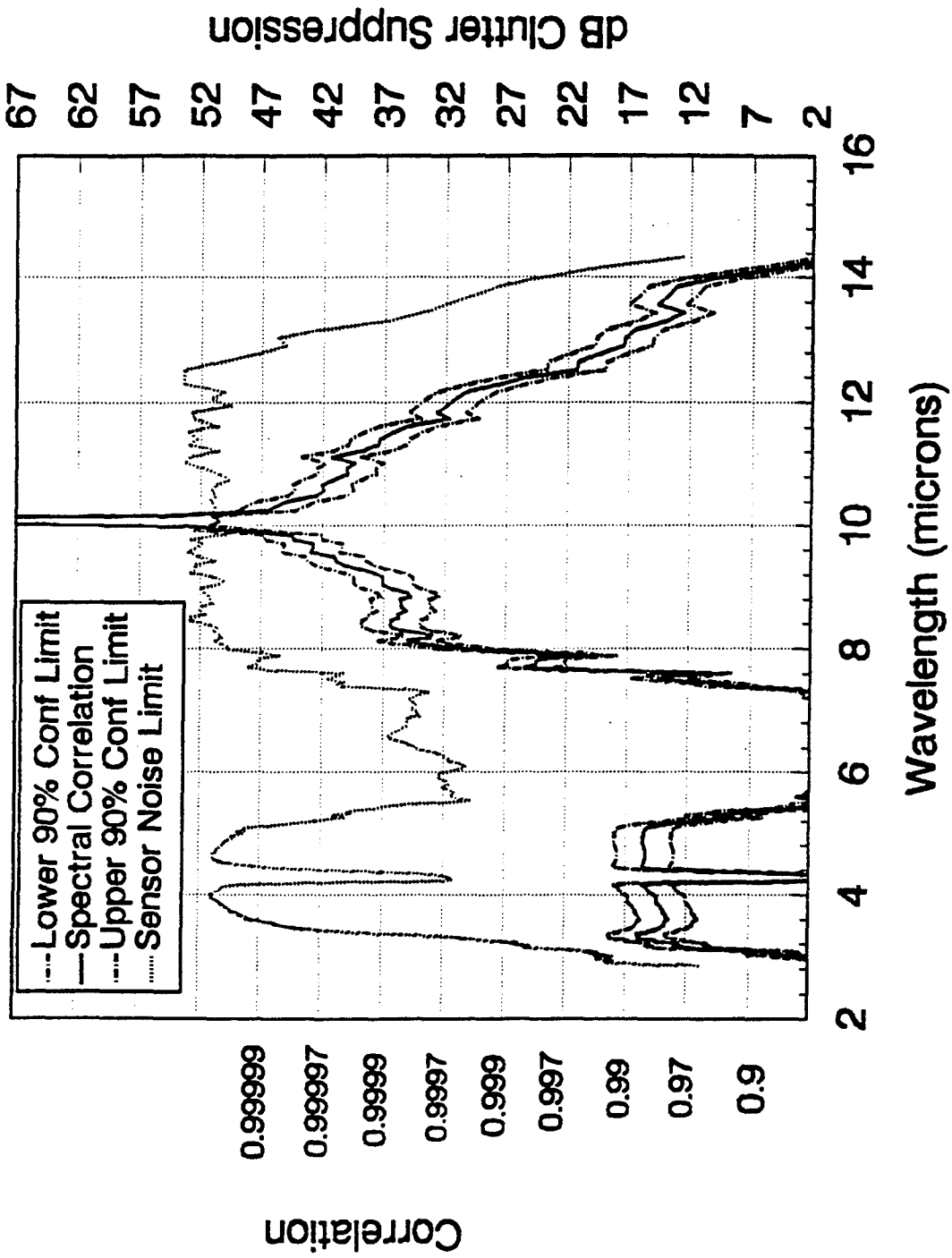


Figure 6-1. Treeline Correlation With 10.1 Microns

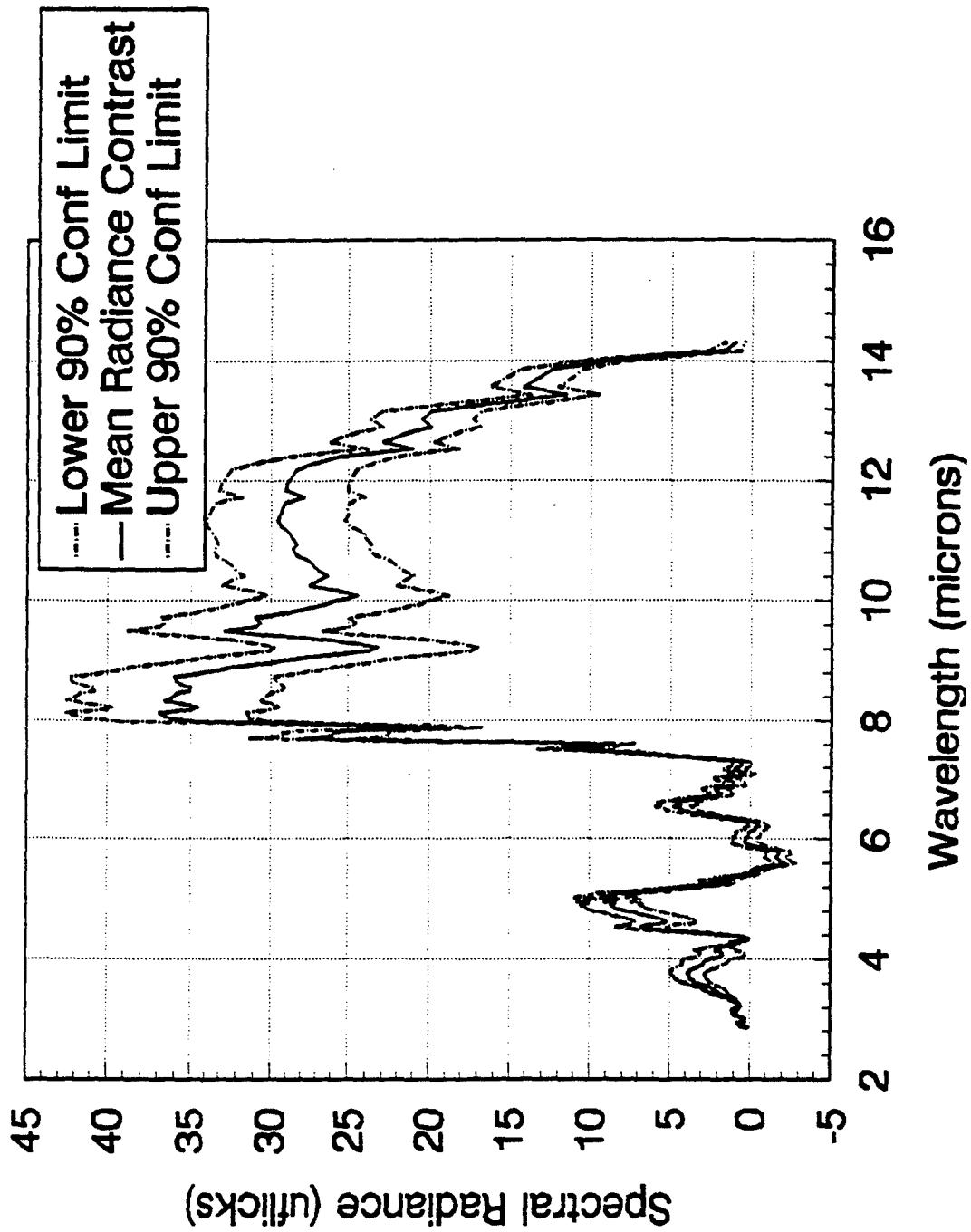


Figure 6-2. Mean Contrast: CARC Panel vs Treeline

Figure 6-3 is a scatter plot of the target and background data in narrow bands centered at 8.3 and 10.1 microns. It is clear that the target pixel would be poorly detected in either single band but can be detected very well when the two bands are combined due to the favorable coloring and a very high clutter correlation of 0.9998.

Figure 6-4 shows the single-band signal-to-clutter ratio and the dual band signal-to-clutter ratio obtained by pairing the 10.1 micron band with the other bands. Figure 6-4 confirms the high dual band target detectability at signal-to-clutter ratios of 28 to 32 dB in various LWIR band pairs.

Figure 6-5 is a scatter plot of target and background data in two narrow bands centered at 5 and 11 microns. It shows the time history of the data from 7:30 to 8:30 am which is near thermal crossover. The target is detectable using only the 11 micron band at 7:30 and 8 am but becomes less detectable as the conditions approach thermal crossover at 8:30 am. However, the target clearly remains detectable when the two bands are combined. This is another example of IR multispectral target detection gain.

Under IRIA contract funding, Phase 2 of the Multispectral Sensor Program will analyze the wealth of data collected. It is expected that the promising preliminary results discussed above will be confirmed.

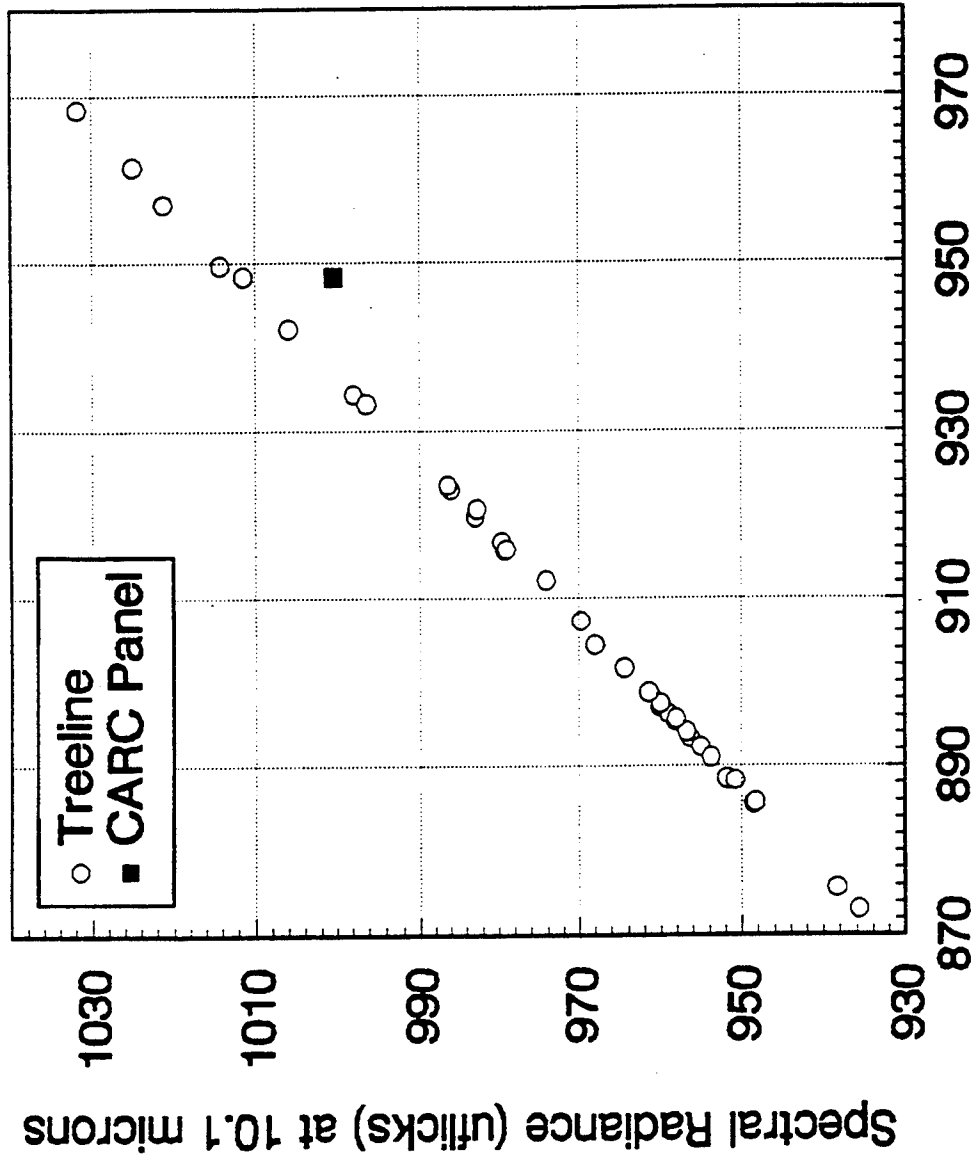


Figure 6-3. CARC Panel and Treeline

Spectral Radiance (uflicks) at 10.1 microns

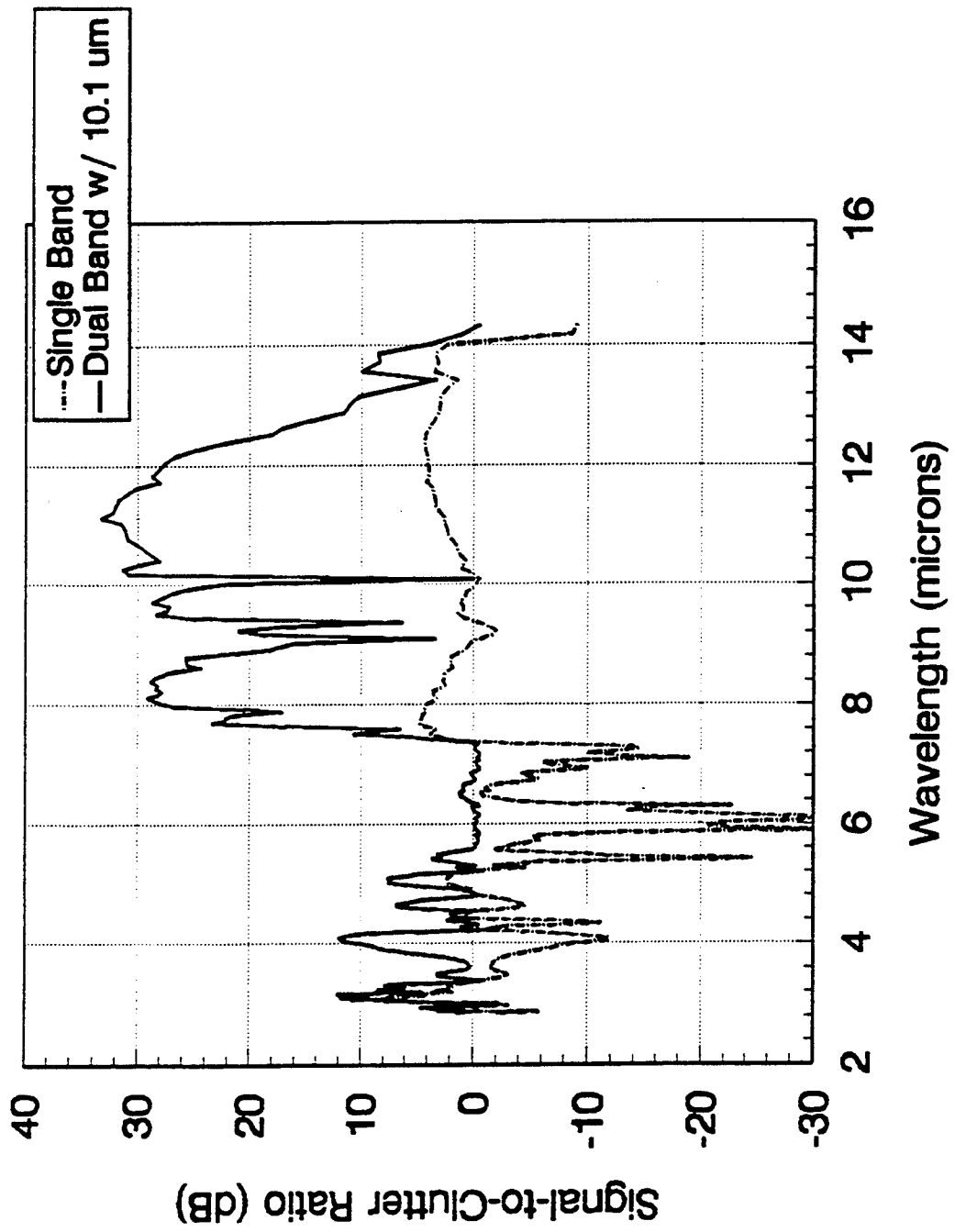
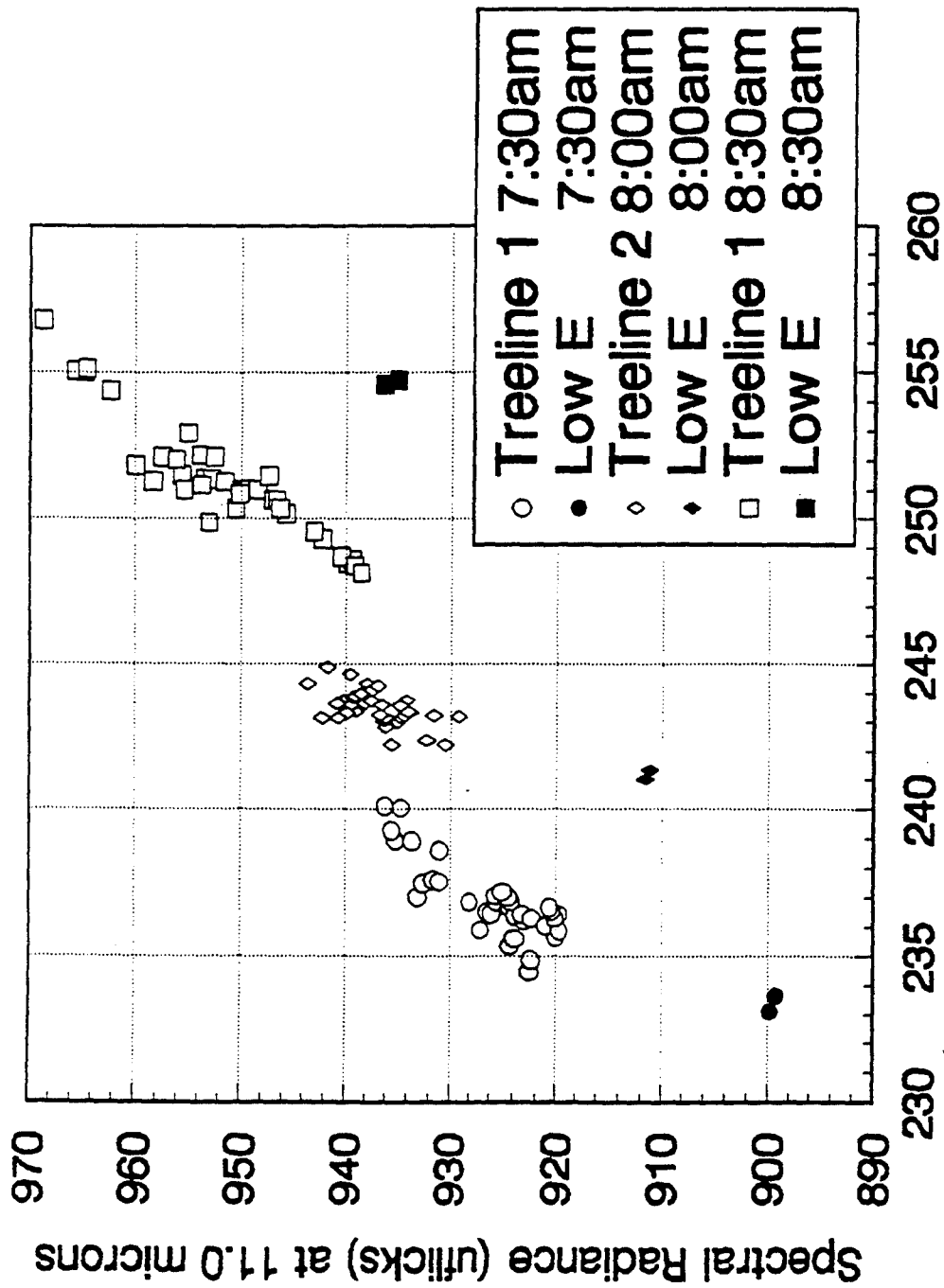


Figure 6-4. Signal-to-Clutter Ratio for CARC Panel vs Treeline



Spectral Radiance (uflicks) at 5.0 microns

Figure 6-5. Low Emissivity Panel and Treeline

Appendix A. Confidence Limits for Quick-Look Parameter Estimates

A.1 INTRODUCTION AND SUMMARY

This memo provides statistically valid confidence limits for several parameters that will be estimated and plotted for "quick-look" analysis during the Bomem FTS data collection experiments. These parameters include mean radiance, mean radiance contrast, radiance variance, and spectral correlation coefficient. All confidence limits are based on the assumption of homogeneous Gaussian-distributed samples, consistent with the approach taken in last year's performance modeling studies. The limits are also valid for small sample sizes, which is important because of the practical constraints on the number of independent spatial samples that can be collected from targets (primarily due to area limitations) and backgrounds (primarily due to time limitations).

A.2 MEAN RADIANCE

Mean radiances (vs. λ) of targets and backgrounds will be estimated from finite numbers of spatial samples (i.e., spectrometer scans). Since the true mean and variance of the samples are unknown in advance, any uncertainty in the variance of the resulting mean estimate should be explicitly accounted for when forming a confidence interval for the mean.

Assume that the radiance samples $x_n(\lambda)$, $n=1,\dots,N$ are Gaussian distributed with true mean $\mu(\lambda)$ and variance $\sigma^2(\lambda)$. The sample mean and variance of the $x_n(\lambda)$ are computed as

$$\bar{x}(\lambda) = \frac{1}{N} \sum x_n(\lambda) \quad (\text{A.1})$$

$$s_x^2(\lambda) = \frac{1}{N-1} \sum [x_n(\lambda) - \bar{x}(\lambda)]^2 \quad (\text{A.2})$$

These are unbiased estimates of $\mu(\lambda)$ and $\sigma^2(\lambda)$, respectively. Confidence limits on the mean when the variance is unknown are based on the normalized statistic

$$T = \frac{\bar{x}(\lambda) - \mu(\lambda)}{s_x(\lambda) / \sqrt{N}} \quad (\text{A.3})$$

which has a t-distribution with $N-1$ degrees-of-freedom [A.1]. The $(1-\alpha)$ confidence interval for the mean radiance $\mu(\lambda)$ is therefore given by

$$\left[\bar{x}(\lambda) - t_{1-\alpha/2}(N-1) \cdot s_x(\lambda) / \sqrt{N}, \bar{x}(\lambda) + t_{1-\alpha/2}(N-1) \cdot s_x(\lambda) / \sqrt{N} \right] \quad (\text{A.4})$$

where $t_{1-\alpha/2}(N-1)$ is the threshold corresponding to a cumulative probability of $1-\alpha/2$ on the t-distribution with $N-1$ degrees-of-freedom. The t-distribution is symmetric about zero and approaches the standard normal distribution in the limit as $N \rightarrow \infty$. Probability points on the cumulative t-distribution are tabulated

in numerous references [A.1,A.2] (see Table A-1). Since the t-values are fairly sensitive to N for N<30 samples or so, a table of t-thresholds vs. N for the desired confidence level (1- α) should be maintained by the quick-look system.

A.3 MEAN RADIANCE CONTRAST

Mean radiance contrast will be estimated as a function of λ for various target-background combinations. In each case, two sets of Gaussian spatial samples are assumed to be available for a given λ : one set from a target area and another from a nearby background region of interest. We will assume that the target and background samples are independent of one another since they are collected from different locations at different times.

Let $x_n(\lambda)$, $n=1,\dots,N$ denote a set of N target radiance samples with true mean $\mu_x(\lambda)$ and variance $\sigma_x^2(\lambda)$, and let $y_m(\lambda)$, $m=1,\dots,M$ denote a set of M background radiance samples with true mean $\mu_y(\lambda)$ and variance $\sigma_y^2(\lambda)$. The target-background mean contrast to be estimated is the difference in means $\Delta\mu(\lambda)=\mu_x(\lambda)-\mu_y(\lambda)$. It is relatively easy to obtain confidence intervals for a difference in means in special cases where $\sigma_x^2(\lambda)=\sigma_y^2(\lambda)$ or $N=M$; many statistics texts provide these solutions. However, for most of our experimental data we expect the variances and sample sizes to differ for the target and background populations. In this general case it appears to be impossible to find a statistic involving $\Delta\mu(\lambda)$ and the individual sample means $\bar{x}(\lambda)$ and $\bar{y}(\lambda)$ that does not depend on the ratio of the unknown variances $\sigma_x^2(\lambda)$ and $\sigma_y^2(\lambda)$.

A clever trick that converts this general problem to a tractable one has been suggested by Muirhead [A.3]. Suppose that the number of target samples N is less than the number of background samples M (probably always the case). Then define a new set of N random variables $z_n(\lambda)$ from the original observations as

$$z_n(\lambda) = x_n(\lambda) - (N/M)^{1/2} y_n(\lambda) + (NM)^{-1/2} \sum_{i=1}^N y_i(\lambda) - M^{-1} \sum_{j=1}^M y_j(\lambda) \quad (\text{A.5})$$

where $n=1,\dots,N$. Given the assumed statistical properties of the target and background samples, it is readily shown that the $z_n(\lambda)$ are independent, identically distributed random samples from a Gaussian distribution with mean and variance

$$\begin{aligned} \mu_z(\lambda) &= \mu_x(\lambda) - \mu_y(\lambda) = \Delta\mu(\lambda) \\ \sigma_z^2(\lambda) &= \sigma_x^2(\lambda) + \frac{N}{M} \sigma_y^2(\lambda) \end{aligned} \quad (\text{A.6})$$

The problem is now converted to that of finding a confidence interval on the unknown mean $\Delta\mu(\lambda)$ of a set of i.i.d. Gaussian samples $\{z_n(\lambda), n=1,\dots,N\}$ of unknown variance. This is exactly the same problem that was encountered above in finding the mean radiance confidence interval. Applying those results to the present case, the confidence interval for the mean radiance contrast $\Delta\mu(\lambda)$ is given by

Table A-1. Student's t-Distribution

PERCENTAGE POINTS, STUDENTS t-DISTRIBUTION

$$F(t) = \int_{-\infty}^t \frac{\Gamma\left(\frac{n+1}{2}\right)}{\sqrt{nr} \Gamma\left(\frac{n}{2}\right)} \left(1 + \frac{x^2}{n}\right)^{-\frac{n+1}{2}} dx$$

$\frac{F}{n}$.60	.75	.90	.95	.975	.99	.995	.9995
1	.325	1.000	3.078	6.314	12.706	31.821	63.657	636.619
2	.289	.816	1.886	2.920	4.303	6.965	9.925	31.598
3	.277	.765	1.638	2.353	3.182	4.541	5.841	12.924
4	.271	.741	1.533	2.132	2.776	3.747	4.604	8.610
5	.267	.727	1.476	2.015	2.571	3.365	4.032	6.869
6	.265	.718	1.440	1.943	2.447	3.143	3.707	5.959
7	.263	.711	1.415	1.895	2.365	2.998	3.499	5.408
8	.262	.706	1.397	1.860	2.306	2.896	3.355	5.041
9	.261	.703	1.383	1.833	2.262	2.821	3.250	4.781
10	.260	.700	1.372	1.812	2.228	2.764	3.169	4.587
11	.260	.697	1.363	1.796	2.201	2.718	3.106	4.437
12	.259	.695	1.356	1.782	2.179	2.681	3.055	4.318
13	.259	.694	1.350	1.771	2.160	2.650	3.012	4.221
14	.258	.692	1.345	1.761	2.145	2.624	2.977	4.140
15	.258	.691	1.341	1.753	2.131	2.602	2.947	4.073
16	.258	.690	1.337	1.746	2.120	2.583	2.921	4.015
17	.257	.689	1.333	1.740	2.110	2.567	2.898	3.965
18	.257	.688	1.330	1.734	2.101	2.552	2.878	3.922
19	.257	.688	1.328	1.729	2.093	2.539	2.861	3.883
20	.257	.687	1.325	1.725	2.086	2.528	2.845	3.850
21	.257	.686	1.323	1.721	2.080	2.518	2.831	3.819
22	.256	.686	1.321	1.717	2.074	2.508	2.819	3.792
23	.256	.685	1.319	1.714	2.069	2.500	2.807	3.767
24	.256	.685	1.318	1.711	2.064	2.492	2.797	3.745
25	.256	.684	1.316	1.708	2.060	2.485	2.787	3.725
26	.256	.684	1.315	1.706	2.056	2.479	2.779	3.707
27	.256	.684	1.314	1.703	2.052	2.473	2.771	3.690
28	.256	.683	1.313	1.701	2.048	2.467	2.763	3.674
29	.256	.683	1.311	1.699	2.045	2.462	2.756	3.659
30	.256	.683	1.310	1.697	2.042	2.457	2.750	3.646
40	.255	.681	1.303	1.684	2.021	2.423	2.704	3.551
60	.254	.679	1.296	1.671	2.000	2.390	2.660	3.460
120	.254	.677	1.289	1.658	1.980	2.358	2.617	3.373
∞	.253	.674	1.282	1.645	1.960	2.326	2.576	3.291

$$\left[\bar{z}(\lambda) - t_{1-\alpha/2}^{(N-1)} \cdot s_z(\lambda)/\sqrt{N}, \bar{z}(\lambda) + t_{1-\alpha/2}^{(N-1)} \cdot s_z(\lambda)/\sqrt{N} \right] \quad (\text{A.7})$$

where

$$\bar{z}(\lambda) = \frac{1}{N} \sum_n z_n(\lambda)$$

$$s_z^2(\lambda) = \frac{1}{(N-1)} \sum_n [z_n(\lambda) - \bar{z}(\lambda)]^2$$

are the sample mean and variance of the $z_n(\lambda)$ defined in (A.5), and where $t_{1-\alpha/2}^{(N-1)}$ is the threshold corresponding to a cumulative probability of $1-\alpha/2$ on the t-distribution with $N-1$ degrees-of-freedom.

A.4 RADIANCE VARIANCE

For a set of spatial samples $x_n(\lambda)$, $n=1, \dots, N$, the sample variance is computed as

$$s_x^2(\lambda) = \frac{1}{N-1} \sum [x_n(\lambda) - \bar{x}(\lambda)]^2 \quad (\text{A.8})$$

where $\bar{x}(\lambda)$ is the sample mean. If the true variance of the sample is $\sigma_x^2(\lambda)$, then the normalized statistic

$$Q = (N-1)s_x^2(\lambda)/\sigma_x^2(\lambda) \quad (\text{A.9})$$

is known to have a chi-square distribution with $N-1$ degrees of freedom [A.1]. A $(1-\alpha)$ confidence interval on the true variance $\sigma_x^2(\lambda)$ is given by

$$\left[\frac{(N-1)s_x^2(\lambda)}{q_2}, \frac{(N-1)s_x^2(\lambda)}{q_1} \right] \quad (\text{A.10})$$

where q_1 and q_2 are selected such that $\text{Prob}\{q_1 < Q < q_2\} = (1-\alpha)$. Typically, one selects q_1 and q_2 such that there is equal probability mass $\alpha/2$ to either side of the confidence interval. In this case, the desired confidence interval for the variance $\sigma_x^2(\lambda)$ becomes

$$\left[\frac{(N-1)s_x^2(\lambda)}{\chi_{1-\alpha/2}^2(N-1)}, \frac{(N-1)s_x^2(\lambda)}{\chi_{\alpha/2}^2(N-1)} \right] \quad (\text{A.11})$$

where $\chi_p^2(N-1)$ denotes the threshold corresponding to probability p on the cumulative chi-square distribution with $N-1$ degrees-of-freedom. Chi-square thresholds are given in Table A-2. Note that

Table A-2. Percentage Points of the Chi-Square Distribution

$$F(x^2) = \int_0^{x^2} \frac{1}{2^{\frac{n}{2}} \Gamma(\frac{n}{2})} x^{\frac{n-2}{2}} e^{-\frac{x}{2}} dx$$

F n	.005	.010	.025	.050	.100	.250	.500	.750	.900	.950	.975	.980	.985
1	.000393	.000157	.000982	.00393	.0158	.102	.455	1.32	2.71	3.84	5.02	6.63	7.88
2	.0100	.0201	.0506	.103	.211	.575	1.39	2.77	4.61	5.99	7.38	9.21	10.6
3	.0717	.115	.216	.352	.584	1.21	2.37	4.11	6.25	7.81	9.35	11.3	12.8
4	.207	.287	.484	.711	1.06	1.92	3.36	5.39	7.78	9.49	11.1	13.3	14.9
5	.412	.554	.831	1.15	1.61	2.67	4.35	6.63	9.24	11.1	12.8	15.1	16.7
6	.676	.872	1.24	1.64	2.20	3.45	5.35	7.84	10.6	12.6	14.4	16.8	18.5
7	.989	1.24	1.69	2.17	2.83	4.25	6.35	9.04	12.0	14.1	16.0	18.5	20.3
8	1.34	1.65	2.18	2.73	3.49	5.07	7.34	10.2	13.4	15.5	17.5	20.1	22.0
9	1.73	2.09	2.70	3.33	4.17	5.90	8.34	11.4	14.7	16.9	19.0	21.7	23.6
10	2.16	2.56	3.25	3.94	4.87	6.74	9.34	12.5	16.0	18.3	20.5	23.2	25.2
11	2.60	3.05	3.82	4.57	5.58	7.58	10.3	13.7	17.3	19.7	21.9	24.7	26.8
12	3.07	3.57	4.40	5.23	6.30	8.44	11.3	14.8	18.5	21.0	23.3	26.2	28.3
13	3.57	4.11	5.01	5.89	7.04	9.30	12.3	16.0	19.8	22.4	24.7	27.7	29.8
14	4.07	4.66	5.63	6.57	7.79	10.2	13.3	17.1	21.1	23.7	26.1	29.1	31.3
15	4.60	5.23	6.26	7.26	8.55	11.0	14.3	18.2	22.3	25.0	27.5	30.6	32.8
16	5.14	5.81	6.91	7.96	9.31	11.9	15.3	19.4	23.5	26.3	28.8	32.0	34.3
17	5.70	6.41	7.56	8.67	10.1	12.8	16.3	20.5	24.8	27.6	30.2	33.4	35.7
18	6.26	7.01	8.23	9.39	10.9	13.7	17.3	21.6	26.0	28.9	31.5	34.8	37.2
19	6.84	7.63	8.91	10.1	11.7	14.6	18.3	22.7	27.2	30.1	32.9	36.2	38.6
20	7.43	8.26	9.59	10.9	12.4	15.5	19.3	23.8	28.4	31.4	34.2	37.6	40.0
21	8.03	8.90	10.3	11.6	13.2	16.3	20.3	24.9	29.6	32.7	35.5	38.9	41.4
22	8.64	9.54	11.0	12.3	14.0	17.2	21.3	26.0	30.8	33.9	36.8	40.3	42.8
23	9.26	10.2	11.7	13.1	14.8	18.1	22.3	27.1	32.0	35.2	38.1	41.6	44.2
24	9.89	10.9	12.4	13.8	15.7	19.0	23.3	28.2	33.2	36.4	39.4	43.0	45.6
25	10.5	11.5	13.1	14.6	16.5	19.9	24.3	29.3	34.4	37.7	40.6	44.3	46.9
26	11.2	12.2	13.8	15.4	17.3	20.8	25.3	30.4	35.6	38.9	41.9	45.6	48.3
27	11.8	12.9	14.6	16.2	18.1	21.7	26.3	31.5	36.7	40.1	43.2	47.0	49.6
28	12.5	13.6	15.3	16.9	18.9	22.7	27.3	32.6	37.9	41.3	44.5	48.3	51.0
29	13.1	14.3	16.0	17.7	19.8	23.6	28.3	33.7	39.1	42.6	45.7	49.6	52.3
30	13.8	15.0	16.8	18.5	20.6	24.5	29.3	34.8	40.3	43.8	47.0	50.9	53.7

confidence limits on the standard deviation $\sigma_x(\lambda)$ are obtained simply by taking the square roots of the limits given in (A.11).

A.5 SPECTRAL CORRELATION COEFFICIENT

Given a set of N spatial samples $x_n(\lambda_1)$ and $x_n(\lambda_2)$ collected in two spectral bands, an estimate of the spectral correlation coefficient is given by

$$r(\lambda_1, \lambda_2) = \frac{\frac{1}{N-1} \sum [x_n(\lambda_1) - \bar{x}(\lambda_1)] [x_n(\lambda_2) - \bar{x}(\lambda_2)]}{s_x(\lambda_1) s_x(\lambda_2)} \quad (\text{A.12})$$

where $\bar{x}(\lambda_i)$ and $s_x(\lambda_i)$, $i=1,2$, denote the sample mean and standard deviations for the individual bands.

To derive a confidence interval on the correlation coefficient estimate $r(\lambda_1, \lambda_2)$, it is most convenient to work with Fisher's transformed statistic

$$y = \frac{1}{2} \log \left[\frac{1+r(\lambda_1, \lambda_2)}{1-r(\lambda_1, \lambda_2)} \right] = \tanh^{-1} r(\lambda_1, \lambda_2) \quad (\text{A.13})$$

which is known to converge very rapidly in N to a Gaussian random variable with mean and variance

$$\begin{aligned} \mu_y &= \tanh^{-1} \rho(\lambda_1, \lambda_2) \\ \sigma_y^2 &= \frac{1}{N} \end{aligned} \quad (\text{A.14})$$

with $\rho(\lambda_1, \lambda_2)$ being the true spectral correlation of the process [A.3]. Simulation experiments show that the transformed statistic y is for all practical purposes a Gaussian variable when $N > 10$. This is convenient since confidence bounds on Gaussian statistics are easy to calculate. If we let

$$z = \frac{\mu_y - y}{\sigma_y} = \frac{\tanh^{-1} \rho(\lambda_1, \lambda_2) - \tanh^{-1} r(\lambda_1, \lambda_2)}{1/\sqrt{N}} \quad (\text{A.15})$$

then z is approximately standard normal and we can immediately write the confidence bound expression

$$\text{Prob}\{-Q^{-1}(\alpha/2) < z < Q^{-1}(\alpha/2)\} = 1-\alpha \quad (\text{A.16})$$

where $\alpha=0.05$ for 95% confidence and $Q(\cdot)$ is the tail probability of a standard normal random variable. Using (A.15) to invert the above expression gives the following $(1-\alpha)$ confidence interval on the true correlation coefficient $\rho(\lambda_1, \lambda_2)$:

$$\left[\tanh \left[\tanh^{-1} r(\lambda_1, \lambda_2) - Q^{-1}(\alpha/2)/\sqrt{N} \right], \tanh \left[\tanh^{-1} r(\lambda_1, \lambda_2) + Q^{-1}(\alpha/2)/\sqrt{N} \right] \right]$$

A.6 REFERENCES

- [A.1] A.M. Mood, F.A. Graybill and D.C. Boes, *Introduction to the Theory of Statistics*, McGraw-Hill, New York (1974).
- [A.2] W.H. Beyer (ed.), *Handbook of Tables for Probability and Statistics*, CRC Press, Boca Raton, FL (1968).
- [A.3] R.J. Muirhead, *Aspects of Multivariate Statistical Theory*, Wiley, New York (1982).

APPENDIX B

TWO POINT CALIBRATION ERROR ANALYSIS

Appendix B provides background information on two point radiometric calibration of the Bomem FTS, including the effects of error sources on calibration.

B.1 Two Point Radiometric Calibration

For two point radiometric calibration of the Bomem FTS, the complex signal equations are given as:

$$\tilde{S}_T(\lambda) = \tilde{K}(\lambda)L_T(\lambda) + \tilde{S}_P(\lambda) \quad (\text{B-1})$$

$$\tilde{S}_H(\lambda) = \tilde{K}(\lambda)L_H(\lambda) + \tilde{S}_P(\lambda) \quad (\text{B-2})$$

$$\tilde{S}_C(\lambda) = \tilde{K}(\lambda)L_C(\lambda) + \tilde{S}_P(\lambda) \quad (\text{B-3})$$

where

- $L_T(\lambda)$ = the true spectral radiance of the target (unknown),
- $\tilde{S}_T(\lambda)$ = the measured complex target (or background) spectrum (measured),
- $\tilde{S}_H(\lambda)$ = the measured complex spectrum for the hot blackbody (measured),
- $\tilde{S}_C(\lambda)$ = the measured complex spectrum for the cold blackbody (measured),
- $L_H(\lambda)$ = the true spectral radiance of the hot blackbody (known),
- $L_C(\lambda)$ = the true spectral radiance of the cold blackbody (known),
- $\tilde{K}(\lambda)$ = the complex FTS instrument response (unknown),
- $\tilde{S}_P(\lambda)$ = the spectral power of measured stray radiance (unknown).

Equations B-2 and B-3 can then be used to solve for the instrument response:

$$\tilde{K}(\lambda) = \frac{\tilde{S}_H(\lambda) - \tilde{S}_C(\lambda)}{L_H(\lambda) - L_C(\lambda)} \quad (\text{B-4})$$

Inserting this result back into EQ B-2 provides the stray radiance:

$$\tilde{S}_P(\lambda) = \frac{\tilde{S}_C(\lambda)L_H(\lambda) - \tilde{S}_H(\lambda)L_C(\lambda)}{L_H(\lambda) - L_C(\lambda)}. \quad (\text{B-5})$$

Finally, EQ B-1 can now be used to compute the desired spectral radiance of the target:

$$L_T(\lambda) = \frac{\tilde{S}_T(\lambda) - \tilde{S}_P(\lambda)}{\tilde{K}(\lambda)} = \frac{L_H(\lambda) - L_C(\lambda)}{\tilde{S}_H(\lambda) - \tilde{S}_C(\lambda)} \tilde{S}_T(\lambda) - \frac{\tilde{S}_C(\lambda)L_H(\lambda) - \tilde{S}_H(\lambda)L_C(\lambda)}{\tilde{S}_H(\lambda) - \tilde{S}_C(\lambda)}. \quad (\text{B-6})$$

Spectral radiance is a real quantity and thus only the real part of the result of EQ B-6 is used. However, the presence of imaginary residuals in the computed spectral radiance is an indication of calibration error. The magnitude of the calibration error is proportional to the magnitude of the imaginary residual.

B.2 Calibration Error Sources

Radiometric calibration errors are the result of errors in our knowledge of the true calibration source radiances. Estimates of the blackbody spectral radiances ($L'_H(\lambda), L'_C(\lambda)$) for two point calibration (one hot and one cold blackbody calibration source) as a function of the actual spectral radiances ($L_H(\lambda), L_C(\lambda)$) and the spectral radiance errors ($\Delta L_H(\lambda), \Delta L_C(\lambda)$) are:

$$L'_H(\lambda) = L_H(\lambda) + \Delta L_H(\lambda) \quad (\text{B-7})$$

$$L'_C(\lambda) = L_C(\lambda) + \Delta L_C(\lambda). \quad (\text{B-8})$$

After two point calibration of the FTS using our estimates of the blackbody spectral radiances ($L'_H(\lambda), L'_C(\lambda)$), the measured spectral radiance is related to the true spectral radiance via:

$$L'_T(\lambda) = \left(1 + \frac{\Delta L_H(\lambda) - \Delta L_C(\lambda)}{L_H(\lambda) - L_C(\lambda)} \right) L_T(\lambda) + \frac{L_H(\lambda)\Delta L_C(\lambda) - L_C(\lambda)\Delta L_H(\lambda)}{L_H(\lambda) - L_C(\lambda)} \quad (\text{B-9})$$

where L'_T is the measured target spectral radiance and L_T is the actual target spectral radiance. We now have an equation with which we can track the effects of errors in our two point radiometric calibration.

Prior to two point calibration, the blackbody spectral radiance estimates are computed using Planck's equation and our best understanding of the blackbody temperatures (T_H and T_C) and emissivities ($\epsilon_H(\lambda)$ and $\epsilon_C(\lambda)$) as:

$$L'_H(\lambda) = \epsilon_H(\lambda) \times \frac{2hc}{\lambda^5} \times \left(e^{\frac{hc}{\lambda k T_H}} - 1 \right)^{-1} \quad (\text{B-10})$$

and

$$L'_C(\lambda) = \epsilon_C(\lambda) \times \frac{2hc}{\lambda^5} \times \left(e^{\frac{hc}{\lambda k T_C}} - 1 \right)^{-1}. \quad (\text{B-11})$$

Using these equations we can derive the estimated spectral radiances as functions of the true spectral radiance and the error in the knowledge of both temperature (ΔT_H , ΔT_C) and emissivity ($\Delta \epsilon_H(\lambda)$, $\Delta \epsilon_C(\lambda)$):

$$L'_H(\lambda) \cong \left(1 + \frac{\Delta \epsilon_H(\lambda)}{\epsilon_H(\lambda)} \right) \left(1 + \frac{hc}{\lambda k T_H^2} \Delta T_H \right) L_H(\lambda) \quad (\text{B-12})$$

$$L'_C(\lambda) \cong \left(1 + \frac{\Delta \epsilon_C(\lambda)}{\epsilon_C(\lambda)} \right) \left(1 + \frac{hc}{\lambda k T_C^2} \Delta T_C \right) L_C(\lambda). \quad (\text{B-13})$$

It is assumed that the temperature error terms are uncorrelated with the emissivity error terms. The temperature errors have mean temperature uncertainties (dT_H , dT_C) and rms instabilities (σ_{TH} , σ_{TC}) and the emissivity errors have uncertainties ($d\epsilon_H(\lambda)$ and $d\epsilon_C(\lambda)$). Using these assumptions and equations B-7, B-8, B-12, and B-13, we can write our error in blackbody spectral radiance as a function of both temperature and emissivity errors:

$$\Delta L_H(\lambda) = L'_H(\lambda) - L_H(\lambda) \cong \left(\frac{\Delta \epsilon_H(\lambda)}{\epsilon_H(\lambda)} + \frac{hc}{\lambda k T_H^2} \Delta T_H \right) L_H(\lambda) \quad (\text{B-14})$$

$$\Delta L_C(\lambda) = L'_C(\lambda) - L_C(\lambda) \cong \left(\frac{\Delta \epsilon_C(\lambda)}{\epsilon_C(\lambda)} + \frac{hc}{\lambda k T_C^2} \Delta T_C \right) L_C(\lambda). \quad (\text{B-15})$$

These equations, along with the two point calibration EQ B-9, provides a means to analyze the effects of temperature and emissivity errors on the two point calibration procedure. We can rewrite the calibration equation as:

$$L'_T(\lambda) = a(\lambda)L_T(\lambda) + b(\lambda) \quad (\text{B-16})$$

where

$$a(\lambda) = \left(1 + \frac{\Delta L_H(\lambda) - \Delta L_C(\lambda)}{L_H(\lambda) - L_C(\lambda)} \right) \quad (\text{B-17})$$

$$\text{and } b(\lambda) = \frac{L_H(\lambda) \Delta L_C(\lambda) - L_C(\lambda) \Delta L_H(\lambda)}{L_H(\lambda) - L_C(\lambda)}. \quad (\text{B-18})$$

B.2.1 Absolute Temperature Inaccuracy (Temporally fixed error)

As previously stated, inaccuracies in our knowledge of the source temperatures leads to calibration errors. Let $dT = dT_H = dT_C =$ the uncertainty of each source. If each source is independent, then the results of EQ B-17, EQ B-18, and the approximation:

$$\frac{dL(\lambda)}{dT} \approx \frac{hc}{\lambda k T^2} L(\lambda), \quad (\text{B-19})$$

can be used to determine the uncertainty in the gain ($da(\lambda)$) and offset ($db(\lambda)$), given by:

$$da(\lambda) = \frac{1}{\sqrt{2}} \times \frac{1}{L_H(\lambda) - L_C(\lambda)} \times \left(\frac{hc}{\lambda k T_H^2} L_H(\lambda) + \frac{hc}{\lambda k T_C^2} L_C(\lambda) \right) dT \quad (\text{B-20})$$

$$db(\lambda) = \frac{1}{\sqrt{2}} \times \frac{L_H(\lambda) L_C(\lambda)}{L_H(\lambda) - L_C(\lambda)} \times \left(\frac{hc}{\lambda k T_H^2} + \frac{hc}{\lambda k T_C^2} \right) dT. \quad (\text{B-21})$$

B.2.2 Emissivity Uncertainty (Temporally fixed error)

Inaccuracies in our knowledge of the source emissivities also leads to calibration errors. Let $d\varepsilon(\lambda) = d\varepsilon_H(\lambda) = d\varepsilon_C(\lambda) =$ the uncertainty of each source. If the gain and bias are independent, then this results in an uncertainty in the gain and offset, given by:

$$da(\lambda) = \frac{1}{\sqrt{2}} \times \frac{L_H(\lambda) + L_C(\lambda)}{L_H(\lambda) - L_C(\lambda)} \times \frac{d\varepsilon(\lambda)}{\varepsilon(\lambda)} \quad (\text{B-22})$$

$$db(\lambda) = \frac{L_H(\lambda) L_C(\lambda)}{L_H(\lambda) - L_C(\lambda)} \times \frac{d\varepsilon(\lambda)}{\varepsilon(\lambda)}. \quad (\text{B-23})$$

B.2.3 Temperature Instability (Temporally varying error)

Temporal changes in the calibration source temperatures will also lead to calibration errors. Let $\sigma_T = \sigma_{TH} = \sigma_{TC}$ = the rms instability of each source. If the gain and bias are independent, then this results in an rms instability in the gain and offset of:

$$\sigma_a(\lambda) = \frac{1}{\sqrt{2}} \times \frac{1}{L_H(\lambda) - L_C(\lambda)} \times \left(\frac{hc}{\lambda k T_H^2} L_H(\lambda) + \frac{hc}{\lambda k T_C^2} L_C(\lambda) \right) \sigma_T \quad (\text{B-24})$$

$$\sigma_b(\lambda) = \frac{1}{\sqrt{2}} \times \frac{L_H(\lambda) L_C(\lambda)}{L_H(\lambda) - L_C(\lambda)} \times \left(\frac{hc}{\lambda k T_H^2} + \frac{hc}{\lambda k T_C^2} \right) \sigma_T. \quad (\text{B-25})$$

B.2.4 Random Reflected Radiance Components

Random reflections off the calibration sources must also be considered because of nonperfect blackbody emissivities (i.e., $\epsilon < 1.0$). Let us assume that the illumination of each source, which is to be subsequently reflected, has variance σ_S^2 . The expected value for $1-\epsilon$ is $d\epsilon$. If the illumination for each source is independent, then:

$$\sigma_a(\lambda) = \frac{d\epsilon(\lambda)}{\sqrt{2}} \times \frac{\sigma_S(\lambda)}{L_H(\lambda) - L_C(\lambda)} \quad (\text{B-26})$$

$$\sigma_b(\lambda) = \frac{d\epsilon(\lambda)}{\sqrt{2}} \times \frac{L_H(\lambda) + L_C(\lambda)}{L_H(\lambda) - L_C(\lambda)} \sigma_S(\lambda). \quad (\text{B-27})$$

B.3 Calibration Error Case Analyses

B.3.1 Case 1: Measurements Within a Single Calibration Cycle

If both mean and coherence measurements are made within a single calibration cycle, then only fixed errors result in the gain (a) and bias (b) terms. The estimated means, mean differences, variances, and correlations are then given as:

$$\hat{\mu}_L(\lambda) = [1 + \Delta a(\lambda)] \mu_L(\lambda) + \Delta b(\lambda) \quad (\text{B-28})$$

$$\hat{\mu}_{\Delta L}(\lambda) = [1 + \Delta a(\lambda)] \mu_{\Delta L}(\lambda) \quad (\text{B-29})$$

$$\hat{\sigma}_L^2(\lambda) = \sigma_L^2(\lambda) \quad (\text{B-30})$$

$$\hat{\rho}_L(\lambda_1, \lambda_2) = \rho_L(\lambda_1, \lambda_2). \quad (\text{B-31})$$

The effect on the mean difference measurement is to cause an uncertainty given by:

$$d\mu_{\Delta L}(\lambda) = da(\lambda)\mu_{\Delta L}(\lambda). \quad (\text{B-32})$$

There is no effect on the correlation measurement.

B.3.2 Case 2: Measurements Made Within Different Calibration Cycles

If both mean and correlation measurements are made within different calibration cycles, then it is necessary to include the effects of calibration source instability. Assume that each measurement is made with a different (uncorrelated) calibration error resulting from temperature instability σ_T . The gain and bias terms now have a fixed random error. The estimated means, mean differences, variances, and correlations are then given as:

$$\hat{\mu}_L(\lambda) = [1 + \overline{\Delta a}(\lambda)]\mu_L(\lambda) + \overline{\Delta b}(\lambda) \quad (\text{B-33})$$

$$\hat{\mu}_{\Delta L}(\lambda) = \left[1 + \frac{\Delta a_{irg}(\lambda) + \Delta a_{bkg}(\lambda)}{2}\right]\mu_{\Delta L}(\lambda) + (\Delta b_{irg}(\lambda) - \Delta b_{bkg}(\lambda)) \quad (\text{B-34})$$

$$\begin{aligned} &+ (\Delta a_{irg}(\lambda) + \Delta a_{bkg}(\lambda)) \left(\frac{\mu_{L_{irg}}(\lambda) + \mu_{L_{bkg}}(\lambda)}{2} \right) \\ &= \sigma_L^2(\lambda) + \sigma_b^2(\lambda) + \sigma_a^2(\lambda)\mu_L^2(\lambda) + 2\sigma_a(\lambda)\sigma_b(\lambda)\mu_L(\lambda)\rho_{ab}(\lambda), \end{aligned} \quad (\text{B-35})$$

$$\hat{\rho}_L(\lambda_1, \lambda_2) = \frac{E\left[\{a(\lambda_1)L(\lambda_1) + b(\lambda_1)\}\{a(\lambda_2)L(\lambda_2) + b(\lambda_2)\}\right]}{\hat{\sigma}_L(\lambda_1)\hat{\sigma}_L(\lambda_2)} \quad (\text{B-36})$$

$$\begin{aligned} &= \frac{\{\sigma_L(\lambda_1)\sigma_L(\lambda_2) + \sigma_a(\lambda_1)\sigma_a(\lambda_2)\rho_{aa}(\lambda_1, \lambda_2)\sigma_L(\lambda_1)\sigma_L(\lambda_2)\}}{\hat{\sigma}_L(\lambda_1)\hat{\sigma}_L(\lambda_2)} \times \rho_L(\lambda_1, \lambda_2) \\ &+ \frac{1}{\hat{\sigma}_L(\lambda_1)\hat{\sigma}_L(\lambda_2)} \{ \sigma_a(\lambda_1)\sigma_a(\lambda_2)\rho_{aa}(\lambda_1, \lambda_2)\mu_L(\lambda_1)\mu_L(\lambda_2) \\ &+ \sigma_a(\lambda_1)\sigma_b(\lambda_2)\rho_{ab}(\lambda_1, \lambda_2)\mu_L(\lambda_1) + \sigma_a(\lambda_2)\sigma_b(\lambda_1)\rho_{ab}(\lambda_2, \lambda_1)\mu_L(\lambda_2) \\ &+ \sigma_b(\lambda_1)\sigma_b(\lambda_2)\rho_{bb}(\lambda_1, \lambda_2) \}, \end{aligned}$$

The effect on the mean difference measurements is to provide the uncertainty given by:

$$d\mu_{\Delta L}(\lambda) = \frac{da}{\sqrt{2}}\mu_{\Delta L}(\lambda) + \sqrt{2}\sigma_b + \sqrt{2}\sigma_a \left(\frac{\mu_{L_{trg}}(\lambda) + \mu_{L_{bkg}}(\lambda)}{2} \right) \quad (B-37)$$

The effect on the correlation is to provide a decorrelation gain and correlation bias. The decorrelation gain reduces the correlation while the bias can actually increase correlation.

B.4 Calibration Error Examples

Sample numerical calculations have been included to provide a sense of the magnitude of the calibration errors. The following conditions have been assumed or calculated:

- 1) Hot Calibration Source: $T_H = 40$ C, $L_H = 11.5 \times 10^{-5}$ W/cm²/μm/sr at 4μm
- 2) Cold Calibration Source: $T_C = 10$ C, $L_C = 3.4 \times 10^{-5}$ W/cm²/μm/sr at 4μm
- 3) Assumed Calibration Source Attributes (both sources at 4μm):

$$\varepsilon = 1.0, d\varepsilon = 0.01, \sigma_S = \sigma_L, \sigma_T = 0.05C, dT = 0.1C$$

- 4) Target Attributes: $T_{trg} = 25C$, $\mu_L = 6.5 \times 10^{-5}$ W/cm²/μm/sr at 4μm
- 5) Calculated Quantities:

$$\text{Absolute Temperature Inaccuracy: } da = 0.0053, db = 0.028 \times 10^{-5} \text{ W/cm}^2/\mu\text{m/sr}$$

$$\text{Absolute Emissivity Uncertainty: } da = 0.013, db = 0.045 \times 10^{-5} \text{ W/cm}^2/\mu\text{m/sr}$$

$$\text{Temperature Instability: } \sigma_a = 0.0027, \sigma_b = 0.014 \times 10^{-5} \text{ W/cm}^2/\mu\text{m/sr}$$

$$\text{Emissivity Instability: } \sigma_a = 0.011 (\sigma_L/\mu_L)$$

$$\sigma_b = 0.085 \times 10^{-5} \text{ W/cm}^2/\mu\text{m/sr} (\sigma_L/\mu_L).$$

B.4.1 Case 1: Measurements Within a Single Calibration Cycle

For mean difference and correlation measurements made within a single calibration cycle:

$$1) \text{ Relative mean difference error} = \frac{d\mu_{\Delta L}}{\mu_{\Delta L}} = 1.3\% \text{ and is limited by } d\varepsilon,$$

and 2) The decorrelation factor is 1.0 and the correlation bias is 0.0.

The conclusion is that calibration errors under a single calibration cycle are negligible.

B.4.2 Case 2: Measurements Made Within Different Calibration Cycles

For mean difference and correlation measurements made between multiple calibration cycles the error values are given in Table B-1.

Table B-1: Case 2 Calibration Errors

	$\sigma_T = 0.5K$ $\sigma_L/\mu_L = 0.02$	$\sigma_T = 1.0K$ $\sigma_L/\mu_L = 0.08$	$\sigma_T = 5.0K$ $\sigma_L/\mu_L = 0.2$
$d\mu_{\Delta L} / \mu_L$	0.0051	0.0053	0.0073
Decorrelation factor	0.97	0.998	0.9994
Correlation Bias	0.04	0.003	0.0009

B.5 Conclusions

- 1) The correlation and mean difference measurements made within a single calibration cycle will be practically unaffected by anticipated miscalibrations.
- 2) The correlation and mean difference measurements between multiple calibration cycles are more affected, but errors can be minimized using stable sources.
- 3) Expected mean difference uncertainties will be on the order of 1% apparent emissivity or less between calibration cycles.
- 4) Expected decorrelation due to calibration source instability will range from 0.97 to 0.999 depending on scene radiance variance (between calibration cycles).